Turbulent Simulations of a Buoyant Jet-in-Crossflow

Christian T. Martin

Thesis submitted to the Faculty of the
Virginia Polytechnic Institute and State University
in partial fulfillment of the requirements for the degree of

Master of Science
in
Aerospace Engineering

Eric G. Paterson, Chair
Jonathan S. Pitt
Todd K. Lowe

Nov. 18th, 2019
Blacksburg, Virginia

Keywords: HRLES, JICF, buoyant, crossflow, DES, CFD, OpenFOAM, near-field

Turbulent Simulations of a Buoyant Jet-in-Crossflow

Christian T. Martin

(ABSTRACT)

A lack of complex analysis for a thermally buoyant jet in a stratified crossflow has motivated the studies presented. A computational approach using the incompressible Navier–Stokes equations (NSE) under the Boussinesq approximation is utilized. Temperature and salinity scalar transport equations are utilized in conjunction with a linear equation of state (EOS) to obtain the density field and thus the buoyancy forcing. Comparing simulation data to experimental data of a point heat source in a stratified environment provides general agreement between the aforementioned computational model and the physics studied. From the literature surveyed, no unified agreement was presented on the selection of turbulence models for the jet–in–crossflow (JICF) problem. For this reason, a comparison is presented for a standard Reynolds–Averaged Navier–Stokes (RANS) and a hybrid Reynolds–Averaged Navier–Stokes/large eddy simulation (HRLES) turbulence model. The mathematical differences are outlined as well as the implications each model has on solving a buoyant jet in stratified crossflow. The RANS model provides a general over prediction of all flow quantities when comparing to the HRLES models. Studies involving the removal of the thermal component inside the jet as well as varying the environmental stratification strength have largely determined that these affects do not alter the near-field in any significant way, at least for a high Reynolds number JICF. The velocity ratio of the jet being the ratio of the jet velocity to the free–stream flow velocity. Deviating from a velocity ratio of one has provided information on the variability of the forcing on the plate the jet exits from, as well as in the integrated energy quantities far downstream of the jet's exit. The departures presented here show that any deviation from the unity value provides an increase in the overall forces seen by the plate. It was also found that the change in the integrated potential and turbulent kinetic energies is proportional to the deviation from a unity velocity ratio.

Turbulent Simulations of a Buoyant Jet-in-Crossflow

Christian T. Martin

(GENERAL AUDIENCE ABSTRACT)

A lack of complex analysis for a heated jet in a non-uniform crossflow has motivated the studies presented. A computational approach for the fluid dynamics governing equations under specific assumptions is implemented. Additional equations are solved for temperature and salinity in conjunction with a linear equation of state to obtain the density field. Comparing simulations to experimental data of a point heat source in a non-uniform, fluid tank provides general agreement between the aforementioned computational model and the physics studied. Studying the literature yields no unified agreement on the selection of turbulence treatment for the jet-in-crossflow problem. For this reason, a comparison is presented for two various techniques with differing complexity. The mathematical differences as well as the implications each model are outlined, specifically pertaining to a heated jet in a non-uniform crossflow. The simpler model provides a general over prediction when compared to the more complex model. Studies involving the removal of the heat from inside the jet as well as varying the environmental forcing have largely determined that these affects do not alter the flow field near the jet's origin point in any significant way. Changing the jet's velocity has provided information on the variability of the forcing on the plate the jet exits from, as well as in the energy released into the environment far downstream of the jet's exit. The ratios presented show that any deviation from a notional value provides an increase in the overall forces seen by the plate. It was also found that the change in the released energies is proportional to the deviation from the notional jet velocity.

Dedication

To Caitlin, my children: CJ, Thea, and Zayden, my parents, and Nikki.

Acknowledgments

I would like to give my deepest appreciation to my advisor, Dr. Eric Paterson for his guidance along my academic journey and for all the knowledge he shared with me. I would also like to thank my committee members, Dr. Jonathan Pitt and Dr. Todd Lowe, for their knowledge and feedback on my research and thesis.

Thank you to my colleagues who helped me gain the necessary knowledge and skills to further my research to its current state. I would also like to thank my professor, Dr. Christopher Roy for the knowledge that his courses provided that helped me further my understanding of the process and procedures of computational fluid dynamics.

My final appretiation goes to my wife, Caitlin, for her relentless support as I continued through my time at Virginia Tech, and to my children who were the driving force that kept me on my path.

Contents

List of Figures

List of Tables

Chapter 1

Introduction

1.1 Motivation

A jet interacting with a crossflow is considered a jet–in–crossflow (JICF). The notional jet has been accepted to be embedded in a flat plate with a boundary layer growing from upstream of the jet's exit point. The jet then interacts with this boundary layer, as well as the incoming crossflow. JICFs are common throughout various engineering problems and disciplines, as well as all throughout nature. Some examples of these applications are VTOL and STOVL aircraft, film cooling for turbine blades, fuel injection systems, exhaust stacks, and hydrothermal vents on the oceans' floors. This sample is by no means an exhaustive list of the various occurrences of the JICF, however, its purpose is to demonstrate the vast array of applications and scenarios where a fundamental understanding of the JICF and its behavior are necessary for accurate predictions to be made. Many have studied the JICF problem to better understand these fundamental questions. However, much of these investigations have been carried out for low Reynolds number and high velocity ratio ($r = U_j/U_0$) flows. Examples inside this space include fuel injection systems, exhaust stacks, hydrothermal vents, and other applications For this regime, there is a general agreement on the fundamental physics and flow characteristics observed. However, the same cannot be said for the case of higher Reynolds number, low velocity ratio jets. These types of jets in crossflow are better suited for applications such as film cooling on turbine blades, where the mixing of the jet is desired to be kept near to the surface the jet exited from. It is also noted that a fair number of these studies neglect much, if not all, of the buoyancy forcing, particularly the forcing that stems from the stratification of the crossflow. The interest here is due to the lack of investigation of these high Reynolds number jets with low velocity ratios, especially for buoyant jets.

1.2 Objectives

The present study stems from the lack of understanding of the fate and transport of a high Reynolds number, low velocity ratio, buoyant jet in a stratified crossflow. Specifically, how various turbulence modeling techniques impact the capturing of the interaction between the jet and the crossflow, as well as which modeling technique, are recommended for such an

application. To further the understanding of such a problem, a series of computational fluid dynamics (CFD) simulations are devised to help fill this gap in the fundamental understanding. The overarching objectives are presented, below:

1. Determine the turbulence modeling technique required to capture the JICF far downstream of the orifice (approximately 100 diameters).
2. Quantify the differences in the downstream wake when utilizing different turbulence modeling techniques.
3. Perform a parametric study for the JICF problem studying the following aspects on the fate and transport of the jet downstream of its origin.
   (a) Internal Buoyancy (i.e., non–heated vs heated jets)
   (b) Environmental Buoyancy (i.e., stratification strength)
   (c) Internal Momentum (i.e., jet velocity)

1.3 Agenda

The presented work will be organized in such a way to first discuss the current literature regarding the JICF problem, where the JICF will be studied, then the usage of various turbulence models for the JICF problem will be investigated, and finally a look into the JICF as it pertains to stratified fluids will be conducted. After surveying the literature on the JICF problem, the overall computational approach for a CFD flow solver is discussed. This discussion will include detailed information on the following: the mathematical model, numerical methods, boundary and initial conditions, as well as point source declarations. Following the basic outline of the CFD flow solver, a verification and validation (V&V) study will be presented. This section will outline the author's definition of these terms, as well as the processes used to perform the V&V study for the aforementioned CFD flow solver. Finally, a discussion of the JICF problem, which will present the overall setup along with a grid-study, reasoning for the usage of the hybrid turbulence modeling technique, mentioned later and a parameter study to demonstrate the affects of buoyancy and momentum on the fate and transport of the JICF downstream of the jet origin, will be presented.

Chapter 2

Literature Review

The literature review of a JICF is broken into three individual sections. The first being a general review of the literature focusing on the fundamental physics and understanding of the jet in crossflow problem, which are presented in the literature. Following this section is a section devoted to turbulence model selection. A study of the historical methods for treating the turbulence modeling in simulations of the jet in crossflow problem will be outlined and the current state–of–the–art will be discussed. Finally, the topic of stratified flows will be reviewed. Much of this review will be focused on how stratification in the crossflow affects the interaction between the jet and the crossflow.

2.1 Jet–in–Crossflow

A jet impinging on a perpendicular crossflow is a common engineering problem. For this reason, it has had extensive exposure from various industries and research fields. Some of the earliest instances of investigating this complex phenomenon started in the 1950's with experiments geared toward ensuring exhaust gases from ship funnels would not blow down onto the ship's deck, causing complications for the ship's personnel [1]. Similarly, research on land-based exhaust funnels used numerical investigations to quantify the downwash of industrial plant exhaust into cities [43]. Other experimental studies were conducted in order to understand the fundamental trajectory of the jet's wake as it interacted with the crossflow [17, 27]. Alongside these experiments, analytical approaches were also pursued as a method to obtain a simplistic expression for the jet's trajectory [27, 33]. As these early investigations were heavily application driven, much of the insight gained pertains to a small subset of the wide domain the JICF envelops. For this reason, these studies did not progress much in the way of fundamentally understanding the interaction between the jet and the crossflow. This was made clear by Morton [33], stating that his solution to the JICF problem "add[s] nothing to the physical understanding of the flows described."

In addition to the desire to better understand the trajectory of exhaust from smoke stacks, an interest in the understanding of how waste-water dumped into bodies of water also arose. Experimental and analytical investigations of buoyant and non-buoyant jets impinging into uniform and stratified crossflows were conducted by Fan [15]. These studies presented a more fundamental understanding of the overall impact on the jet-crossflow wake that the

various buoyancy sources have investigated. Experiments motivated by desalination plant outfalls were conducted by Chu [10] who employed a theoretical approach. Again, the main goal was to formulate an expression for the jet–crossflow wake's trajectory. Through the 1970's, research continued with investigations on air quality near exhaust from plants and operational equipment [5, 20]. Experiments were also conducted focusing on the cooling of combustion gases inside gas turbines [26].

By the mid 1980's, Sykes et al. attempted to dive deeper into the fundamentals and characteristics of the jet–crossflow wake, beginning their paper with "the details of the transition are complicated and not well understood, and we hope to shed some further light on the process"' [47]. The transition spoken of refers to the bending of the jet, initially perpendicular to the crossflow, until parallel with the crossflow. Their approach to the problem was one of the earlier numerical approaches where more information than the overall trajectory of the centerline or the maximum vertical height was computed. For these computations, the Navier–Stokes equations are solved in addition to a turbulent energy and a passive scalar. Their model constants were selected empirically. The setup of the computational domain used lead to the jet being placed inside on of the boundaries. This would ultimately mimic the wall bounded JICF. However, Sykes et al. noted that "we do not treat the lower surface as a true wall outside the jet-exhaust region," noting this is due to a more extraneous mesh requirement near the wall and their problem of interest being smoke stacks, which are freestanding and thus have no wall affects [47].

Morton and Ibbetson [34] rebutted that this statement, and a few others, such as Sykes et al. [47] had a fundamental misunderstanding of the implementations of their computational choices and, thus, a flawed understanding of their results. This led to his rebuttal paper where a detailed approach to understanding the fundamentals of this flow are outlined. From their break–down of the flow and their experiments, the significance of the vorticity inside the JICF is emphasized. They also confirmed the "universal existence of the embedded vortex pair in deflected jets" [34] and tied the entrainment strength back to these vortex pairs.

During the same time that Morton and Ibbetson published their paper, many others began numerically investigating the JICF problem using various CFD techniques. Among some of these CFD studies include Chen and Yapa [9], Cavar and Meyer [7], and Muppidi and Mahesh [37]. A more detailed review of the historical approach to computational modeling is presented in section 2.2. Despite CFD's increase in popularity, experimental investigations have remained an invaluable source of knowledge about the JICF as a whole. Much of these experiments can be used for CFD model validation purposes before extending the application of the model. Kulkarni, Singh and Seshadri [29, 30] and Mokhtarzadeh-Dehghan, König, and Robins [36], are both examples of groups conducting experimental studies specifically to validate their CFD models. Other experimental work includes studies on interactions between multiple jets [11], geometrical variations of the jet orifice [38, 39, 40], as well as experiments geared towards understanding the effects of momentum, entrainment, and Reynolds number scaling on the interaction between the jet and the crossflow in order to better design future

experiments [45].

Much of the applications that are driving the continuation of studies into the JICF problem have spread out from the conventional smoke stack and ship funnel exhaust plumes. This spread includes areas such as film cooling of turbine blades [4, 16], turbulent mixing [3, 8, 14, 32, 41], as well as on plumes discharged from trailing suction hopper dredger vessels [13]. Alongside the increase in the scope of the applications driving the JICF studies, the complexity of the measurements and quantifications have increased. In the earlier studies of Acker [1], Priestley [43] and Gördier [17], the main concentration was the dispersion of the plume and its contents, as well as its trajectory. More recent studies by Garg and Gaugler [16] and Yin and Durbin [4], for example, investigate the cooling capacity of these flows.

2.2 Turbulence Modeling

Much of the numerical and analytical research pertaining to the understanding of the JICF problem began with rudimentary test problems. This was due to the lack of computational ability to numerically solve the complexity rooted in the JICF problems of interest. Referring to his basic momentum-mass flux analysis presented in 1961 [33], Morton acknowledged this with his statement, "the unfortunate fact is that more sophisticated methods of attack are often not available." As technology progressed, the computational capacity of machines drastically increased. This increase in computational ability allowed many fields to better utilize computational mechanics in various ways for a wider variety of investigations.

In 1995, Chang and Chen [8] utilized CFD to help understand the effects of design considerations for gas–turbine combustors. Their simulations involved two opposing jets in channel flow in which they used a Reynolds–Averaged Navier–Stokes, (RANS) turbulence model. Upon varying the momentum fluxes and inclination angles of these jets, they were able to uncover a correlation between the temperature and velocity distributions, the wake dimensions, and the reattachment point all in terms of the momentum flux, location, and inclination.

Both Lavelle [31] and Chen and Yapa [9] used computational modeling to help predict plumes in an oceanic environment. Lavelle used what he referred to as VLES, or Very Large Eddy Simulation. The differentiation between VLES and Large Eddy Simulations (LES) was mentioned to be a computational grid not fine enough to effectively model the smallest scales, but these "scales fall within the subinertial range of turbulence where details of dissipation ought not to matter" [31]. Chen and Yapa used the COMBOS3D software to modeling oil spills, incorporating phase change into the modeling [9]. These studies involved low velocity ratios with the inclusion of jet buoyancy and thus created free–convection plumes dominated by buoyancy forcing.

Continuing the study of the JICF, many studies through the 2000's were carried out using the implementation of RANS turbulence modeling for solving this problem. Kulkarni, Singh,

and Seshadri [29] performed validation of a RANS model and its ability to accurately predict experimental results of ship funnel exhaust smoke behind a bluff body. They then continued their research by comparing experimental and RANS computations for various configurations of ship funnels with varying velocity ratios [30]. In 2006, Mokhtarzadeh-Dehghan, König, and Robins [36] used RANS turbulence modeling to compare to experimental data of smoke stack exhaust. After validating their simulations, they performed a comparison of select RANS variants as well as a Differential Flux Model (DFM) which showed stronger evidence than either of the RANS models demonstrated. However, their conclusion came to be that the DFM model was more computationally expensive than a sufficiently fine computational solution using either of the RANS models.

To assess the capabilities of RANS modeling for the JICF problem, Muppidi and Mahesh [37] computed Direct Numerical Simulations (DNS) for a jet impinging on a crossflow. Before making claims about the usage of their DNS results, their simulations were compared to experimental results to ensure validity. They then provided evidence, using their DNS results, to conclude that the JICF characteristics were not in "turbulent equilibrium" [37]. The underlying claim here is that, at least near the jet orifice, a RANS model does not have the capacity to accurately model and predict the problem of the JICF.

The continued usage of RANS modeling, despite its short comings when compared to more complex techniques, was predominately due to the lack of computational resources to utilize the more complex methods of DNS and LES. As technology advances, so does the complexity of computational studies. For this reason, simulations began to shift towards utilizing more complex methods, such as LES. For larger and more complex problems, DNS is still a difficult challenge and is selectively used. With the increase in complexity of simulations, studies of turbulent mixing are more accessible. Paik [41] studied turbulent mixing of thermal discharge from a smoke stack using LES demonstrating the experimental matching capabilities of LES techniques for such complex interactions. Roger et al. [14] used LES turbulence modeling to investigate the mixing capabilities of interacting square jets in order to further the understanding of industrial mixers.

With the desire to increase the complexity of the JICF problems handled with CFD, approaches to blend the, less computationally intensive but also lower fidelity, RANS models with the, more computationally intensive, yet higher fidelity–yielding LES models. This blend is known as the Hybrid Reynolds–Averaged/Large Eddy Simulation (HRLES) model and would have a more feasible computational requirement, while also having a higher fidelity than the previous RANS models. Yin and Durbin [4] implemented a HRLES model to study the film cooling on turbine blades. Studying the turbulent mixing of fuel inside combustors, Prause et al. [3] also utilized a HRLES turbulence model.

Depending on the requirements and complexities of the problem studied, various turbulence modeling techniques and strategies are selected to gain the most favorable outcomes. With the increase in computational capacities available, came an increase in the utilization of more complex modeling techniques. Despite studies showing LES modeling techniques superior-

ity over RANS models, application-based engineering cannot always utilize the increased computational resources that accompany the LES modeling techniques. For this reason, a greater interest has risen for investigating the overall capabilities of HRLES models for the JICF problem as well as to gain better understanding of where they fall on the spectrum between RANS and LES modeling techniques.

2.3 Stratified Flows

Stratified environments have been investigated for decades. Much of this is due to the direct comparison to environments seen in realistic conditions. Some of the early works involved investigating wakes passing through stratified fluids. Early experiments by Kennedy and Frobel [28] in 1964 involved laboratory investigations of two-dimensional bodies traversing at the interface of a two-layer density stratification. In 1965, Wu [50] studied the wake of a submerged body in an attempt to characterize three independent regimes of the wake collapse. Other experimental investigations lead van de Watering [49] to conclude that, far downstream, the vertical growth of a turbulent wake decreases until it collapses onto the wake.

Some of experiments conducted involved utilization of a net–zero–momentum wake to emulate a self–propelled body [46]. Alongside the experimental investigations, numerical and analytical investigations were also being conducted. In 1967, Morton [35] devised entrainment models for jets, plumes, and wakes. Both Pao and Janowitz in 1968 [25, 52] utilized the Boussinesq approximation in their attempts to numerically solve the Navier–Stokes Equations. Pao also used his theoretical approach to compare with their experimental studies.

Similar interest has been shown for jets in stratified fluids. Some early work by Darden [12] examined differences between non–buoyant and buoyant line jets in a linear density stratified environment. It was determined that buoyant jets entrained about five times the amount of the environmental fluid, when compared to the non-buoyant jet. Utilizing a point source of momentum, Afanas'ev and Voropaev [2], studied a jet entering a density stratified fluid. Xu and Chen, in 2012 [51], used particle image velocimetry (PIV) and planar laser–induced fluorescence (PLIF) measurements to determine velocity and density fields of a jet entering density stratified fluid. Again using the Boussinesq approximation, Peyret in 1976 [42], investigated jets in stratified fluids while varying the Reynolds and Froude numbers found in their investigations.

Due to an increase in the popularity of the nuclear energy, some investigators have begun studying catastrophic events such as a Loss of Coolant Accident (LOCA). Numerically studying these types of events can bring about much safer solutions than an accurate experimental approach would present. Sarikurt and Hassan in 2017 [44] validated their LES model by simulating an LOCA event and comparing their results to the OECD–NEA conducted experiments of a similar event. These aforementioned studies have only pertained to jets

and wakes in quiescent, stratified environments. Much of the early investigations, pertaining to stratified flows were conducted for wakes.

Early investigations mentioned earlier [1, 17, 27, 33, 43], the buoyancy forcing, either through the jet's density difference or environmental stratification, was ignored due to the increased complexity of the experiment and/or model. This was addressed by Priesley [43] discussing the drastic temperature drop near the jet's exit as "clear that thermal stratification will exert an important modifying influence." Despite this acknowledgement, no analysis was conducted using thermal stratification in his studies. Theoretical and experimental investigations by Fan in 1967 [15] were conducted for buoyant jets in a quiescent stratified fluid as well as non–buoyant jets in a uniform crossflow. For these investigations, it was noted that theoretically, an overall estimation of the trajectory and shape of the buoyant plume could be determined and was accurately predicted by theory. From these experiments, Fan was able to fine tune the entrainment coefficient of this theoretical analysis to achieve better agreement with the experimental data. Fan was also able to predict the buoyant jets half-width inside a uniform crossflow with theoretical analysis. Despite these advancements in the theoretical analysis, these cases do not include buoyancy in the jet and the environment, nor a crossflowing fluid acting at the same time. This is theorized to be mostly due to the complexity of setting up a stably stratified crossflow. In Fan's dissertation, the buoyant jet in a stratified crossflow is briefly mentioned, outside of the depiction of the theorized flow.

In 1985, Hwang and Chiang [21] utilized a numerical analysis, carried out for a vertical buoyant jet, in a uniform stratified crossflow. From these studies, the maximum rise–of–height of multiple cases were compared to experimental data, also conducted by Hwang and Chiang. Following this investigation, Hwang, Pon, and Yang [22] devised an entrainment model to predict the centerline trajectory of the wake created from the interaction of the jet and the crossflow. Their model compared well with experimental data for non-buoyant and buoyant cases for various Froude numbers. Simple analytical models, like the entrainment model determined by Hwang, Pon, and Yang have successfully been validated against experimental studies, however, the nature of these models only allows for limited information to be gained from their usage. A continued search for more detailed methods of understanding and obtaining information about the jet-in-crossflow is underway and fuels the following research.

2.4 Summary of Contributions

As shown from the literature surveyed, there is a lack of understanding of both the fate and transport of the wake of a JICF far downstream (e.g., 100 jet diameters) of the jet's exit. Much of the investigations have been for high velocity ratio jets impinging into non–stratified, low Reynolds number cross–flow, which do not mimic practical applications and thus are of little use when investigating their results for application–based problems. Only a handful of studies have conducted research that effectively shows the differences between

utilizing a RANS model to simulate the JICF problem when compared to LES and even fewer for HRLES models. Due to the apparent lack of literature on these subjects, the current research was conducted. First, an investigation into the ability of a RANS model to accurately capture the wake of the JICF far downstream from the jet's exit is conducted with comparisons to a HRLES model. Following this analysis is a quantitative comparison of the differences between each model's velocity and temperature profiles far downstream of the jet's orifice. Finally, utilizing the HRLES model only, the investigation of the influence of jet heating, environmental stratification, and jet velocity on the fate and transport are demonstrated.

Chapter 3

Computational Methods

3.1 The CFD Process

To further the understanding the CFD approach, the overall process should be outlined. For any CFD problem, there exists three main portions of the analysis. First is the conceptional or "thinking" phase, followed by the simulation phase, and concludes with the post-processing or analysis phase. Before any simulation is to take place, a conceptional understanding of the following is required: the problem as a whole, the flow, environmental, boundary, and initial conditions. After grasping the overall problem and its setup, the outcomes of the simulations should be determined. When all these are taken into consideration, the mesh can be designed to ensure resolution of the flow and capture the desired outcomes. After the mesh is generated, the simulation phase can begin. Here, the previously determined information for the simulation is converted to the CFD solver's inputs. After the simulation is setup, it can be run, either in serial or parallel, depending on the solver and/or the problem of interest. Once the simulation has been completed, the desired outcomes are extracted from the simulation and analyzed. The simulation can also be visualized to better convey the simulation and its solution. Numerical errors are estimated and comparison errors and uncertainties should be computed. These help to ensure the validity of the simulation performed.

3.2 Mathematical Model

This section will outline the equations used in the simulations to follow. Starting with the instantaneous Navier–Stokes equations and scalar transport equations the derivation of the RANS and LES equations will be presented. Next, the HRLES equations with an explanation of the function that switches the modeling from LES to RANS in specified regions are demonstrated. For each of these models, the associated turbulence model used is detailed. Finally the linear equation of state is detailed.

3.2.1 Navier-Stokes Equations

To solve the fluid–flow problem of the JICF, the Navier–Stokes Equations (NSE) are implemented. The incompressible, instantaneous NSE in the Boussinesq form are shown in eqns. (3.1-3.2) using tensor notation.

$$\frac{\partial u_j}{\partial x_j} = 0 \tag{3.1}$$

$$\frac{\partial u_i}{\partial t} + \frac{\partial (u_i u_j)}{\partial x_j} = -\frac{1}{\rho_0}\frac{\partial p}{\partial x_i} + \frac{\partial}{\partial x_j}\left(2\nu S_{ij}\right) + \frac{\Delta\rho}{\rho_0} g_i \tag{3.2}$$

$$with$$

$$S_{ij} = \frac{1}{2}\left(\frac{\partial u_i}{\partial x_j} + \frac{\partial u_j}{\partial x_i}\right)$$

This form of the NSE has U as the non–inertial velocity, t as time, x as the spatial coordinates, ν as the molecular viscosity, and S_{ij} is the rate of strain. Additionally, the gravitational acceleration g points in the negative z direction. The density difference $\Delta\rho$ is the deviation from the background density, ρ_{BG}. These density values are related through the expression for total density, $\rho = \Delta\rho + \rho_{BG}$. The pressure $\hat{p}$ is the piezometric pressure, which can be determined by $\hat{p} = p - \rho|g|z$, where $|g|$ is the magnitude of the gravity vector.

3.2.2 Scalar Transport Equations

A custom OpenFOAM solver has been developed to solve this particular variation of the NSE [18]. In this custom solver, temperature and salinity have been added and their transport is solved using the scalar transport eq. (3.3). This equation is for the instantaneous transport of a scalar ϕ, which is either temperature T or salinity S for this problem. The diffusion coefficient for each scalar transport equation is given as k_ϕ and S_ϕ is an optional source term. More on this source term and its determination can be found in section 3.6.

$$\frac{\partial \phi}{\partial t} + \frac{\partial (\phi u_j)}{\partial x_j} = \frac{\partial}{\partial x_j}\left(k_\phi \frac{\partial \phi}{\partial x_j}\right) + S_\phi \tag{3.3}$$

3.2.3 Reynolds–Averaged Navier–Stokes

Solving the previously mentioned full NSE would force all turbulence length scales to be resolved. This would then be a Direct Numerical Simulation (DNS). In order to simplify

the meshing and time-step requirements for such an approach, the RANS equations are implemented. For these equations, all the turbulent length scales are modeled. This is due to taking the long time average of the NSE through a process called Reynolds Averaging. It should be mentioned that this averaging must only be long in comparison to the time scales of the turbulent fluctuations. Therefore unsteady RANS (URANS) is the implementation of the RANS equations for unsteady, time–evolving flows.

Before taking the Reynolds Average, the flow variables must be decomposed into their mean U and fluctuating u' components. The instantaneous values are given in eq. (3.4), with the definition of the mean given by eq. (3.5). Here, T is a time scale chosen to be longer than the largest fluctuations, but shorter than the bulk unsteady motion of the flow. From these definitions, it can be shown that the Reynolds Average of the fluctuations is zero.

$$u = U + u' \tag{3.4}$$

$$U(\mathbf{x}) = \int_{t}^{t+T} u(\mathbf{x}, t)dt \tag{3.5}$$

With a rudimentary understanding of Reynolds Decomposition and Averaging, the RANS equations can be derived. The NSE are first decomposed using Reynolds Decomposition, then the Reynolds time average can be taken. The resulting RANS equations are given in eqns. (3.6-3.7) . The averaging operation is denoted with an over–bar over the variable as $\overline{u}$, and remains for any terms which do not equate to either the mean flow quantity, or zero.

$$\frac{\partial U_j}{\partial x_j} = 0 \tag{3.6}$$

$$\frac{\partial U_i}{\partial t} + \frac{\partial (U_i U_j)}{\partial x_j} = -\frac{1}{\rho_0}\frac{\partial P}{\partial x_i} + \frac{\partial}{\partial x_j}\left(2\nu S_{ij} - \tau_{ij}\right) + \frac{\Delta\rho}{\rho_0} g_i \tag{3.7}$$

The rate of strain, S_{ij}, for the RANS equations is of the same form given for the full NSE, however, the velocity values are the mean values U_i instead of the instantaneous u_i. The velocity and pressure, like in the rate of strain, are now time averaged values. The addition of the τ_{ij} term, given by eq. (3.8), is the only difference between the NSE and RANS equations, minus the notation (e.g., U instead of u). Further investigation of the the second term in the RANS expression for τ_{ij} lends this term to be evaluated to zero, thus cancels out and leaving only the cross–correlation term $\overline{u_i' u_j'}$.

$$\tau_{ij} = \overline{u_i' u_j'} - \overline{u_i'}\ \overline{u_j'} \tag{3.8}$$

The same procedure can be carried out for the instantaneous scalar transport equations. The Reynolds–Averaged scalar transport equation is given by eq. (3.9). The same differences seen in the continuity and momentum equations are noted here, when comparing the instantaneous and RANS scalar transport equations. For the additional term q_j, given by eq. (3.10), it can also be shown that the time average of the fluctuations is zero, again, leaving only the cross–correlation term.

$$\frac{\partial \Phi}{\partial t} + \frac{\partial (\Phi U_j)}{\partial x_j} = \frac{\partial}{\partial x_j}\left(k_\phi \frac{\partial \Phi}{\partial x_j} - q_j\right) + S_\phi \tag{3.9}$$

$$q_j = \overline{\phi' u_j'} - \overline{\phi'}\ \overline{u_j'} \tag{3.10}$$

The cross–correlation terms, for both the momentum and scalar transport equations, cannot be directly calculated and thus are modeled. For this, the linear eddy viscosity model is used, and the expression for both the Reynolds stresses, τ_{ij}, and the scalar fluxes, q_j, are given in eqns. (3.11-3.12), respectively.

$$\tau_{ij} = 2\nu_t S_{ij} - \frac{2}{3} k \delta_{ij} \tag{3.11}$$

$$q_j = \frac{\nu_t}{\sigma_\phi} \frac{\partial \Phi}{\partial x_j} \tag{3.12}$$

For these equations, ν_t is the eddy viscosity, S_{ij} is the mean rate of strain, and k is the turbulent kinetic energy. Calculation of ν_t is done through equation eq. (3.13) with the expressions for k and the specific turbulence dissipation rate ω are provided by the k-ω SST turbulence model, via eqns. (3.14-3.15). A slight variation on the given expression for eddy viscosity is implemented in OpenFOAM's k-ω SST model, which is designed to prevent situations in which ω approaches zero, and thus ν_t approaches infinity.

$$\nu_t = k/\omega \tag{3.13}$$

$$\frac{\partial k}{\partial t} + \frac{\partial (k U_j)}{\partial x_j} = \frac{\partial}{\partial x_j}\left[\left(\nu + \sigma_k \nu_t\right)\frac{\partial k}{\partial x_j}\right] - \tau_{ij}\frac{\partial U_i}{\partial x_j} - \epsilon_k \tag{3.14}$$

$$\frac{\partial \omega}{\partial t} + \frac{\partial (\omega U_j)}{\partial x_j} = \frac{\partial}{\partial x_j}\left[\left(\nu + \sigma_\omega \nu_t\right)\frac{\partial \omega}{\partial x_j}\right] - \tau_{ij}\frac{\partial U_i}{\partial x_j} - \epsilon_\omega + \frac{\sigma_d}{\omega}\frac{\partial k}{\partial x_j}\frac{\partial \omega}{\partial x_j} \tag{3.15}$$

The definition of the dissipation term in the turbulent kinetic energy equation is given in eq. (3.16), with the RANS length scale defined in eq. (3.17). The constant β^* is defined within by the k-ω SST turbulence model.

$$\epsilon_k = \frac{k^{3/2}}{l_{RANS}} \tag{3.16}$$

$$l_{RANS} = \frac{\sqrt{k}}{\beta^* \omega} \tag{3.17}$$

3.2.4 Large Eddy Simulations

Differing from the RANS equations, the LES equations attempt to resolve a specified portion of the turbulent length scales. This results in different mesh and time-step requirements, which are not as strenuous as for DNS but more strenuous than for RANS. Similar to the RANS derivation, the instantaneous values from the NSE are operated on. However, for the LES equations, this operation involves filtering of the turbulent length scales, instead of a time averaging. This filtering is done through an integration given generically by eq. (3.18). The filter function G takes various forms and provides the method for which the turbulent length scales are filtered. Such filters include, but are not limited to, box (also referred to as top-hat), Gaussian, and Fourier cutoff filters. The resultant value U is the filtered component and the subgrid–scales u' are the turbulent length scales that are filtered out from the filter function. The filter length Δ is the length about which the filtering occurs. As an example, taking the simple box filter as the filter function, all turbulent length scales below the set filter length will be filtered out, and thus must be modeled.

$$U(\mathbf{x}, t) = \iiint G(\mathbf{x} - \xi; \Delta) u(\xi, t) d^3\xi \tag{3.18}$$

Like for the RANS derivation, the full NSE are first decomposed into the filtered U and subgrid–scale u' components using the same form given in eq. (3.4) after which the filter operation is performed. The resulting LES equations are given by eqns. (3.19-3.20).

$$\frac{\partial U_j}{\partial x_j} = 0 \tag{3.19}$$

$$\frac{\partial U_i}{\partial t} + \frac{\partial (U_i U_j)}{\partial x_j} = -\frac{1}{\rho_0}\frac{\partial P}{\partial x_i} + \frac{\partial}{\partial x_j}\left(2\nu S_{ij} - \tau_{ij}\right) + \frac{\Delta\rho}{\rho_0} g_i \tag{3.20}$$

These equations closely resemble the RANS equations, however there are a few fundamental differences. First, the velocity and pressure components used are the filtered values, and not

the time averaged ones. This then implies the rate of strain S_{ij} to be the filtered rate of strain, utilizing the filtered components of velocity. Additionally, τ_{ij} is expressed similarly to the RANS equations. However, the filtering operator, given by the tilde over the variables $\widetilde{u}$, is utilized instead of the time averaging. The filtered quantities $\widetilde{u_i'}$ and $\widetilde{u_j'}$, are not value at zero based on their definition, as was determined for the time averaged version. Thus, the second term in τ_{ij} expression, given by eq. (3.21), cannot be canceled out for all filter functions.

$$\tau_{ij} = \widetilde{u_i' u_j'} - \widetilde{u_i'}\ \widetilde{u_j'} \tag{3.21}$$

The same procedure can be carried out for the instantaneous scalar transport equations. The filtered scalar transport equation is given by eq. (3.22). Again, the velocity and scalar here are the quantities that has been filtered and not time averaged. Similar to τ_{ij} from the momentum equations, the second term of q_j cannot be canceled out.

$$\frac{\partial \Phi}{\partial t} + \frac{\partial (\Phi U_j)}{\partial x_j} = \frac{\partial}{\partial x_j}\left(k_\phi \frac{\partial \Phi}{\partial x_j} - q_j\right) + S_\phi \tag{3.22}$$

$$q_j = \widetilde{\phi' u_j'} - \widetilde{\phi'}\ \widetilde{u_j'} \tag{3.23}$$

Again, the linear eddy viscosity model is used, and the expression for both the subgrid Reynolds stresses, τ_{ij}, and the subgrid scalar fluxes, q_j, are determined by eqns. (3.24-3.25), respectively.

$$\tau_{ij} = 2\nu_t S_{ij} - \frac{2}{3} k \delta_{ij} \tag{3.24}$$

$$q_j = \frac{\nu_t}{\sigma_\phi} \frac{\partial \Phi}{\partial x_j} \tag{3.25}$$

For these equations, ν_t is again the eddy viscosity, S_{ij} is the filtered rate of strain, and k is the turbulent kinetic energy. Calculation of ν_t is done through equation eq. (3.26) with the expressions for k given by the *k-equation* turbulence model, given by eq. (3.27). To arrive at these equations for ν_t and k, the box filter function is selected for G, thus all turbulent length scales smaller than Δ will be modeled, and all scales larger than Δ will be resolved, given an appropriate mesh resolution.

$$\nu_t = C_k \sqrt{k} \Delta \tag{3.26}$$

$$\frac{\partial k}{\partial t} + \frac{\partial (kU_j)}{\partial x_j} = \frac{\partial}{\partial x_j}\left[\left(\nu + \sigma_k \nu_t\right)\frac{\partial k}{\partial x_j}\right] - \tau_{ij}\frac{\partial U_i}{\partial x_j} - \epsilon_k \tag{3.27}$$

The dissipation term in the turbulent kinetic energy equation is similarly defined to that of the RANS model, replacing the RANS length scale with the LES length scale, which is defined in eq. (3.28). The *k-equation* LES model defines the constant C_e.

$$l_{LES} = \frac{\Delta}{C_e} \tag{3.28}$$

3.2.5 Hybrid Reynolds–Average/Large Eddy Simulations

For wall bounded flows, such as the JICF, solving the LES set of equations derived in section 3.2.4 would require a much finer wall mesh resolution to resolve the smaller turbulent scales within the boundary layer. This would ultimately drive appropriate time–step sizes to a much lower value than for RANS. For these reasons, solving the LES equations for wall–bounded application–based flows are not applicable. To overcome these challenges, two options are considered. The first is to implement wall modeling within the LES model itself, and the second is to utilize a hybrid RANS/LES model. The former was not investigated but the latter is discussed here and implemented in the simulations presented later.

The derivation of the HRLES equations follow that of LES equations. Thus, the velocity and pressure, seen in eqns. (3.19-3.20), are the filtered components and not the time averaged RANS variables. The difference between a HRLES simulation and an LES simulation is the turbulence model utilized for the turbulence closure. For this a RANS turbulence model is implemented with a modification to the dissipation term of the turbulent kinetic energy, at least in the case of a two–equation turbulence model.

The previously mentioned modification is encompassed in the length scale used to calculate the dissipation term, eq. (3.16). The HRLES length scale is given by eq. (3.29), in which both the RANS and LES length scales are calculated and the minimum value is used in the evaluation of the dissipation term. This modification allows for coarser meshing when compared to the requirements for LES simulations, to occupy flow regions in which only small turbulence scales are present, as seen inside boundary layers. Thus, this allows the turbulence model to mimic a RANS model in these regions and remain an LES model for the remaining portions of the domain.

$$l_{HRLES} = min(\ l_{RANS}\ ,\ l_{LES}\ ) \tag{3.29}$$

The HRLES model selected, for the simulations to follow, is based on the k-ω SST RANS turbulence model. The turbulent kinetic energy and the specific turbulence dissipation rate are given as in eqns. (3.14-3.15), as well as ν_t in eq. (3.13) with the dissipation term of the turbulent kinetic energy equation expressed by eq. (3.30). From the definitions of the RANS and LES length scales, the mechanism by which the HRLES model switches from the LES implementation to the RANS can be better understood. From eq. (3.17), it is shown that the RANS length scale is based on the calculated turbulent length scale, as defined by the k-ω model. The LES length scale, given by eq. (3.28), is calculated based on the filter length, which, for OpenFOAM implementations, is defined based on the local cell size. Therefore, the HRLES length scale determines whether the filter length (e.g., the local cell size) is larger, or smaller, than the local turbulent length scale. If the filter length is small enough to capture the turbulent length scale, the HRLES model will switch to the LES implementation, and if the filter length is larger than the turbulent length scale, the HRLES model will take on the RANS implementation of the turbulent kinetic energy dissipation term.

$$\epsilon_k = \frac{k^{3/2}}{l_{HRLES}} = \frac{k^{3/2}}{min(\ l_{RANS}\ ,\ l_{LES}\ )} \tag{3.30}$$

3.2.6 Equation of State

The density is solved using a linear equation of state (EOS) given by eq. (3.31) with notional constants found in Table 3.1. The scalars, temperature T and salinity S, can also be expressed in a linear fashion, as expressed in eq. (3.32).

$$\rho(T, S) = \rho_0[1 + \alpha(T - T_0) + \beta(S - S_0)] \tag{3.31}$$

$$\begin{aligned} T &= T_0 + \frac{\partial T}{\partial z} z + \Delta T \\ S &= S_0 - \frac{\partial S}{\partial z} z + \Delta S \end{aligned} \tag{3.32}$$

3.3 Numerical Methods

This section outlines the decoupling of the velocity and pressure variables through the PISO Algorithm. Next the temporal and spatial discretization are outlined, along with the details of each of the specific schemes used. Following the discussion of the schemes, the linear solvers used for each equation are detailed.

Temperature $[°C]$		Salinity $[PSU]$	
α	-2.1×10^{-4}	β	7.6×10^{-4}
T_0	20	S_0	36

Table 3.1: Notional constants for a linear EOS.

3.3.1 The PISO Algorithm

To solve the NSE for this problem, the velocity and pressure are decoupled through the Pressure–Implicit with Splitting of Operators (PISO) Algorithm [24]. This method reformulates the momentum equations to the one seen in eq. (3.33). Here all the terms with a velocity component are displayed on the left–hand side, and the remaining source terms are presented on the right–hand side. This allows the momentum equations to be written in matrix form as eq. (3.34). This form encompasses the three velocity components for all cells within the domain.

$$\frac{\partial U_i}{\partial t} + \frac{\partial (U_i U_j)}{\partial x_j} - \frac{\partial}{\partial x_j}\left(2\nu S_{ij} - \tau_{ij}\right) = -\frac{\partial \hat{P}}{\partial x_i} + \rho_k g_i \tag{3.33}$$

$$M\mathbf{U} = \mathbf{B} \tag{3.34}$$

For completeness, the definition of both $M\mathbf{U}$ and $\mathbf{B}$ are shown in eqns. (3.35) and (3.36), respectively. Some notational differences are used in these equations from the ones previously shown. Here $\hat{P}$ is the pressure divided by the density and ρ_k is the density difference (e.g. $\Delta\rho = \rho - \rho_{BG}$) divided by a reference density ρ_0. The τ_{ij} can be defined by either the RANS or LES turbulence model.

$$M\mathbf{U} = \frac{\partial U_i}{\partial t} + \frac{\partial (U_i U_j)}{\partial x_j} - \frac{\partial}{\partial x_j}\left(2\nu S_{ij} - \tau_{ij}\right) \tag{3.35}$$

$$\mathbf{B} = -\frac{\partial \hat{P}}{\partial x_i} + \rho_k g_i \tag{3.36}$$

Further decomposing of the $M\mathbf{U}$ yields the diagonal terms, given by the A matrix, as well as the $\mathbf{H}$ matrix, which consists of the remaining terms not given inside the A matrix. The form of this decomposition is given in eq. (3.37). The $\mathbf{H}$ matrix can then be found by using eq. (3.38).

$$M\mathbf{U} = A\mathbf{U} - \mathbf{H} \tag{3.37}$$
$$\mathbf{H} = A\mathbf{U} - M\mathbf{U} \tag{3.38}$$

Setting eq. (3.37) equal to eq. (3.36) the solution for $\mathbf{U}$ can be found as eq. (3.39).

$$\mathbf{U} = A^{-1}\mathbf{H} + A^{-1}\mathbf{B} \tag{3.39}$$

Substituting this expression into the continuity equation, rearranging terms, and expanding $\mathbf{B}$, eq. (3.40) can be found. This expression is the pressure Poisson equation.

$$\frac{\partial}{\partial x_i}\left(A^{-1}\frac{\partial P}{\partial x_j}\right) = \frac{\partial}{\partial x_i}\left(A^{-1}\mathbf{H} + A^{-1}\rho_k g_i\right) \tag{3.40}$$

With the background on the decomposition of the NSE for the PISO method understood, the actual implementation of the PISO algorithm can be discussed. Following are the steps taken from within the PISO method.

1. Set the boundary conditions
2. Solve Momentum Predictor (i.e., eq. (3.34)) using initial or previous pressure value
3. Solve Scalars (Temp. and Salinity) and Calculate ρ_k from the selected EOS
4. Calculate the fluxes ϕ and $\mathbf{H}$ vector
   - $\phi = (A^{-1}\mathbf{U} + A^{-1}\rho_k g_i) \cdot A_f \ \hat{n}$
5. Solve the pressure Poisson equation (i.e., eq. (3.40)); the fluxes are used here instead of the right–hand side of the equation
6. Repeat step 5 for n number of non-orthogonal correctors ($n = 1$ for the simulations to follow)
7. Correct the fluxes ϕ for consistency
8. Update the Velocity with eq. (3.39)
9. Correct the boundary conditions
10. Repeat steps 4 - 9 for a total of m number of inner loops ($m = 2$ for the simulations to follow)
11. Solve the turbulence equations and calculate the eddy viscosity
12. Step forward in time by Δt and repeat from 1

3.3.2 Temporal Discretization

The backwards temporal discretization scheme was selected for the discretization of all temporal terms. The backward difference scheme in OpenFOAM is defined by eq. (3.47) where ϕ^0 is the value at the previous time-step, and ϕ^{00} is the value at the time-step before the previous. Initially, $\phi^0 = \phi^{00}$, so that the numerical iterative process can begin. This scheme is denoted as being second order accurate.

$$\frac{\partial \phi}{\partial t} = \frac{1}{2\Delta t}(3\phi - 4\phi^0 + \phi^{00}) \tag{3.41}$$

3.3.3 Spatial Discretization

To discretize the spatial terms within the NSE, the cell-centered values are interpolated to the faces. For some schemes, the gradient of a value is also interpolated to the faces. A depiction of this can be seen in Figure 3.1, with P denoting the owner cell, N denoting the neighbor cell, and f denoting the face to which the the cell values (from P and N) are interpolated to. The distance between the cell centers is referenced by $\vec{d}$, also denoted as $\mathbf{d}$, with the distance from the owner cell center to the face shown as $\vec{r}$, and also $\mathbf{r}$.

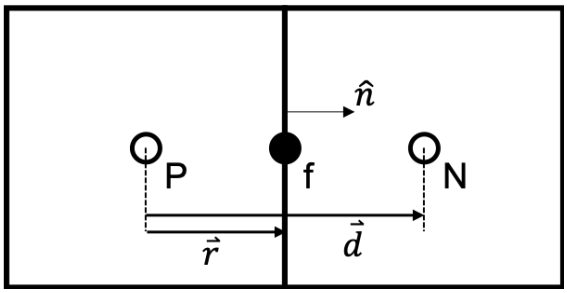

Figure 3.1: Diagram for a pair of cells with a shared face which is used to visually represent some parameters to be mentioned.

The simplest discretization comes from assuming the values are constant throughout each cell. From this, the value at the face, ϕ_f, can either be taken as the cell value of the owner, ϕ_P, or of the neighbor cell, ϕ_N. To determine which cell the face value is taken from, the volume flux F_f through the face is calculated through eq. (3.42). The area of the face A_f, unit normal $\hat{n}$, and the velocity at the face U_f is required for these calculations. The formulation of the upwind discretization scheme can then be expressed as in eq. (3.43). Since the values are assumed to be constant across the cells, the upwind scheme is first order accurate. This scheme was not directly used to discretize any of the terms in the NSEs, but instead is used as a partial calculation for a later defined scheme.

$$F_f = A_f(\mathbf{U}_f \cdot \hat{n}) \tag{3.42}$$

$$\phi_f = \begin{cases} \phi_P \ , & F_f > 0 \\ \phi_N \ , & F_f < 0 \end{cases} \tag{3.43}$$

The most accurate spatial discretization scheme offered in OpenFOAM is the linear scheme. This scheme assumes that the values vary linearly across the cell. To calculate the face value, a linear interpolation is implemented using eq. (3.44), where Ψ is the distance from the owner's cell center to the face and is divided by the distance between the cell centers. See eq. (3.45) for the expression for the Ψ term used in the interpolation.

$$\phi_f = \Psi\phi_N + (1 - \Psi)\phi_P \tag{3.44}$$

$$\Psi = \frac{|x_f - x_P|}{|x_N - x_P|} = \frac{|\mathbf{r}|}{|\mathbf{d}|} \tag{3.45}$$

With a basic understanding of the most dissipative and the most accurate schemes OpenFOAM has to offer, the scheme selection for the various terms in the NSE can be broken down and discussed. Table 3.2 lists the various terms for each of the equations solved, as well as the scheme, in OpenFOAM notation. The order of each scheme will be discussed in the following section, but is also place in parentheses inside the table for easier comparison.

ϕ	$\partial(\phi)/\partial t$	$\partial(\phi u_i)/\partial x_i$	$\partial(\phi)/\partial x_i$	$\partial^2(\phi)/\partial x_i \partial x_j$
Momentum	Backward (2)	Filtered-Linear (1.8)	-	Corrected-Linear (2)
Pressure	-	-	Limited-Linear (2)	Corrected-Linear (2)
Turb.	Backward (2)	Linear-Upwind (2)	-	Corrected-Linear (2)
Scalar	Backward (2)	Linear-Upwind (2)	-	Corrected-Linear (2)

Table 3.2: Tabulated OpenFOAM specific schemes for equation specific terms with the approximate order in parentheses.

3.3.4 Cell-Limited Linear Spatial Discretization

For the discretization of the gradient terms, specifically the pressure gradient in the momentum equations, the Cell-Limited Linear scheme is implemented. This scheme has two separate components that are implemented within. First is the calculation of the face value

$(\phi_f)_0$. This is not limited to the linear scheme, however for these calculations, the linear scheme previously mentioned was used. After an initial face value was calculated, this value is then limited to keep it within the values of the owner and neighbor cells surrounding the face.

$$\phi_f = min\Big[max\Big((\phi_f)_0, min(\phi_P, \phi_N)\Big), max(\phi_P, \phi_N)\Big] \tag{3.46}$$

3.3.5 Linear-Upwind Spatial Discretization

The divergence terms for the turbulence and scalar variables utilize the Linear-Upwind scheme. This scheme is a modification of the Upwind scheme, from eq. (3.43), with a second order, gradient corrector. Similar to the Upwind scheme, the Linear-Upwind scheme the volume flux is used to determine which cell values to use in the interpolation. This scheme calculates the face value from eq. (3.47). Here, $\nabla\phi$ is the calculated gradient at the respective cell center which is calculated using the same Cell-Limited Linear scheme used for the pressure gradient calculations, as previously discussed.

$$\phi_f = \begin{cases} \phi_P + (\nabla\phi)_P \cdot \mathbf{r}\ , & F_f > 0 \\ \phi_N + (\nabla\phi)_N \cdot \mathbf{r}\ , & F_f < 0 \end{cases} \tag{3.47}$$

3.3.6 Filtered-Linear Spatial Discretization

The momentum divergence terms are discretized using a Filtered-Linear scheme. This scheme has the capability of limiting the over/under shoot of the face value interpolation, which is proportional to the difference between the owner and neighbor cell values. There is also the ability to blend the Upwind, first order scheme, with the Linear, second order scheme.

The over/under shot is controlled through the setting of the l variable inside the coefficient β defined by eq. (3.49). Setting $l = 0$ will not allow any over/under shoot and setting $l = 1$ will allow the maximum over/under shoot to be equivalent to the difference between the cell values. The order of the scheme is set through varying the k coefficient inside eq. (3.49). The order of the scheme is set through the k variable. Setting $k = 0$ with no over/under shooting (i.e., $l = 0$) will result in $\phi_f = (\phi_f)_{lin}$, the result from the linear scheme. Fully-limiting this scheme is done by setting $k = 1$ where the full magnitude of the fractional portion of the β coefficient is utilized in calculating the blending coefficient, β.

As previously mentioned, the order of this scheme can vary from first to second order. For the simulations to follow, the values $l = 0$ and $k = 0.2$ were used for all the momentum divergence terms. Gathering that the β coefficient can be no larger than one, the approximate order can

be estimated for the implemented scheme. From this, $\beta \approx 0.8$, and thus the final form of the face interpolated values would be similar to $\phi_f = 0.2(\phi_f)_{up} + 0.8(\phi_f)_{lin}$. The approximated order from this definition of the face values is about 1.8.

$$\phi_f = (\phi_f)_{up} + \beta[(\phi_f)_{lin} - (\phi_f)_{up}] \tag{3.48}$$

$$\beta = 1 + l - k\frac{min\Big(max(\delta\phi - \overline{\nabla\phi_P}, 0)\ ,\ max(\delta\phi - \overline{\nabla\phi_N}, 0)\Big)}{max\Big(|\delta\phi|\ ,\ max(|\overline{\nabla\phi_P}|, |\overline{\nabla\phi_N}|)\Big)} \tag{3.49}$$

3.3.7 Corrected-Linear Spatial Discretization

For all the Laplacian terms, the Corrected-Linear scheme is implemented. Since the definition of the Laplacian in the finite volume method, eq. (3.50), utilizes the gradient of the value at the face, the gradient is interpolated, and not the value.

$$\nabla \cdot (\Gamma \nabla\phi) = \frac{1}{V}\sum_{i}^{N}(\nabla\phi)_{f,i} \cdot \Gamma(A\hat{n})_{f,i} \tag{3.50}$$

$$(\nabla\phi)_f^{\perp} = \alpha\frac{\phi_P - \phi_N}{|\mathbf{d}|} + (\hat{n} \cdot \alpha\mathbf{d}) \cdot (\nabla\phi)_f \tag{3.51}$$

3.3.8 Linear Solvers

Each of the equations mentioned previously are formulated into the matrix system $A\mathbf{x} = \mathbf{b}$. In order to solve this system, linear solvers are implemented to iteratively solve each equation. The pressure Poisson equation is solved using the Preconditioned Conjugate Gradient (PCG) solver while the Preconditioned Bi–Conjugate Gradient (PBiCG) solver is used to solve the remaining equations: momentum, scalars, and turbulence quantities. A minimum of one iteration is used for each equation, with a maximum of 1000 iterations per equation per solve. This is to ensure that all variables are updated at each time step and to limit the number of iterations to ensure no infinite loops occur. The residual tolerances for these iterative methods were set at 10^{-5} for pressure and 10^{-8} for all other equations.

3.4 Boundary Conditions

To solve the mathematical model on a discrete finite volume grid, boundary conditions are needed to ensure that the numerical methods have enough information to solve the mathematical model near the edges of the domain. A brief overview of the relevant boundary types and their associated boundary conditions are presented here.

3.4.1 Definitions

Defining individual boundary conditions will help in the overall understanding of the boundary types to be listed and referenced later. This section outlines the boundary conditions used and provides a basic definition of each boundary condition.

Zero-Gradient The zero-gradient condition, as the name suggests, forces the gradient of the variables applied to, to be zero on the specified boundary. This condition can be applied to both scalar and vector variables.

Fixed Value The fixed value condition specifies the value of a given variable at the applied boundary. This value is fixed in time, and uniform in space. This condition can be applied to both scalar and vector variables.

GroovyBC The GroovyBC condition is similar to the fixed value condition in that a value for a given variable is specified at the applied boundary. However, this boundary condition does not have the limitations of being fixed in time, nor does it require the value to be uniform in space. Instead, this conditions takes a function and applies it to all boundary faces, at every time–step. This condition can be applied to both scalar and vector variables. *It should also be noted that this boundary condition does not come standard with the OpenFOAM package but with Swak4Foam, a package built to increase OpenFOAM's functionality.*

Wall Functions The wall function condition is specifically for scalar turbulence variables. Each variable has a different function defining the actual condition, but the general idea is to use a specified function to blend the free–stream turbulence value to the wall value. This condition can only be applied to the specific turbulence variables the wall function was designed for. For LES simulations, wall functions are generally not used. Instead a wall-value is specified, with adequate wall spacing assumed.

Slip The slip condition mimics that of the zero-gradient condition for scalars, however, for vectors, only the tangential components have the zero–gradient condition applied to them. The normal component of the vector is set to zero, and thus holding a zero–flux condition. This condition can be applied to both scalar and vector variables, however when used for scalars, it is analogous to the zero–gradient condition. *The slip condition is useful when simulating walls in non–viscous simulations.*

No–Slip The no-slip condition is a specific variation of the fixed value condition for vector

variables, where all components are specified to be zero. This condition can only be applied to vectors. *The no–slip condition is useful when simulating walls in viscous simulations.*

3.4.2 Boundary Types

Boundary types mentioned earlier will be presented, for this thesis, as groupings of boundary conditions which, when used together, mimic a realistic occurrence.

Inlet The inlet boundary type is equivalent to an inflow of a fluid. This being where all variables are known. However, due to the nature of the PISO Method, mentioned previously, the velocity and pressure cannot both be specified. Therefore, for the inlet boundary patch, the pressure is set to utilize a zero–gradient condition and all other variables are specified, either using the fixed value, slip, or GroovyBC condition.

Outlet The outlet boundary type is quite the opposite of the inlet boundary type. This would be the uncontrolled outlet of a fluid, where only pressure is specified, and all other variables utilize the zero-gradient condition.

Wall The wall boundary type is setup to simulate an impenetrable wall inside the simulation thusly forcing all turbulence values to utilize their respective wall function (or wall values for LES), velocity to either use the slip (for non–viscous simulations) or no–slip (for viscous simulations) condition, and all other variables to utilize the zero-gradient condition.

Far-field The far–field condition is a boundary type that is meant for boundaries that are placed relatively far away from most flow features. This inherently eliminates the wall boundary type and prohibits the usage of an inlet or outlet boundary type. This is not to say that flow cannot flow through this boundary type it is just not its intended purpose. For these reasons, all flow variables utilize the zero–gradient condition on these boundary types.

3.5 Initial Conditions

In a similar manner to boundary conditions, CFD solvers require an initial condition, or an initial guess, to the mathematical model for which the numerical methods use as a starting point. The dependency of the initial conditions on the overall CFD results depends on the numerical methods used. The basis behind initial condition selection is dependent on the physics to be solved, and the overall problem the CFD solver will be handling. Spatially constant free–stream values can be used to initialize the finite volume domain and the numerical methods are marched enough to allow the mathematical model to attempt to correct these initial guesses. This is the simplest approach to setting initial conditions, however, it can extend simulation time or inaccurately define the problem. For the specific cases discussed later in this thesis, the spatially variation of initial conditions as these simulations

have variable stratification profiles, requiring the use of non-uniform initial conditions.

3.5.1 Spatial Variations

In the context of the work presented, there are two main reasons why spatial initial conditions are desired. The first is to initialize the background fields creating the environmental stratification. The second is to initialize the basic flat plate boundary layer. Initializing a basic boundary layer profile gives a more accurate initial condition and also reduced computational cost of propagating the boundary layer though the entire domain. For both of these conditions, a Third–Party package called, swak4Foam, is utilized [19]. This package has many features specifically designed to increase the overall functionality of the OpenFOAM CFD Toolbox. Specifically, a function called funkySetFields allows any variable to be set to a wide variety of spatial (or temporal) functions.

The funkySetFields function takes an input of the specific field to be manipulated and an expression to apply to the selected field. There is also an optional input to set conditions, spatially and temporally, on the application of the expression. Upon running the funkySetFields function, the inputs are read and the cells of the mesh are then looped over. Each cell's value is then set based on the supplied conditional statement and the supplied expression.

3.6 Point Sources

Briefly mentioned in section 3.2.2 was the addition of a source term in the scalar transport equations. The addition of these source terms is to allow point sources to be added to simulations without the requirement of a complex mesh with addition boundaries ultimately creating a similar effect. Despite requiring less complex of a mesh to implement, the addition of sources in this manner requires a more complex definition than simply setting the scalar value, as when utilizing a more complex mesh with additional boundary conditions. The formulation of this source term depends on the scalar on which this source is being applied. Since the source term determination is dependent on the scalar itself, and only a temperature (i.e., heat) source is used for the point heat source simulations of Chapter 4, the determination of a point source for the temperature transport equation will be outlined.

Before proceeding with the determination of the source term, the definition of a point source should be stated. In an absolute sense, a point source would be a source applied at a single, infinitesimally small point. However, in a practical sense, a point source would more accurately refer to a given volume, centered at a point, through which the source is applied. Thus, in determining a source term, the volume to which this source is applied should be determined. For the remainder of this section, the source term referred to will more specifically be a source term to the temperature transport equation, or more simply, a thermal source. To determine the definition of a thermal source, two additional quantities

are necessary. First, the energy released by the point source per unit time (i.e., power) and the specific heat of the fluid the source is placed in, are required. Due to specific heat capacities having units of mass and not volume, the density of the fluid is also required. The determination of the required quantities, outside the volume of the source, are again dependent on the scalar quantity itself.

Once the necessary quantities that determine the source term are obtained, the relationship between these quantities is needed. For this the Buckingham Π Theorem is used [6]. The selection of the source term S_T as the independent variable, while the dependent variables consist of the quantities previously mentioned: the volume of the source V, the power supplied to the source P, the specific heat capacity of the fluid C_h, and the fluid density ρ. From Table 3.3, the number of base units is found to be four, giving rise to a reduction of four. With 5 parameters, the number of Πs to be found is $5 - 4 = 1$. To find this relationship, Π, it is recognized that $S_t = f(P, C_h, \rho, V)$ and the exponents (a-d) of eq. (3.52) can be solved using dimensional analysis. The result is an expression for the thermal source term, eq. (3.53). For a more in–depth analysis on the process, see Appendix A.

$$S_T = (P)^a (C_h)^b (\rho)^c (V)^d \tag{3.52}$$

$$S_T = \frac{P}{C_h \rho V} \tag{3.53}$$

Variable	S_T	V	P	C_h	ρ
Units	θ/T	L^3	ML^2/T^3	$L^2/T^2\theta$	M/L^3

Table 3.3: Base units for variables used in Buckingham Pi analysis.

Chapter 4

Point Heat Source

In this section, the V&V philosophy is outlined by providing definitions and a brief mention of their background. Afterwards the overall outline of experimental design, simulation design, and other metrics needed to complete the V&V process, are given. This is a necessary step in strengthening the extrapolation capabilities of the solver and simulation techniques previous outlined.

4.1 Verification & Validation Philosophy

In this section, a basic understanding of the author's usage of both terms, verification and validation, are given before the overall implementation of the V&V process is outlined. This can be worthwhile as there are various definitions of these terms depending on the application and the reference used to define these terms. To further illustrate the variability of these definitions, the author's definitions are prefaced with a dictionary definition followed by definitions adopted by the IEEE in the 2011 drafting guide [23].

To begin, the dictionary definition of **verification** is *the process of establishing the truth, accuracy, or validity of something.* **Validation** is defined as *the action of checking or proving the validity or accuracy of something.* These definitions, however, are not a helpful combination as, upon further inspection, these definitions seem to overlap. This comes from the usage of the word *action* in the definition of validation. An **action** refers to *the fact or process of doing something*, which when replaced in the definition of validation, the dictionary definitions of both terms overlap.

However, for most scientific applications, these two terms have generally been accepted to hold different meanings. One reference for these terms can be found in the IEEE draft guide from 2011, mentioned above [23]. Here the definition for verification and validation are more specific and have a distinction between them. **Verification** is defined as "*the evaluation of whether or not a product, service, or system complies with a regulation, requirement, specification, or imposed condition*". It is also noted that verification is generally something internal thus excluding outside interventions. **Validation** is said to be "*the assurance that a product, service, or system meets the needs of the customer and other identified stakeholders*". Validation is said to contrast verification and include direct intervention with external parties.

Specifically for computational mechanics, and for the context of the work presented here, verification and validation have a more specific definition than those proposed by the IEEE in their draft guide. Not only do these definitions differ, but they also complement each other. This ultimately means that both verification and validation must be performed to access the computational mechanics process being carried out. First, **verification** is "*the process of accessing the accuracy of the model implementation and its ability to solve the mathematical model*". This is done by checking for implementation errors, inconsistencies in algorithms, and accessing errors such as round-off, iterative, and discretization. While **validation** is "*the process of accessing the mathematical model's ability to predict the physics it was modeled after*". The most common way to perform validation for computational mechanics problem is to compare the results with experimental studies. With the basic understanding of the definitions used for the V&V process, the process itself is outlined.

4.2 Experimental Validation Data

As previously mentioned, comparison with experimental data plays an important role in accessing the accuracy of a computational mechanics process. For this reason, experimental data was sought after in order to access the mathematical model described in section 3.2. The main focus for this investigation, was to access the math model's ability to accurately capture the buoyancy affects that were introduced through the Boussinesq approximation. With this in mind, the search for experimental data was focused on experimental data of a buoyancy driven flow in a stratified environment, as the desired JICF simulations are also placed inside a stratified environment. The search was not limited to jets as this V&V assessment focuses on the buoyancy terms in the mathematical model, not the momentum terms. No experiments that fit the necessary guidelines, also incorporating jets, were found. For this reason, the 1981 experiments of Tupitsyn and Chashechkin [48] was selected as the validation experiment to access the computational model outlined in Chapter 3.

For their experiments, Tupitsyn and Chashechkin filled an optical glass tank with layers of salt water. The dimensions of the tank are 1.5 x 0.4 x 0.4 meters. The salt concentration in each of the layers are such that a stable stratification was produced. Once an allotted amount of time passed, the layers diffused into an approximately linear stratification profile. This procedure was used in creating three different stratification profiles used in various experimental seetups. The EOS recognized for these experiments was linear and of the form seen in eq. (4.1). Other notable fluid properties are shown in Table 4.1.

$$\rho = \rho(T, S) = \rho_0[1 - \alpha(T - T_0) + \beta(S - S_0)] \tag{4.1}$$

After the tank was filled, a "two–electrode coaxial cell" was used to heat the water in a specific region of the tank, thus acting as a point source [48]. The dimensions of the heated

Variable	Value
α	$3 \times 10^{-4}\ K^{-1}$
β	$7 \times 10^{-4}\ PSU^{-1}$
ν	$1 \times 10^{-6}\ m^2/s$
χ	$1.43 \times 10^{-7}\ m^2/s$
k_S	$1.41 \times 10^{-9}\ m^2/s$

Table 4.1: Fluid properties and their values presented by Tupitsyn and Chashechkin [48].

region were not precisely measured, but are said to follow these guidelines. First, the heated region is assumed to be spherical. Secondly, this spherical region's diameter is not to exceed five times that of the diameter of the smaller, inner electrode of the coaxial cell heating element. Lastly, the heated region is stated to contain 90 percent of the released energy within its bounds. The specific location of the resultant point source is not mentioned, but is assumed to be centered inside the tank. This is a reasonably safe assumption as the region of influence of the source is roughly an order of magnitude smaller than the tank dimensions. This assumption also maximizes the distance, in all directions, between the point source and any given surface.

The power used to drive the coaxial heating element, was measured using the ammeter-voltmeter method with a stated error of two percent. However, no calculations of the loses inside the heating element were given. For this reason, the measured power might not be equivalent to the power added to the water near the coaxial cell, either due to electrical or other loses. In order to record the temperature fluctuations inside the water tank, a thermocouple was used with the cold junction placed against the side of the tank, at the same vertical location as the measurement. The measurements were stated to have a measured error of $0.1K$. Changing the location of these temperature measurement, was done using a "coordinate–rotation device above the [tank]" is used [48]. This device allows the thermocouple to be placed at any location within the tank with a recorded error of $0.1mm$. As previously discussed, setting up the stratification profile involved setting multiple layers of fluid inside the water tank, each with a different concentration of salinity. After a set time elapsed, these layers diffused to form a constant salinity gradient. This was done for each of the three different environmental profiles studied. For a more in-depth information about the experimental setup, see Tupitsyn and Chashechkin's 1981 paper on their experiment [48].

A compilation of all experiments run by Tupitsyn and Chashechkinis given in Table 4.2. Included is the measured power, the maximum time the experiment was ran for, the stratification strength λ and the corresponding internal Froude number Fr, calculated using eq. (4.3). Using the information found previously in section 3.2 and noting the absence of a temperature gradient in these experiments, the density profile, and thus the gradient, can be calculated. This table also includes the types of results provided for each experimental run.

The images provided are shadowgraphs, and from these, circulation zones were identified with the height and width of these regions recorded. Finally, vertical and horizontal data plots of the temperature were given for a select number of experimental runs.

$$\lambda = \left(\beta \frac{\partial S}{\partial z}\right)^{-1} \tag{4.2}$$

$$Fr = \frac{U_0}{2\pi}\left(\frac{g}{\rho_0}\frac{\partial \rho}{\partial z}\right)^{-1/2} \tag{4.3}$$

Case	Power(W)	$t_{max}(s)$	$\lambda(m)$	Fr	Images	Cell-Sizes	Plots
1	0.6	300	400	12.5	yes	no	no
2	1.5	4500	15	2.5	no	yes	yes
3	4.2	180	15	2.5	no	yes	no
4	5.1	2400	15	2.5	no	yes	no
5*	5.3	288	15	2.5	no	no	yes
6	5.9	600	15	2.5	yes	no	no
7	23	30	15	2.5	yes	no	no
8	66	60	15	2.5	yes	no	no
9	3.2	3000	4.4	1.25	yes	yes	no

Table 4.2: Tabulated list of the properties used for the experiments presented in Tupitsyn and Chashechkin's paper. Appended to the right of the experimental parameters, are the data results given for each experiment. Froude Number is calculated assuming a fluid speed of 2.0 m/s. (*experimental case used for validation)

4.3 CFD Simulation

In this section, the simulation setup for the point heat source (PHS) used to compare with the experimental data from Tupitsyn and Chashechkinis outlined. To start with, the computational domain is discussed, followed by the boundary and initial conditions, and finishing off with the specification and considerations for the point source generation. A depiction of the simulation domain can be seen in Figure 4.1.

4.3.1 The Computational Domain

The computational domain was selected to encompass the entirety of the experimental domain. In using this approach, no approximations or errors, due to improperly selected

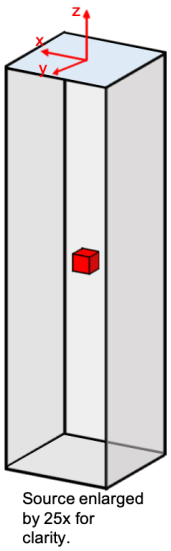

Figure 4.1: Depiction of the PHS problem setup.

boundary conditions, were introduced into the simulation results. The local coordinate system for the computational domain is centered on the top surface with the positive z axis pointing upward, out of the tank. With the overall dimensions of the domain set, the location of the point source can be defined. This follows the same logic explained in section 4.2, where the source's origin point is centered in the tank. This corresponds to a local point location of $(x, y, z) = (0, 0, -0.75)\ m$. Along with the location of the source, the sizing of the source volume is required. This is not discussed here, however, more in–depth discussion is provided in section 4.3.3. For now, we can arbitrarily assign a volume over which the point source will act, noting that the center of this volume is set by the experimental setup, previously mentioned.

To ensure the ability of the computational domain to resolve the resultant flow features caused by the PHS, a set number of cells are placed across the source volume in all coordinate directions. After which, the cell size is grown away from the source with a growth rate of 1.15 until the outer limits of the computational domain are reached. This resultant volume is then a structured domain filled with hexahedron cells having zero skewness. The number of cells across the point source, n, varies depending on the domain resolution, and is shown, for all computational domains used, in Table 4.3. Other domain metrics, such as total cell count and maximum cell volume, are also given in this table to help differentiate the various computational meshes used.

Domain	Cells	n	$max(\frac{V_{cell}}{V_{total}})$	AR_{MAX}
coarse	0.725	20	0.08%	956
medium	2.344	28	0.03%	1324
fine	7.614	40	0.012%	2030

Table 4.3: Table of PHS computational domain metrics for comparison. *Cell count in millions.*

4.3.2 Boundary and Initial Conditions

With a computational domain set, boundary and initial conditions are selected to best match the experimental setup. For this problem, only two boundary types were utilized. The first being the walls that make up five of the six sides of the simulation domain. For these boundaries, the wall boundary type, mentioned in section 3.4, can directly be implemented. The remaining boundary is one that was not previously mentioned and is designed to mimic that of a free-surface. For this boundary, the outlet boundary type, described in section 3.4 is modified such that the velocity normal to the boundary surface is zero, i.e., using the slip boundary condition. This is suitable since little to no free-surface disturbances are expected as the PHS's influence is far enough away to not interfere with this boundary. The boundaries and variables of the PHS problem are tabulated in Table 4.4 with their respective boundary conditions.

Field	Patch		Initial Conditions
-	Free-Surface	Walls	-
U	Slip	No-Slip	$(0, 0, 0)$
p	0	$\nabla\phi = 0$	0
T	$\nabla\phi = 0$	$\nabla\phi = 0$	20
S	$\nabla\phi = 0$	$\nabla\phi = 0$	$36 - \frac{\partial S}{\partial z}z$

Table 4.4: Table of boundary and initial conditions for the PHS simulations.

It is at this point that the turbulence model selection should be discussed. In order to properly test the implementation of the Boussinesq approximation, no turbulence model was selected. This decision was in an effort to minimize the error sources introduced into the V&V simulations. In OpenFOAM, this is forced by setting the eddy viscosity ν_t in the Reynolds Stresses and the scalar turbulence fluxes to be zero.

4.3.3 Source Specification

Since no diagram of the coaxial cell was provided by Tupitsyn and Chashechkin, Figure 4.2 illustrates a best guess at the configuration of the coaxial cell. This illustration steams from the three conditions imposed on the point source generation, which were described in section 4.2. The source diameter, $5d$ in the figure, is given as a maximum estimate for the source diameter, however, the actual diameter was not recorded by Tupitsyn and Chashechkin. The supplied dimensions were 20 mm as the overall diameter D and 0.5 mm for both the protruding length l and the maximum inner electrode diameter d. With this information, the spherical source's diameter is calculated to be 2.5 mm. For preliminary testing, a cubic source was specified with a side length equal to $5d$. The magnitude of the calculated source term was decreased proportional to the increased volume of the computational source over the proposed experimental source. However, the source term was not changed to a spherical shape due to preliminary results giving fairly good agreement to the experimental results. This, coupled with a relatively high uncertainty in the experimental measurements and setup, would result in a much higher computational cost, when compared to the knowledge gained from rerunning these simulations. The methodology of generating the source term and the final expression, can be directly taken from section 3.6.

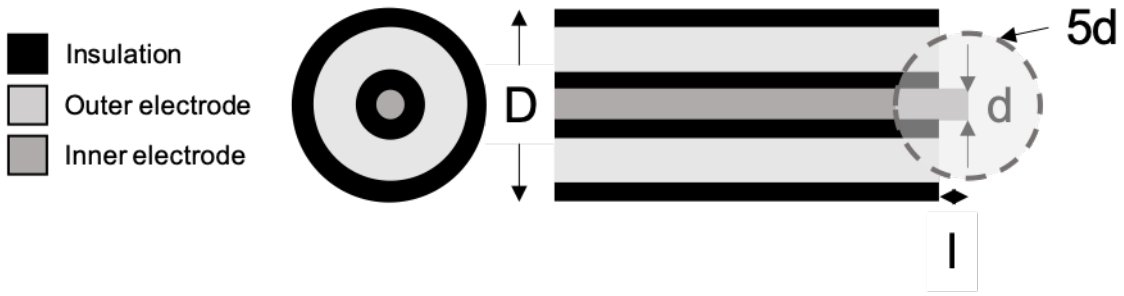

Figure 4.2: (left) Axial and (right) centerplane cross–cut illustrations of the coaxial cell used to generate the PHS in Tupitsyn and Chashechkin's experiment.

4.3.4 High–Performance Computing

Due to the high computational costs, seen in Table 4.5, a simple desktop machine is not feasible to utilize when running such simulations. The coarsest simulation, taking 835 CPU hours on 48 processors would take close to a full week, running on an eight–core desktop machine. The finest simulation, taking over 30 thousand CPU hours on 384 processors would take almost five months on the same machine. For this reason, running simulations, such as the ones presented here, are essentially required to run on high–performance computing (HPC) machines. The Air Force Research Laboratory's HPC cluster Mustang, was utilized for all the PHS computations shown here. This allowed the much shorter turnaround time of

no more than four days per simulation, for the finest simulation, with an average turnaround time of just over two days for each simulation.

Noting that the refinement factor for the time-steps is $r = \sqrt{2}$, when examining the computational times presented in Table 4.5, it is seen that, while holding the spatial discretization and the number of processors the same, the increase in computational time spent is proportional to the time-step refinement factor. This claim cannot be said for the variations in spatial discretization, however, the number of cells per processor varies for the coarse, medium, and fine grid simulations. This variation in the distribution of cells has an unclear effect on the increase in computational time spent, when comparing simulation with varying grids. The increase in computational costs for the grids would be expected to be proportional to the cube of the grid refinement factor, which also happened to be $r = \sqrt{2}$. Thus the estimated increase should be approximately $r^3 = 2.83$, instead the increase was noted to be between five and seven times.

Case	Grid	Time-Step (s)	Cores	CPU Time (hrs)
1	Coarse	0.001	48	835
2	Medium	0.001	96	4,668
3	Fine	0.001	384	31,444
4	Fine	0.002	384	17,160
5	Fine	0.001414	384	23,174

Table 4.5: The number of processors utilized and the overall computational time, in hours, for the PHS simulations.

4.3.5 Data Extraction

In order to perform the validation procedure later discussed, data from the experiments performed by Tupitsyn and Chashechkin is needed. Due to the lack of quantitative information given from the image results, they were not selected as good metrics to validate against. For similar reasoning, the cell-sizes, calculated from the still images, were decided not optimal when compared to the data plots that Cases 2 and 5 offered. The main differences between these cases are the power induced, maximum run time, and the number of data points. The latter being the most relevant difference and one of the deciding factors for the selection of the validation experiment. Since Case 5 has twice the data plots that Case 2 has, it is a more optimal validation comparison.

With the case selected, the available data for said case was examined and all simulations were sampled at the same locations as the experimental measurements. Figure 4.3 depicts the simulation at its final run time with a close–up of the data extraction planes. Data was also extracted on the centerline of these planes. A sample of these plots are shown as Figures 4.6 and 4.7, with the remaining figures presented in Appendix B.1. The experimental data

from this specific experiment has been extracted and plotted alongside the simulation data. Along the extraction lines, 8 radial locations were sampled where experimental data was also available. Table 4.6 lists the vertical locations for the line sampling, as well as the radial positions for the data points and the label for which the respective extraction location will be referred as for the following sections. These data points will be used in the error calculation presented in the following sections.

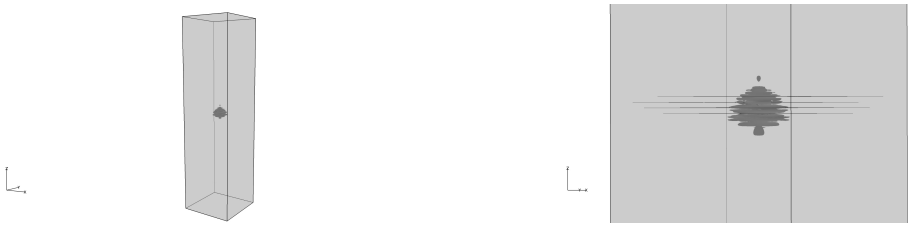

(a) (b)

Figure 4.3: Depiction of the PHS simulation at the final simulation time. (a) Full size domain and (b) close–up of source with data extraction lines.

$r(cm)$	$z(m)$	label
-0.7	-0.7020	z_0
-0.6	-0.7124	z_1
-0.3	-0.7228	z_2
-0.1	-0.7335	z_3
0.001	–	–
0.1	–	–
0.2	–	–
0.5	–	–

Table 4.6: Radial and Vertical data probe locations. For a total of 32 probes.

4.4 Verification

Data from five simulations were extracted to conduct both this verification portion as well as the validation portion of the PHS presented in the next section. The data was extracted in the manner described section 4.3.5. Performing the validation of the PHS simulations was carried out using grid and time-step studies. From these simulations, the 32 points locations, listed in Table 4.6, are extracted from each simulation and compared. Figure 4.4 illustrates the locations of data points for a single extraction location with a representation of the comparison error, ϵ_h, for a given measurement, f_h. This illustration is represented using experimental data, however, the same procedure and locations are utilized when comparing simulations for the verification studies presented here.

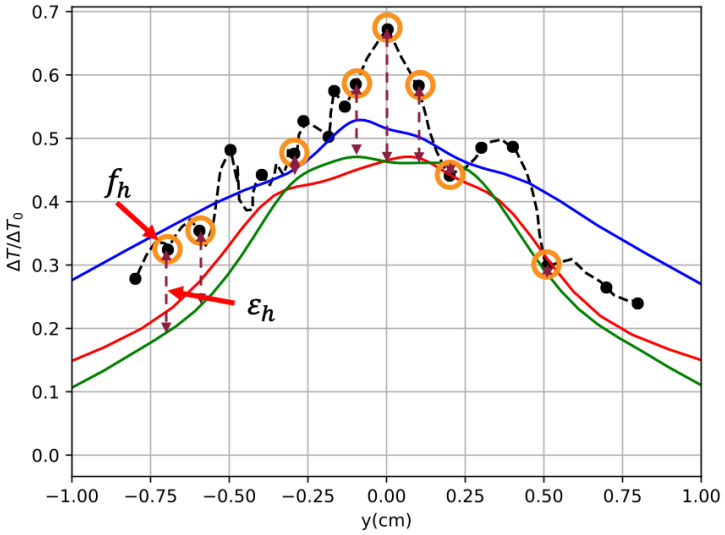

Figure 4.4: Overlay of data extraction locations, along with error approximation, onto data plotted for one of the extraction locations.

Information about the grids used for the grid study are presented in Table 4.3; note that the finest time step was used for all these simulations. For the time–step studies, the fine grid was used with varied time–steps, the list of time–steps, along with the approximated Courant number (Co) for each, are presented in Table 4.7.

Δt	Co
0.002	0.85
0.001414	0.60
0.001	0.42

Table 4.7: Tabulated Co for the various time–steps investigated. These were kept below 1.0 to ensure accurate time marching.

Post–processing the simulations involves calculating the error between the simulations. The formulation for the comparison error is shown in eq. (4.4). The subscript rh denotes the coarser mesh, or time–step, and the h subscript denotes the finer. Once the error at each point location along an extraction location z_i, the root mean square (RMS) value of the error is then calculated using eq. (4.5). Where N is the number of sample points along each extraction location. Figure 4.5 is a sample of the full set of figures, seen in Appendix B.2, where the calculated error is plotted for each data point at each extraction location.

$$\epsilon_{rh} = \frac{f_{rh} - f_h}{f_h} \tag{4.4}$$

$$RMS_{rh} = \left[\frac{1}{N}\sum_{i}^{N} \epsilon_{rh}\right]^{1/2} \tag{4.5}$$

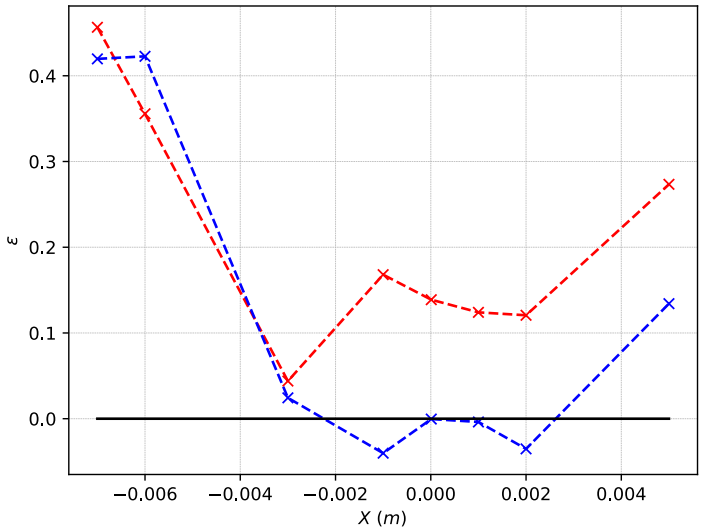

Figure 4.5: Verification error plotted for the grid study at the z_2 extraction location. : Coarse–Medium, : Medium–Fine grid comparison.

The tabulated values for the calculated RMS values are presented in Table 4.8. Analyzing the trends shown in the table, it is shown that with increasing refinement, both the grid and the time-step showed a decrease in calculated error for all extraction locations and studies. This trend held for all but one, the closest location to the source, z_0, for the time-step study.

Looking at the overall profiles in Figures 4.6 and 4.7 general agreement between the grids and time-steps utilized for this verification study can be shown. All extraction locations for both the grid and time-step studies are presented in Appendix B.1. The same statement found when analyzing the RMS values tabulated, is reiterated here with either grid or time-step refinement, where the overall profile marches towards a singular solution. A more rigorous verification campaign could be carried out to evaluate the numerical uncertainties and error quantities. However, this approach was not utilized for this verification study, and should be considered for future assessment.

	Grid Study		Time–step Study	
z	Coarse	Medium	0.002	0.001414
z_0	0.085	0.069	0.0053	0.0062
z_1	0.054	0.045	0.0105	0.0093
z_2	0.247	0.217	0.1180	0.0355
z_3	0.237	0.108	0.0767	0.0667

Table 4.8: Tabulated RMS values of the verification error at each extraction location, $z_0 - z_3$, for both the grid and time–step studies.

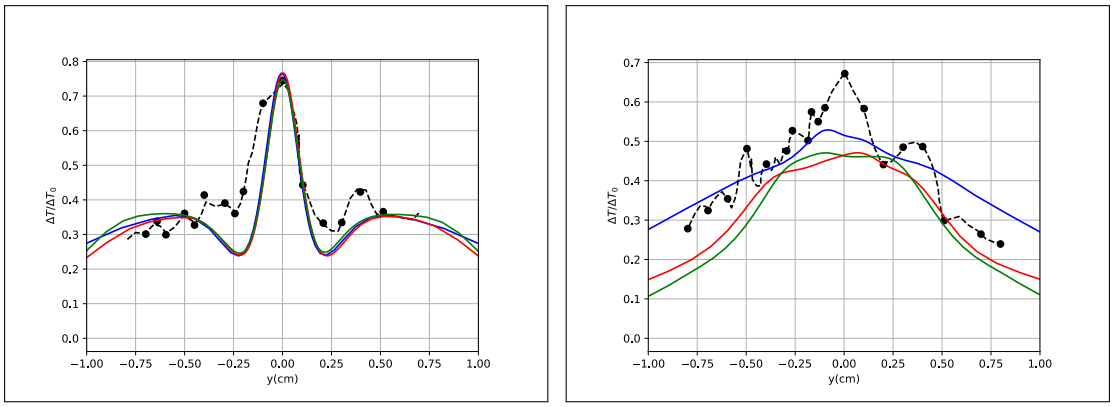

(a) (b)

Figure 4.6: Transverse temperature delta plots for the Grid Study : Coarse Mesh, : Medium Mesh, : Fine Mesh, : Experimental data. Plotting locations are (a) z_1 and (b) z_2.

4.5 Validation

The same procedure carried out for the verification studies were carried out for the validation studies. The only difference here being that one simulation is not compared to another, but rather to the experimental data presented by Tupitsyn and Chashechkin. The same simulation data from the verification studies are utilized for the comparison errors calculations. Again, Figure 4.3 is an illustration of the data points taken from each extraction locations. The same information for the grid and time–step studies are presented in Tables 4.3 and 4.7, respectively.

$$\epsilon_h = \frac{f_h - f_e}{f_e} \tag{4.6}$$

Post–processing the validation data is done just as the verification study. Figure 4.8 is a

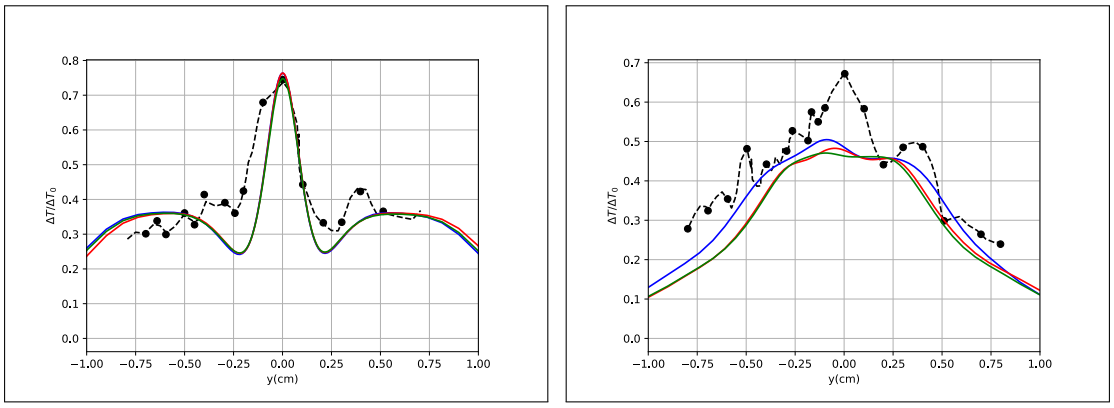

(a) (b)

Figure 4.7: Transverse temperature delta plots for the Time–Step Study : $\Delta t = 0.002$, : $\Delta t = 0.001414$, : $\Delta t = 0.001$, : Experimental data. Plotting locations are (a) z_1 and (b) z_2.

sample of the full set of figures, seen in Appendix B.3, plotting the comparison error for each data point at each extraction location. As mentioned in the verification section, the trends found from these figures are captured in the RMS values tabulated in Table 4.9.

Similar RMS values, to those seen in the verification studies, are calculated using eq. (4.5) and tabulated in Table 4.9. Since much of the simulations values only differ a small amount, it is not a surprise that each of the RMS values for any given extraction location, z_i, are similar in magnitude, for both the grid and time–step study. The trend of increasing refinement, however, does not result in the same conclusions made for the verification studies. No meaningful trends can be found for either the grid or time-step studies for any of the extraction locations.

	Grid Study			Time–step Study		
z	Coarse	Medium	Fine	0.002	0.001414	0.001
z_0	0.408	0.422	0.407	0.406	0.405	0.407
z_1	0.208	0.217	0.202	0.206	0.200	0.202
z_2	0.171	0.189	0.270	0.211	0.266	0.270
z_3	0.698	0.608	0.566	0.519	0.540	0.566

Table 4.9: Tabulated RMS values of the validation error at each extraction location, $z_0 - z_3$, for both the grid and time–step studies.

Again, a more rigorous approach to the validation of these simulation could be taken with numerical uncertainties and error estimates obtained. However, this approach, was not deemed appropriate for this study as no experimental uncertainty was presented by Tupitsyn and Chashechkin. It should also be noted that little information was given on how and when

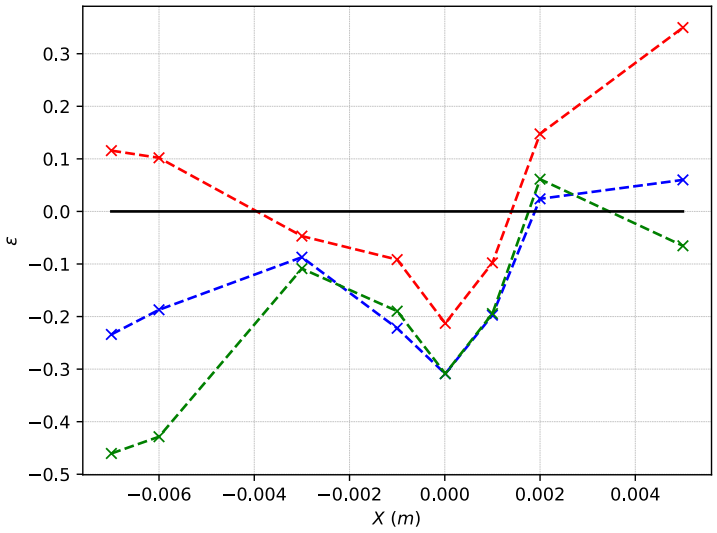

Figure 4.8: Validation error plotted for the grid study at the z_2 extraction location. : Coarse, : Medium, : Fine Grid.

the measurements were taken. With a general agreement to the experimental data and with little variation in the error estimates given for increasing refinement, the validation has proven to be adequate. From this, the simulations present the ability to emulate the PHS experiments outlined by Tupitsyn and Chashechkin, behaving in a predictable way that followed the experimental results. Upon finding a more rigorous experiment of a point source in a temperature or salinity stratified fluid, more validation assessments should be pursued.

Chapter 5

Jet–in–Crossflow

5.1 Problem Statement

The JICF problem is setup by embedding the jet orifice in a vertical flat plate, parallel to the $x - -z$ plane. Thus, by forcing the jet to exit perpendicular to the flat plate, the result is a horizontal pointing jet, in the positive y direction. This is also noted as being perpendicular to the gravitational vector. To study buoyancy affects, from both internal and environmental density differences, the jet is heated with a notional ΔT^* and the crossflow has a vertical temperature gradient. ΔT^* is the jet's non-dimensional temperature that, when implemented, is equal to one at its orifice. Salinity is held constant for these simulations and the density is calculated using the linear EOS, eq. (3.31). A boundary layer grows from the flat plate and directly interferes with the jet and its wake. The jet's orifice is much further downstream of the leading edge of the flat plate. However, to reduce computational costs from simulating such a large domain, a boundary layer profile is implemented as an inlet boundary condition. This will emulate the growth of the boundary layer in the region leading up to the jet's orifice.

5.2 CFD Simulation

In this section, the simulation setup for the JICF problem is outlined. To start with, the computational domain is discussed, followed by the boundary and initial conditions. A depiction of the simulation domain can be seen in Figure 5.1. Here the gray plane denotes the vertical wall, and, as previously mentioned, the leading edge of the flat plate is much further upstream of the orifice, in the negative x direction. All the simulations presented were ran for 2 pass-through times, with the pass-through time being $t_{PT} = \Delta X/U_0$, where ΔX is the distance from the jet orifice to the outlet plane, and U_0 is the free-stream flow velocity.

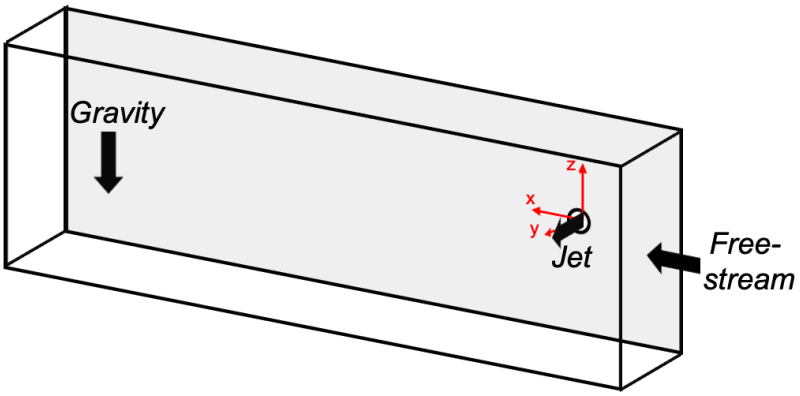

Figure 5.1: Depiction of the JICF problem setup.

5.2.1 The Computational Domain

The computational domain was generated by first creating the overall bounding measurements of the domain, relative to the jet orifice. To minimize the amount of influence the jet has on any boundary, a minimum distance of 10 jet diameters D_j was used for any boundary. To allow the inlet boundary layer ample time to grow and form inside the domain, this minimum distance is doubled, setting the inlet $20D_j$ upstream of the orifice, and thus setting the minimum x location. A desire to track the jet $100D_j$ downstream, determined the furthest x location. The origin is placed at the center of the jet's orifice.

Before creating a three–dimensional domain, the vertical plate was created. Starting by placing n_j number of points across the diameter of the jet's orifice and creating a "H–grid" inside the orifice. The mesh was then marched away from the jet with a plus-shape configuration. This topology localizes the higher skewness cells and allows for larger regions of zero skew cells to be generated elsewhere. The remainder of the two-dimensional plate mesh was generated using a growth rate of 1.15 and ensuring that any singular cell dimension did not exceed a specified value Δ_{MAX} that was set for each mesh and based on a portion of the jet diameter. This percentage differs for the various mesh resolution and can be seen in Table 5.4, along with other mesh metrics.

After the two–dimensional mesh was created, it was then extruded into the third dimension in a manner to generate a boundary layer mesh perpendicular to the wall. To ensure the boundary layer was adequately resolved, an initial wall spacing Δs was used and a set number of cells n_{BL} were placed within the inlet boundary layer thickness of approximately $1.2D_j$. This approximation was found using boundary layer theory for a flat plate. Due to the boundary layer growing downstream of the inlet, more cells will be within the boundary layer. Figure 5.2 depicts the mesh near the jet orifice, as well as the boundary layer for the fine and coarse meshes generated.

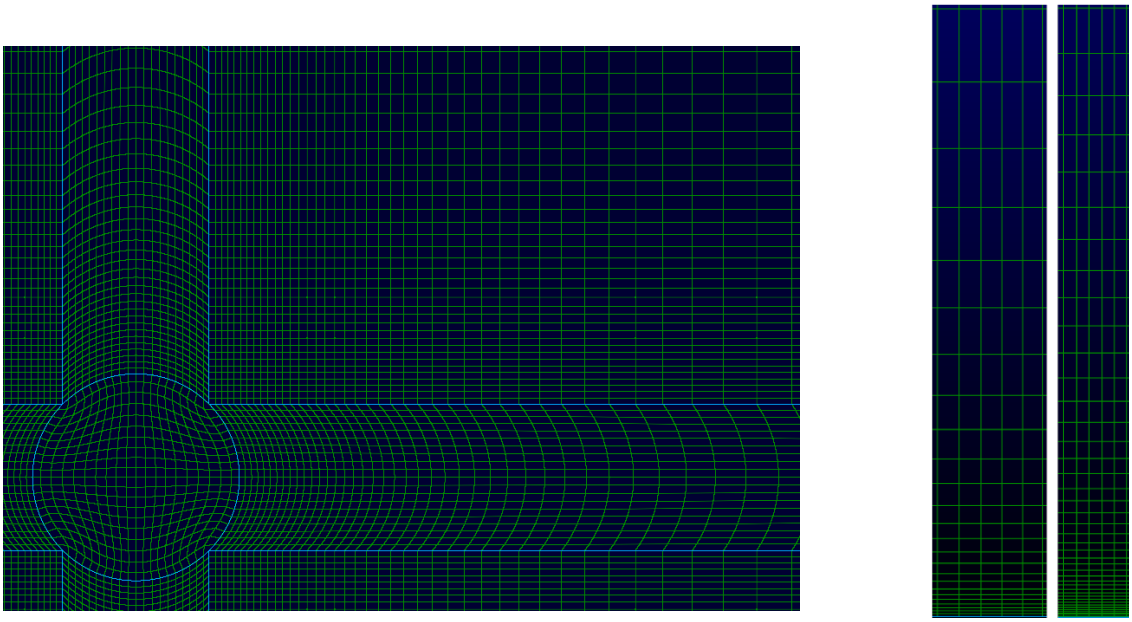

(a) Near the jet orifice

(b) Boundary layer

Figure 5.2: JICF mesh features. (a) coarse mesh, and (b) left – coarse mesh and right – fine mesh.

5.2.2 Boundary Conditions

Referring back to section 3.4, all four boundary types described are utilized in these simulations. First, a no–slip wall boundary is used for the vertical plate. Both the upstream, crossflow boundary and the jet orifice use the inlet boundary type. However, the upstream inlet utilizes a modified velocity inlet boundary condition, GroovyBC, instead of the standard fixedValue boundary condition. This allows for the implementation of the inlet boundary layer mentioned earlier. At the furthest downstream boundary, the outlet boundary type is specified as an outflow. The remaining boundaries, the maximum y boundary as well as the minimum and maximum z boundaries, utilize the far–field boundary condition. Figure 5.3 is an updated version of Figure 5.1 with the boundaries labeled with their appropriate boundary types. Table 5.1 outlines all the boundaries and their associated conditions.

5.2.3 Initial Conditions

To initialize the domain, both uniform and spatially varying conditions were used. Pressure, salinity, and the turbulence quantities utilized the uniform condition. Piezometric pressure was set to zero. Salinity was set to a reference value equal to that of the linear EOS's S_0. Assuming a free-stream turbulence intensity of 0.1% and setting the eddy viscosity ratio

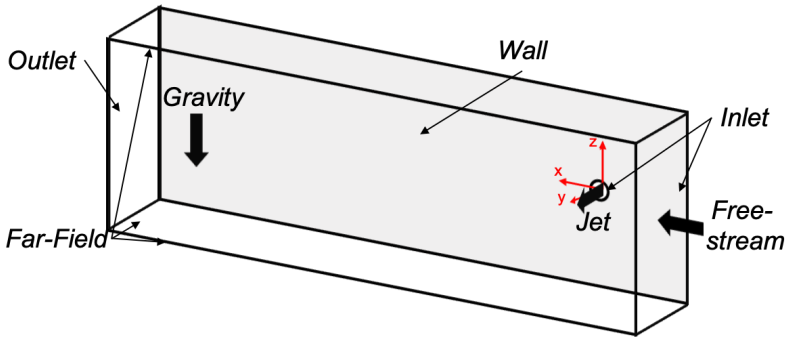

Figure 5.3: JICF domain with boundary types listed.

Field	Patch					Initial Conditions
-	Inlet	Jet	Outlet	Wall	Far-Field	-
U	$U_0(y/\delta_0)^{1/7}$	$(0, U_j, 0)$	$\nabla\phi = 0$	No-Slip	$\nabla\phi = 0$	$U_0(y/\delta_x)^{1/7}$
p	$\nabla\phi = 0$	$\nabla\phi = 0$	0	$\nabla\phi = 0$	$\nabla\phi = 0$	0
T	T_{BG}	$T_{BG} + \Delta T_j$	$\nabla\phi = 0$	$\nabla\phi = 0$	$\nabla\phi = 0$	$T_{BG} = T_0 + \frac{\partial T}{\partial z} z$
S	S_0	S_0	$\nabla\phi = 0$	$\nabla\phi = 0$	$\nabla\phi = 0$	S_0
k	k_0	k_0	$\nabla\phi = 0$	$WF(k_0)$	$\nabla\phi = 0$	k_0
ω	ω_0	ω_0	$\nabla\phi = 0$	$WF(\omega_0)$	$\nabla\phi = 0$	ω_0

Table 5.1: Table of boundary and initial conditions for the JICF simulations. The power law formulation of the inlet and initial velocity conditions is only applied within the boundary layer thickness, calculated using the axial locations Reynolds number.

ν_t/ν to 100, the turbulence quantities were determined. Both velocity and temperature were initialized with spatial variability, as discussed in section 3.5. The velocity is initialize using the $1/7^{th}$ power law and a free stream value of $U_0 = 2.0\ m/s$. This initialization was to reduce the computational effort of advecting the boundary layer downstream and is only meant as a crude initial guess to the entire velocity field. To setup the environmental stratification, the temperature was initialized in a linear fashion. See Table 5.1 for the formulation of both the velocity and temperature initial conditions.

5.2.4 High–Performance Computing

Similar to the PHS simulations, high computational costs long with a fair number of individual simulations, gives reason for the utilization of HPC machines. Table 5.2 shows each simulation with the number of cores utilized as well as the total computational cost in CPU hours. Again, comparing these computational times to those of an eight–core desktop machine, any one of these simulations would take over a week to complete. For the same

reasons as mentioned in 4.3.4, HPC machines are essential for running parametric studies such as the ones conducted in the following sections. The Air Force Research Laboratory's HPC cluster Mustang, was utilized for all the JICF computations shown here.

When comparing the computational costs for these simulations, the most drastic differences are found when varying velocity ratio. Increasing the jet's velocity ratio increased the computational cost by almost 75 percent, whereas decreasing the velocity ratio decreased the computational cost by over 50 percent. Removing the buoyancy from the jet (i.e., case 1) slightly decreased the computational effort. No trend emerges from the stratification study (cases 2, 5, and 6). With these differences being quite small, and understanding that no control over the specific hardware utilized for each simulation, no definite conclusions can be made from these computational times.

With a slightly larger eight percent difference, the RANS simulation is considered to be a more appreciable difference in computational costs. However, the idea of utilizing a more complex model resulting in less computational effort was not expected. For this reason, more studies should be conducted to assess the computational cost differences between the RANS and HRLES turbulence models. This should be done utilizing the same machine with the same simulations. Along with using the same hardware, more comparison cases should also be conducted and an average of the differences in the computational costs should be calculated.

Case	ΔT^*	r	Λ	Turb. Model	Cores	CPU Time (hrs)	Diff (%)
0	1	1.0	4.72	RANS	144	1,684	8
1	0	1.0	4.72	HRLES	144	1,503	−4
2	1	1.0	4.72	HRLES	144	1,558	–
3	1	0.5	4.72	HRLES	144	742	−52
4	1	2.0	4.72	HRLES	144	2,692	73
5	1	1.0	18.89	HRLES	144	1,580	1
6	1	1.0	94.43	HRLES	144	1,468	−6

Table 5.2: The number of processors utilized and the overall computational time, in hours, for the JICF simulations. Each case also has its accompanying parameters and the calculation of the difference in computational cost, when compared to the base HRLES case (case number 2), given as a percentage.

5.2.5 Data Extraction

For the comparisons presented in the following sections, cross–planes of velocity, U, temperature delta, ΔT and TKE are extracted for each of the various axial locations listed in Table 5.3. Within each of the cross planes, that are perpendicular to the cross flow (i.e., the axial direction), the boundary layer profile is extracted using the same vertical location

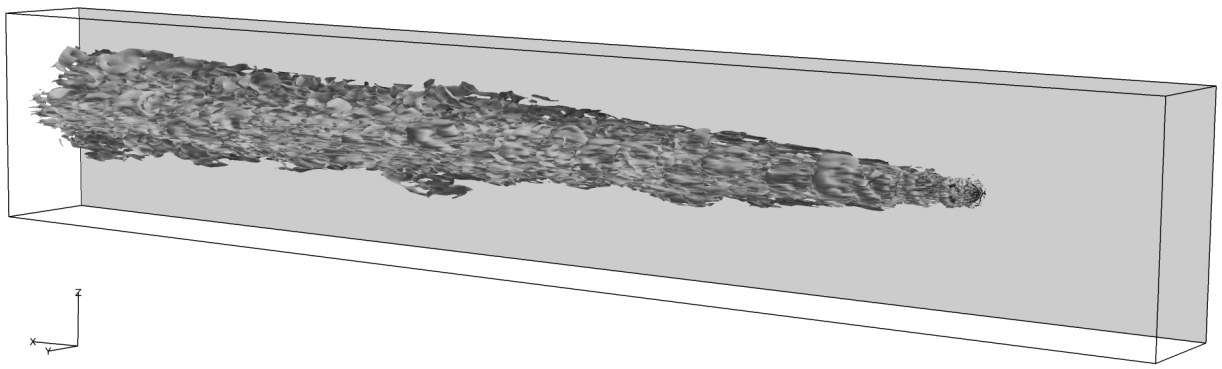

Figure 5.4: Depiction of the JICF problem.

as the jet center, allowing the boundary layer profiles to be compared for each simulation. Figure 5.4 shows a depiction of the JICF simulation and Figure 5.5 shows the same image with the extraction cross–planes visualized in black. These extractions were carried out using OpenFOAM's default *surface* post–processing utility and then plotted using a custom python script. This utility extracts the value of the requested variable from each cell center of the mesh and lists it, along with the extrapolation location, into a separate file with the format being specific to OpenFOAM. The forces and moments acting on the vertical plate were also calculated, with specifically the axial force, perpendicular force, and the moment about the vertical axis being directly compared.

X/D	5	10	20	50	100

Table 5.3: Table of data extraction locations for the JICF simulations. These include boundary layer profiles as well as cross-plane contours.

Another custom python script was written to extract the centerline location, height, and width of the wake for each simulation on each of the cross–planes previously extracted. These values were computed using a jet tracer that was introduced into the simulation as a passive scalar. For this scalar, the initial and boundary conditions are similar to the temperature and salinity scalars previously mentioned. The difference being that, initially, the concentration value was held to a value of zero. The inlet is given a constant value of one, for all times. For each cross–plane, the centerline is marked as the location of the maximum concentration for the given cross–plane. The wake height is measured as the distance between the maximum and minimum y locations (perpendicular to the plate) where the concentration value is one percent. The same measurement is used to calculate the wake width, however, instead using

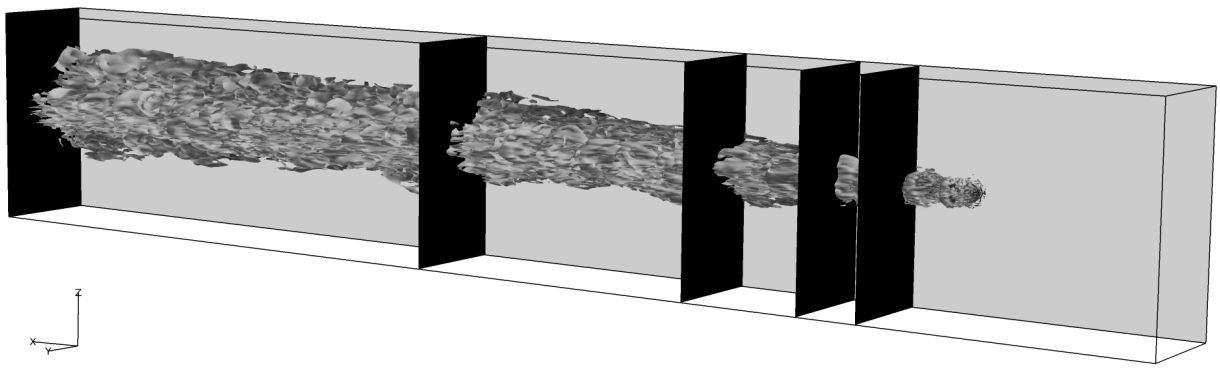

Figure 5.5: Depiction of the JICF problem with data extraction planes labeled.

the maximum and minimum z locations (parallel to the plate). Figure 5.6 depicts these measurements on a sample wake profile. Due to time averaging issues with the tracer scalar, these measurements were also conducted with the non–dimensional temperature delta.

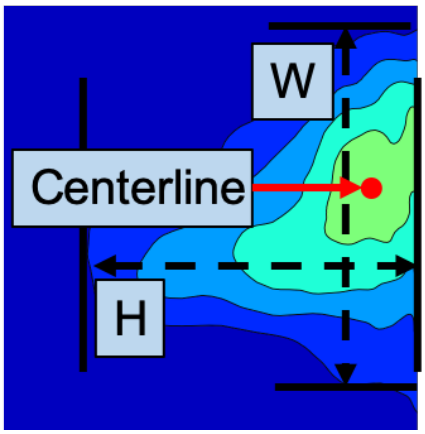

Figure 5.6: Depiction of the centerline, height (H), and width (W) of the JICF wake.

5.3 Grid Study

Before any simulations of interest are performed, a verification study is carried out. This will confirm that the mesh resolution is sufficient before proceeding. Here three grids, coarse, medium, and fine, are used to perform a JICF simulation, with each having the same initial and boundary conditions. These conditions are equivalent to those of Case 2 in Table 5.8

along with initial and boundary conditions in Table 5.1. The mesh properties for this family of grids are outlined in Table 5.4. A refinement factor of $\sqrt{2}$ was used to generate these grids and ensures that the boundary layer was resolved, a minimum of 20 cells were placed within the inlet boundary layer thickness, previously mentioned as $1.2D_j$.

Domain	Cells	n_j	n_{BL}	$\Delta s/D_j$	Δ_{MAX}/D_j
coarse	2.275×10^6	20	20	3.76×10^{-3}	0.5
medium	4.766×10^6	25	25	3.01×10^{-3}	0.4
fine	10.232×10^6	33	33	2.35×10^{-3}	0.3

Table 5.4: JICF computational domain metrics for comparison.

Comparing each grid is done by plotting the boundary layer profiles at the extraction locations mentioned in section 5.2.5. These plots can be seen in Appendix C. There, boundary layer profiles for the axial velocity, vertical velocity, temperature delta, and total turbulent kinetic energy are plotted for each of the meshes studied. From these images a few conclusions can be made. Looking at the axial velocity, the main noticeable difference is the over prediction of the velocity deficit on the coarse mesh close to the jet's orifice. Further downstream, this difference is eliminated, potentially due to the rise in the wake causing the center of the jet wake to no-longer coincide with the jet's initial vertical position. This rise can be seen when investigating the differences between the non–heated and heated imagery shown in the associated appendices, see section 5.5.1 for specific appendix sections. To further back this claim, a further grid study with an isothermal background environment is needed. Nevertheless, the medium and fine grids show excellent agreement amongst themselves. When comparing the vertical velocity, better agreement is seen closer to the jet's orifice. However this agreement begins to break down 10 diameters downstream. Again, the general trend is captured by the coarse mesh, but the magnitude of the peak and wall values slightly differ. Further downstream, both the location and magnitude of the peaks more drastically changes for the coarser simulation. Despite this the medium and fine grids show good agreement between each other.

Analyzing the temperature delta generated from the jet and its wake, better agreement between the coarse, medium, and fine grids are seen near the jet orifice (below $X/D = 10$). Continuing downstream, the coarse mesh's profile slightly widens while keeping the general shape and magnitude similar to the medium and fine grid solutions. The greatest difference between these meshes occurs at $X/D = 100$, where the magnitude of the coarse mesh is approximately double that of the fine mesh's profile. The total turbulent kinetic energy yields similar results that were discovered from the temperature delta profiles. To summarize, the coarse mesh was unable to capture the same profiles that the fine mesh simulation generated, which is to be expected. Despite this, the coarse mesh results were of the same shape and similar magnitude for the majority of the sampling locations. It is also noted that a converging solution is being reached with increasing refinement. Due to challenges of systematically refining boundary layer meshes, integral forces and moments were not used

as a comparison metric for this grid study.

5.4 Turbulence Model Comparison

Once the grids have shown sufficient convergence, the turbulence model comparison can be conducted before the parameter studies. Here, a comparison of a RANS and HRLES turbulence models are performed. For this section, the goal is to understand the differences between these models, and to be able to recognize the weaknesses and the strengths of each model. To conduct this comparison, the same simulation will be used for both the RANS and HRLES turbulence models tested, resulting in the only differences being the turbulence treatment. Refer to sections 3.2.3, 3.2.4, and 3.2.5 for a mathematical explanation of the RANS, LES, and HRLES equations, respectively.

Case	Heated	r	Strat.	Λ	Fr	Ri
RANS	yes	1.0	weak	4.72	200	0.014
HRLES	yes	1.0	weak	4.72	200	0.014

Table 5.5: Properties for HRLES and RANS cases used for comparisons.

With a basic understanding of how the aforementioned RANS and HRLES turbulence models work, their results can be compared, and conclusions made. To start off, Appendices D.1, D.2, and D.4 contain two- and three-dimensional imagery of the RANS and HRLES simulations of axial velocity and temperature delta. These images give a more holistic depiction of the growth and trajectory of the jet's wake as it impinges on the crossflow. Numerically, the forces and moments, calculated on the plate surface, are compared to those found when simulating a flat plate without the inclusion of the jet. Comparing the difference from the flat plate value allows for a simple baseline to be used as a comparison, and will make comparing the parameter variation results more intuitive. The axial and perpendicular forces, along with the moment about the vertical axis are numerically compared in Table 5.6.

Case	C_X	C_Y	C_M
No-Jet	9.054×10^{-4}	-5.435×10^{-3}	-1.631×10^{-3}
RANS	27.47	70.79	59.03
HRLES	9.44	70.30	59.49

Table 5.6: Force coefficients for a 'no–jet' calculation, and the deviation, in percent, $Diff(\%) = 100|C_D - C_{D,no--jet}|/C_{D,no--jet}$ from these values for the RANS and HRLES simulations. C_X: forcing parallel to plate, C_Y: forcing perpendicular to plate, and C_M: moment about z–axis, centered at jet orifice's center.

The most obvious difference between these models is that the RANS model predicts the drag to be 18 percent higher than when compared to the HRLES model. This can be attributed to the over prediction of the velocity deficit seen in Appendix D.3.1. Analyzing the axial velocity cross planes, seen in Appendix D.4.1, the over prediction of the deficit can be seen throughout all the downstream locations as well as the general structure and magnitude differences between these models. It is also seen that the width of the boundary layer grows slightly quicker with the RANS model, with a substantially greater increase in the magnitude. This affect is not only focused near the jet's wake, but also throughout the entirety of the domain. This would suggest that the RANS model over predicts the general boundary layer of the flat plate, when comparing to the HRLES model.

This over prediction was also carried over to the temperature delta boundary field. For the boundary layer profiles seen in Appendix D.3.1, however, the predictions given by the RANS and HRLES models more closely match each other near the jet's orifice, than when compared to further downstream locations. This being said, the RANS model still over predicts the maximum temperature delta value throughout each cross plane, seen in Appendix D.4.2. The centerline temperature delta values for each case are presented in Appendix D.3.2. Along with the centerline profile, wake growth is compared using the wake height and width, as well as the vertical and horizontal position of the measured jet centerline. These values are calculated using the procedure outline in section 5.2.5.

Comparing the width and height growth of the RANS and HRLES simulations reveals that the HRLES generates a much wider wake than the RANS model. The definition of the wake is defined by any temperature delta larger than one percent of the original jet delta. The general shape of the growth in height is shared between the RANS and HRLES models, however at approximately $X/D = 50$ the width of the HRLES wake is dampened by what is presumed to be the environmental stratification. The vertical rise of the centerline of the jet is also closely captured by the RANS model in the far-field, but over predicts the HRLES model in the near-field. The most drastic difference between the RANS and HRLES models for the wake growth and trajectory is the horizontal centerline. Recalling that the centerline is determined from the maximum temperature delta at each downstream location, it is apparent that the RANS model carries this maximum temperature delta further away from the plate and into the far-field as the wake progresses downstream. Beginning at $X/D = 10$, the RANS centerline's horizontal position behaves inversely to that predicted by the HRLES model. This produces an almost five times greater separation from the wall than when compared to the HRLES model.

Before comparing the TKE, the resolved portion is calculated, using eq. (5.1), in order to determine the total TKE. After which the resolved and modeled, provided via the turbulence model, TKE values can be combned. This TKE formulation is the one used throughout this section. With the full TKE calculated, boundary layer plots are given in Appendix D.3.1. Without this total formulation, the differences between these models would be drastically different due to the fact that RANS models all of the turbulent length scales, and HRLES only models length scales that fall below the local filter length. Comparing the total TKE

for each downstream location, it is apparent that the RANS model under predicts the TKE in both the magnitude and the overall breadth of its distribution. It is also noted that the RANS model does not capture the majority of the TKE generated within one diameter of the flat plate.

$$k_R = \frac{1}{2}\left(\overline{(u')^2} + \overline{(v')^2} + \overline{(w')^2}\right) \tag{5.1}$$

Another method of comparing these simulations is through the usage of integral quantities. Integral quantities allow for larger regions of simulations to be compared with a singular value, similar to point values. Examples of these are potential, mean kinetic, and turbulent kinetic energies; each of which are calculated using eq. (5.2), eq. (5.3), and eq. (5.4), respectively. Table 5.7 gives an average of the differences between the RANS and HRLES simulations for all extraction locations with integral values for $X/D = 100$, as a comparison example of the numerical values. As mentioned previously, the axial velocity, and the velocity in general, did not differ greatly between these simulations. This is confirmed by having less than a 5 percent difference between the integrated mean kinetic energy for the RANS and HRLES simulations. The RANS model's over estimation of the temperature delta can be confirmed by the approximated 70 percent difference between the integrated potential energy. Finally, a 30 percent decrease is noted when comparing the average integrated TKE. It is also seen that the RANS model has a decreased average integrated value, thus backing up the aforementioned statement that the RANS model produces less TKE than the HRLES simulations. For reference figure 5.7 compares both turbulence models temperature delta contours 100 diameters downstream of the jet orifice.

$$PE = \iint_A \frac{1}{2}\frac{g}{\partial\rho_{BG}/\partial z}(\rho - \rho_{BG})^2 \, dA \tag{5.2}$$

$$\overline{KE} = \iint_A \frac{1}{2}\rho|U|^2 \, dA \tag{5.3}$$

$$TKE = \iint_A \rho k_{total} \, dA \tag{5.4}$$

From these comparisons, it is recommended to utilize the HRLES turbulence modeling approach when simulating the buoyant JICF. The small difference in axial velocity could potentially be eradicated with longer run times and thus longer averaging, but further testing would be required before any claims can be made. However, this difference is less than 5 percent, when comparing the average integrated kinetic energy, and would not be the main reason for utilizing the HRLES model. Instead, the much larger difference between the temperature delta profiles and the potential energy, is a more appropriate justification for the usage of the HRLES turbulence model for this complex flow problem. With the RANS

Model	PE	KE	TKE
HRLES	124.7	81.5	64.9
	-	-	-
RANS	186.3	71.0	51.8
	69.0%	−4.23%	−31.9%

Table 5.7: Integrated energy values comparing RANS and HRLES turbulence models. Values taken from $X/D = 100$ plane, and percent difference is an average of the integrated energy quantity from all extraction locations.

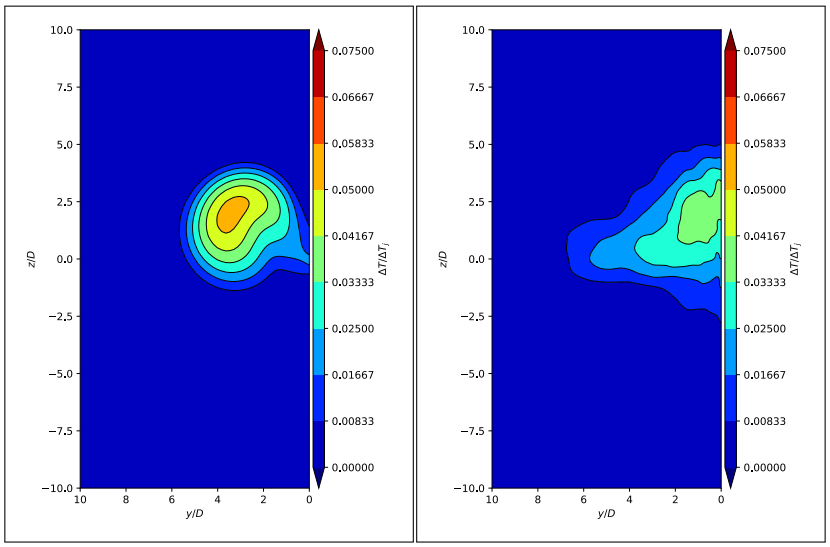

(a) RANS (b) HRLES

Figure 5.7: Comparison of the studied turbulence models cross plane contours of time averaged temperature delta at $X/D = 100$ downstream of the jet orifice.

model producing a temperature profile having a maximum value almost two percent higher than the HRLES model, an approximate 30 percent decrease in wake width, as well as an almost 20 percent decrease in the overall wake height, it is quite clear that a standard RANS modeling approach is not adequate for capturing and transporting the jet–crossflow wake, at least to 100 diameters downstream of the orifice and for higher Reynolds numbers.

5.5 Parametric Study

Once a verification study (i.e., grid–study) is completed and a reasoning for the usage of a HRLES turbulence modeling approach is presented, a parametric study can be performed. In this parametric study, buoyancy and momentum affects are accessed for a high Reynolds

number, low velocity ratio, buoyant jet in a stratified crossflow. The three parameters that are to be accessed and the reasoning behind their selection are discussed. For each of these parameters, the objective is to obtain a reasonable understanding of how the selected parameter and its associated value, impacts the fate and transport of the jet–crossflow interaction far downstream of their initial intersection. Initially the differences that applying thermal buoyancy (i.e., heat) to the jet has on the interactions between the jet and the crossflow is investigated. The jet temperature delta ΔT_j, which is defined as the difference from the environment, is non-dimensionalized by a reference temperature delta ΔT_0, resulting in a non-dimensional temperature $\Delta T^* = \Delta T_j / \Delta T_0$. This non–dimensional temperature is used to indicate whether the jet is thermally buoyant, $\Delta T^* = 1$ and thus heated, or not thermally buoyant with a ΔT^* value of 0, which is denoted as the non-heated simulations. This same reference temperature delta is used to non-dimensionalize all temperature delta values presented.

Another portion of this parametric study is to investigate the effects of varying the strength of the environmental stratification on the fate and transport of the thermal jet. In the simulations presented, the environmental stratification is due to a constant, vertical temperature gradient throughout the domain. The density can then be calculated from a linear EOS, described in section 3.2. The selection of the temperature gradients was initially selected to emulate that of an oceanic environment, and will be denoted as the 'weak' stratification profile. The non–dimensional parameter Λ is used to numerically quantify the stratification strength in a non-dimensional fashion. The expression for Λ is given in eq. (5.5). Not only is buoyancy important to investigate and understand the effects on the jet–crossflow interaction, but it was also desired to investigate the affects that variations in the velocity ratio has on the fate and transport of the JICF far downstream of the exit.

$$\Lambda = \frac{\partial T}{\partial z} \frac{D_j}{\Delta T_0} \times 10^4 \tag{5.5}$$

Table 5.8 lists the cases that encompasses this parameter study. The subsections below will compare a smaller subset of these simulations to investigate the individual parameters and their effects on the fate and transport of the jet's wake. Similar to the appendices formulated in section 5.4, Appendices E, F, and G house all the imagery for the heated, stratification, and velocity ratio parametric studies to be presented.

5.5.1 Heated

To begin understanding what parameters affect the fate and transport of a buoyant JICF, a baseline is first set. This is done using a non-buoyant JICF, known here as the non-heated jet. The only differences between the heated and non-heated simulations are the temperature delta of the jet as it exits the vertical plate. Referencing back to Table 5.8, the cases to be

Case	Heated	r	Strat.	Λ	Fr	Ri
1	no	1.0	weak	4.72	200	0.0
2	yes	1.0	weak	4.72	200	0.014
3	yes	0.5	weak	4.72	200	0.055
4	yes	2.0	weak	4.72	200	0.003
5	yes	1.0	medium	18.89	100	0.014
6	yes	1.0	strong	94.43	45	0.014

Table 5.8: Properties for the cases ran for the parametric study.

compared here are case 1, the non–heated jet, and case 2, the heated jet. The Richardson Number, Ri, has been calculated and is zero for the non–heated jet, and 0.014 for the heated jet. The numerical value of the Richardson number falling well below one indicates that the momentum of these jets were expected to dominate over the buoyancy affects and thus no noticeable difference should be discovered. Again, two– and three–dimensional imagery of the heated and non–heated simulations are presented in Appendices E.1, E.2, and E.4.

Plotted in Appendix E.3.1 are boundary layer profiles of axial velocity and temperature delta. As projected by the Richardson Numbers, little difference can be seen in the axial velocity, with the majority of the differences in the axial profiles being the magnitude of the velocity deficit being slightly larger for the non–heated jet case. Overall, the boundary layer profiles agree quite well between the heated and non–heated simulations. This determination is reinforced when analyzing the axial velocity cross–plane contours found in Appendix E.4.1.

The growth of the wakes is compared in Appendix E.3.2. For the non-heated simulation, the scalar tracer was used, in-lieu of the temperature delta, in order to determine the wakes height, width, and centerline position. From these images, the wake of both simulations grows in a similar fashion up until $X/D = 20$. Further downstream of this point, the vertical growth of each wake follows a similar trend, however the heated jet grows slightly faster leading to an approximate 15 percent increase in the wake width at 100 diameters downstream of the orifice. For the horizontal growth (i.e., away from the plate surface) the non–heated jet's wake height plateaus with minimal growth throughout the remaining 80 diameters downstream. The opposite is true for the heated jet, where after the 20 diameters mark, the heated jet's wake increases in height more rapidly after this location. This difference in trajectories leads to an over 30 percent difference in the height of the jet wakes. The centerline of the wakes, again, behaves similarly for the beginning 20 diameters. After which, the heated jet's vertical position drastically increases to a maximum of 1.8 diameters above the jet origin by 100 diameters downstream.

Similar to the turbulence model comparisons, both the force and moment coefficients are tabulated in Table 5.9 as well as the integrated energies and the average difference between the non-heated and the heat simulations, which are tabulated in Table 5.10. The idea that these simulations would differ little is further confirmed by analyzing the values inside these

tables, as the force and moment coefficients as well as the integrated energies do not differ more than a percent between these simulations. The difference being that the potential energy for the non-heated simulation is only generated by the background stratification and thus is four orders of magnitude smaller than that of the heated jet case. For this reason, the difference in the potential energy was not computed.

Heated	C_X	C_Y	C_M
-*	9.054×10^{-4}	-5.435×10^{-3}	-1.631×10^{-3}
yes	9.44	70.30	59.49
no	9.05	69.87	58.16

Table 5.9: Force coefficients for a 'no–jet' calculation*, and the deviation, in percent, $Diff(\%) = 100|C_D - C_{D,no--jet}|/C_{D,no--jet}$ from these values for the non-heated and heated jet cases. C_X: forcing parallel to plate, C_Y: forcing perpendicular to plate, and C_M: moment about z–axis, centered at jet orifice's center.

Heated	PE	KE	TKE
yes	124.7	81.5	64.9
	-	-	-
no	0.0	82.9	64.6
	–	0.02%	0.45%

Table 5.10: Integrated energy values comparing the non–heated and the heated jet cases. Values taken from $X/D = 100$ plane, while percent difference is an average of the integrated energy quantity from all extraction locations.

Investigating the differences in the fate and transport of a non-heated and a heated jet's wake downstream from its orifice has confirmed that, at least within 100 diameters of the orifice, no noticeable differences can be seen from the overall velocity and turbulence generated from the interaction of the jet with the crossflow. Despite these similarities in the velocity field, the heated jet's wake rose vertically approximately two diameters over the 100 diameter journey downstream. Due to this, the structure of the boundary layer on the plate was skewed, with a larger thickness above the centerline, and consequently a smaller thickness on the lower half. This skewness of the boundary layer thickness ultimately did not affect the overall drag of the plate, however. This comparison does not include the differences in temperature delta, as without the addition of heat inside the jet, no temperature delta can be generated at any location inside the wake.

This conclusion, however, does not mean that further downstream of the jet's orifice, the addition of buoyancy would not greatly impact the velocity and turbulence generated inside the jet, as well as the overall structure itself. To fully quantify the differences between the

heated and non–heated jet, simulations of the same manner should be replicated with an isothermal, isohailine background stratification. The lack of an environmental stratification would allow a fuller understanding of how heating affects the jet's trajectory. Similar determinations to the ones made here are expected to hold for this proposed study, however the magnitude of the differences is unknown.

5.5.2 Stratification

Buoyancy forcing from the jet itself is important to understand, but it is also of interest to study the effects that buoyancy forcing from the environment has on the jet-crossflow interaction. For this reason, the next parameter studied is the environmental stratification. To study this affect, the linear EOS was selected for its simplistic nature. It was also chosen to hold salinity constant throughout the domain. For the comparisons, three temperature gradients were selected and then used in identical simulations. Referencing Table 5.8, the cases to be compared in this section are case 2, also called the weak stratification, case 5, the medium stratification, and case 6, the strong stratification. These cases will be referenced by the weak/medium/strong notation not by their case number. The numerical value for Λ, which corresponds to the stratification level matching the respective case, will be used in the tables presented. The internal Froude number, Fr, is also included in this table.

Appendix F.3.1 houses the boundary layer profiles comparing the three stratification levels. As in the heated study, little variation in the axial velocity profiles is seen through any of the downstream locations. The temperature delta profiles follow this trend and little structural differences between the stratification levels can be seen at any downstream location. Further downstream, however, oscillatory behavior arises for locations closer to the plate, as the stratification strength increases. Despite this, the overall peak location and magnitudes are quite similar in all three cases. For both the weak and medium stratification strengths, the far–field value of the temperature delta increases to a non-zero value as the wake progresses downstream. The evolution of the temperature delta contours, shown in Appendix F.2.2, confirms this, as the contour maps presented in this figure are clipped to only show values with a value above the one percent non-dimensional temperature delta threshold.

Examining the wake's dimensions and centerline trajectory with the plots seen in Appendix F.3.2, little differences are again shown for the weak and medium stratification simulations. Slight differences do occur amongst these wakes, however nothing large enough to affect to the overall velocity and temperature delta profiles, seen in Appendix F.4. The strong stratification case, however, shows an approximate 20 percent decrease in the overall vertical width of the wake, when comparing to the weak stratification. The centerline of the strong stratification wake mimics that of the non-heated simulation previously discussed. Here the vertical position of the centerline is damped to almost a fifth that of the weak and medium stratification simulations.

Table 5.11 tabulates the force and moment coefficients, as previously discussed. For the

axial force coefficient, all three stratifications come within a percent of each other. For the perpendicular force and vertical moment coefficients, there is a maximum of six percent difference for all the cases. Comparing the energies yields similar results with a maximum of less than three percent difference between all three stratifications averaged integral values. Dissecting the cross–plane contours plotted in Appendix F.4, specifically the temperature delta contours of F.4.2, it is discovered that the strong stratification profile dampens the centerline value by about one percent of the jet's initial temperature delta at 100 diameters downstream of the orifice.

Λ	C_X	C_Y	C_M
4.72*	9.054×10^{-4}	-5.435×10^{-3}	-1.631×10^{-3}
4.72	9.44	70.30	59.49
18.89	9.84	67.22	53.97
94.43	9.68	70.29	59.94

Table 5.11: Force coefficients for a 'no–jet' calculation*, and the deviation, in percent, $Diff(\%) = 100|C_D - C_{D,no--jet}|/C_{D,no--jet}$ from these values for the different stratification strengths. C_X: forcing parallel to plate, C_Y: forcing perpendicular to plate, and C_M: moment about z–axis, centered at jet orifice's center.

Λ	PE	KE	TKE
4.72	124.7	81.5	64.9
	-	-	-
18.89	117.5	82.9	64.6
	1.6%	0.08%	1.11%
94.43	97.4	80.9	67.9
	0.29%	−0.78%	2.58%

Table 5.12: Integrated energy values comparing the different stratification strengths. Values taken from $X/D = 100$ plane, while percent difference is an average of the integrated energy quantity from all extraction locations.

Comparing the three stratification profiles presented here has shown that, at least within 100 diameters of the jet's orifice, no large differences are present when increasing stratification strength. The slightly decreased wake width of the strongest stratification profile was mentioned, along with a one percent decrease in the center temperature delta value proves that stratification does affect the wake's fate and transport, however, within the 100 diameters of this investigation, these comparisons have shown that stratification has little impact on the jet's wake and its interaction with the crossflow. As the wake traverses further downstream, stratification is expected to take a larger role than currently shown, however, results from these simulations cannot conclude any information beyond 100 diameters downstream of the

jet's orifice. From the comparisons presented, it was shown that the stronger stratification case begins to flatten out the temperature delta profile within 100 diameters of the jet's orifice. This affect was not present in the medium stratification simulation. For this reason, further studying would be required to determine at what strength does the stratification need to be, before the temperature wake begins to flatten within 100 diameters downstream.

5.5.3 Velocity Ratio

The final parameter to be tested is the velocity ratio of the jet. This value is the result of non–dimensionalizing the jet velocity by the free–stream velocity, U_0. The notional cases previously tested had a velocity ratio r equal to one, such that the jet's velocity matched that of the free stream. To test the affects this parameter has on the fate and transport of the jet's wake, the notional value was halved, and doubled, resulting in velocity ratios of $r = 0.5$ and $= 2.0$, respectively. Referencing Table 5.8, the cases to be compared are case 2, the notional, or base case with $r = 1.0$. The low velocity ratio case is number 3, with $r = 0.5$, and case 4 is the high velocity ratio case with $r = 2.0$. Comparing the Richardson Number for these cases, it can be seen that none of these cases should be dominated by buoyancy, but instead by momentum. It should also be noted that the momentum for each of these cases differs, but the jet temperature delta remained unchanged.

This parametric study produces the largest variation in three–dimensional imagery. The differences between these simulations are shown in Appendix G.1. Less structure is shown in the high r simulation than either the notional or low velocity ratio simulations. The streamlines on the wall here, as well as the boundary layer profiles shown in Appendix G.3.1 and the axial velocity contours in Appendix G.4.1, suggest that the reason for the decrease in structure for the high velocity ratio simulation would be attributed to the fact that the jet's wake blew through the plate's boundary layer and is, for the most part, separate from the boundary layer affects.

Analyzing the axial velocity boundary layers plotted in Appendix G.3.1, each velocity ratio has a unique profile close to the jet orifice. This uniqueness slowly fades further downstream. This fading however is potentially due to the wake center rising above the centerline and thus these plots further downstream do not capture the true center of the wake. It is noticeable, however, that the higher the velocity ratio value, the larger the overall boundary layer thickness is, as well as the strength of the velocity deficit within the profile. Near the jet orifice, the temperature delta profiles take a similar shape, despite having different peak values and locations. This similarity breaks down rather quickly as the lower velocity ratio case flattens its temperature delta profile, while the high velocity ratio case retains its original parabolic profile throughout the entirety of the 100 diameter stretch. The notional case attempts to blend these two scenarios resulting in a flattened parabolic shaped profile.

The temperature delta value along the centerline, for each of the velocity ratio simulations, has little variation. The low velocity ratio does produce a slightly lower centerline value by

$X/D = 100$, however. The wake height and width, shown in Appendix G.3.2, of the notional and high velocity ratio simulations follow similar trends with the high velocity ratio producing a wider and taller wake. These wakes have a width–to–height ratio of approximately one throughout the entirety of the downstream progression. The low velocity ratio simulation does not follow these trends, but instead has a width–to–height ratio of over two. The wake height of the low velocity ratio simulation plateaus after around 30 diameters downstream, whereas the height of the notional plateaus around 50 diameters. The height of the high velocity ratio wake continues to grow throughout the 100 diameter domain. The horizontal rise of the centerline for both the low velocity ratio and notional case remains within one and a half diameters of the plate. The vertical rise, however, remains within a single diameter for either case until 50 diameters, at which time the wake centerline grows to approximately two diameters above the jet's vertical center position. For the high velocity ratio simulation, the vertical position of the centerline remains within one diameter of the jet's center, but the horizontal position linearly grows further from the plate.

Looking specifically at the temperature delta profiles, for the notional, $r = 1.0$ case, the wake initially starts circular, quickly transitioning into an ovoid, and then to a triangular shape by $X/D = 50$. Initially the low velocity ratio case has a higher center temperature value. This higher center value slowly flips to a lower center value by $X/D = 20$, where it remains lower than the notional case for the remainder of the downstream locations. The overall shape of the low velocity ratio wake begins circular, like the notional case, but at $X/D = 10$ this profile changes into a triangular shape, and by the final downstream location, this shape has shifted into a semi–circular shaped wake. The high velocity ratio case more closely resembles the structure of a typical JICF simulation depicted in the literature. Producing a double lobed wake that folds into itself. However, by 20 diameters downstream, this wake structure is replaced with a circular wake which grows to a height of about nine diameters before reaching 100 diameters downstream. The maximum extent from the notional case was only around seven diameters and the low velocity ratio case just reached over three diameters at 100 diameters downstream. Figure 5.8 is a collection of the furthest downstream location's temperature delta cross–plane contours. From these images, it is clear the differences that velocity ratio has on the fate and transport of the wake as it traverses downstream of its orifice.

As presented in the studies before, the forces and moments on the plate are given in Table 5.13, with the integrated energies given in Table 5.14. For both the low and high velocity ratio cases, the axial force acting on the plate drastically increases with approximately a 20 percent increase for both cases. There is also an increase in the perpendicular forcing and the vertical moment coefficient, however the low velocity ratio case has a maximum increase of 28 percent, whereas the high velocity ratio case has a maximum increase of almost double that of the notional case with a 65 percent increase, over the flat plate calculation. The proposed reasoning for this larger increase in the coefficients for the high velocity ratio case is the wake being pushed further from the plate surface, resulting in the wake acting as a virtual appendage on the plate. Conversely is the increase of these coefficients for the low

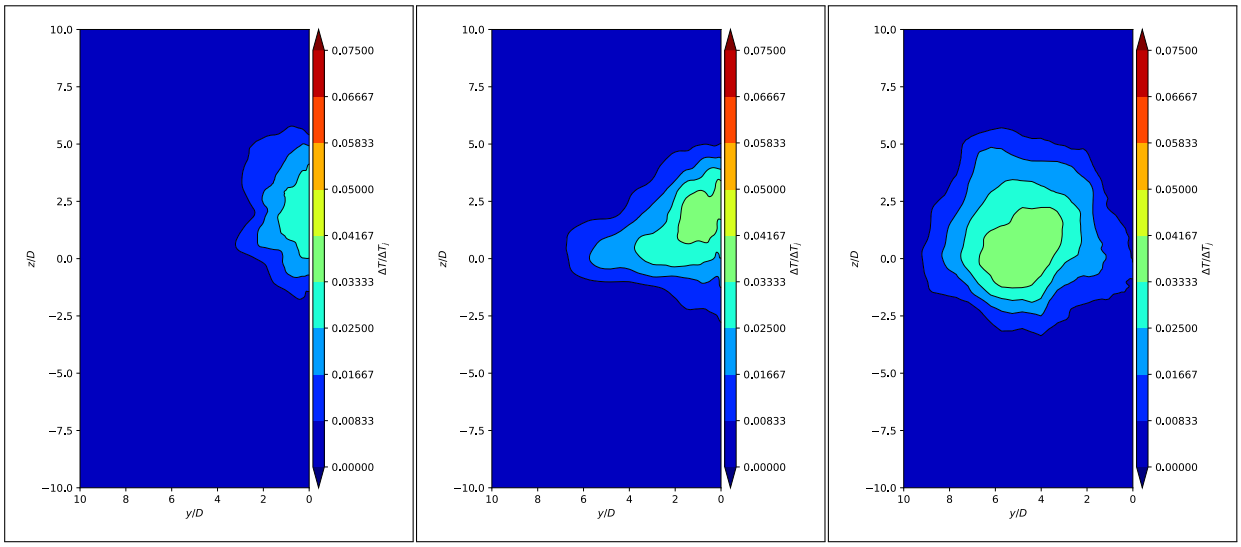

(a) Low Velocity Ratio (b) Base (c) High Velocity Ratio

Figure 5.8: Comparison of the studied velocity ratio cross plane contours of time averaged temperature delta at $X/D = 100$ downstream of the jet orifice.

velocity ratio case. Here the complete addition of the jet's wake into the boundary layer of the plate, resulting in a significantly wider wake that causes these coefficients to increase over the notional case. However, this increase is not as drastic as the high velocity ratio case due to the decrease momentum of the low velocity ratio case's jet, and resultant wake.

Breaking down the differences in the integrated energies for these simulations, it is understood that the high velocity ratio case drastically increased both the potential and turbulent kinetic energies by almost 200 percent, over the notional case. Heading in the opposite direct is the low velocity ratio case, where both these energies are decreased by over 20 percent compared to those given by the notional $r = 1.0$ case. For a holistic comparison with the notional case, the change in energy for the low velocity ratio case decreased the averaged overall integrated energies by about 10 percent, whereas the high velocity ratio case increased the integrated energies by over 130 percent.

Varying the velocity ratio of the jet to a halved and a doubled value has yielded in a much wider variation in evolution of the jet-crossflow interaction than either the heated or stratification studies prior. For these cases, either increasing or decreasing the velocity ratio results in an increase of the forces and moments seen by the plate the jet exits from. However, the low velocity ratio case shown here, proved to have a much lower overall impact on the environment than either the notional and the high velocity ratio case did. This is evident in the overall decrease of the temperature delta wake seen in Figure 5.8 as well as in the 10 percent decrease in the integrated energies. This overall decrease in the impact on the environment is likely due to the wake being entrained into the plate boundary layer, thus only amplifying its affects instead of generating its own separate affects. From this analysis,

r	C_X	C_Y	C_M
*	9.054×10^{-4}	-5.435×10^{-3}	-1.631×10^{-3}
1.0	9.44	70.30	59.49
0.5	29.76	85.39	88.06
2.0	27.15	135.43	115.13

Table 5.13: Force coefficients for a 'no–jet' calculation*, and the deviation, in percent, $Diff(\%) = 100|C_D - C_{D,no--jet}|/C_{D,no--jet}$ from these values for the different velocity ratios. C_X: forcing parallel to plate, C_Y: forcing perpendicular to plate, and C_M: moment about z–axis, centered at jet orifice's center.

r	PE	KE	TKE
1.0	124.7	81.5	64.9
	-	-	-
0.5	63.6	104.3	65.2
	-24.3%	20.9%	-26.0%
2.0	315.2	97.7	122.2
	194.4%	21.4%	193.0%

Table 5.14: Integrated energy values comparing the different velocity ratios. Values taken from $X/D = 100$ plane, while percent difference is an average of the integrated energy quantity from all extraction locations.

it is determined that containing the jet's wake into the boundary layer of the plate helps to reduce the impact the jet has on the overall forces and moments acting on the plate. This also increases the mixing of the temperature distribution inside the jet's wake, effectively decreasing the potential energy the jet's thermal wake introduces into the environment.

Chapter 6

Conclusions

6.1 Summary of Findings and Contributions

The work presented here was in an effort to better understand the effects of turbulence modeling on capturing the JICF far downstream of the jet's orifice. Along with determining the affects that different turbulence models have on the capturing of the JICF, the assessment of the overall temperature and velocity distributions was to be determined. Following this, a parametric study was conducted to determine the effects of internal and external buoyancy forcing as well as the effects of internal momentum on the fate and transport of the JICF far downstream of the jet's orifice. Before any of this could be done, the computational model used was validated to determine the ability of the computational model to capture the JICF far downstream.

To validate the computational model, an experiment utilizing a point heat source in a salinity stratified environment was replicated. Grid and time-step studies were performed and compared to the experimental results. The verification proved that with increasing grid and time-step refinement, the simulations were converging to a solution. The validation using this experiment provided general agreement with the experimental data. However, due to a lack of rigorous recalling of procedures and measurements, no appreciable certainty was found in the experimental data. Thus, no uncertainty or error estimations resulted from this campaign. A more rigorous V&V campaign would be required in order to obtain such quantities.

With general agreement with experimental results, the turbulence model comparisons were conducted. Surprisingly, no substantial difference in computational effort was seen when comparing the usage of the RANS model to the usage of the HRLES model. The resolution of the RANS simulation past 20 diameters, however, saw a substantial hindrance when using the RANS model. Simulating the JICF using a RANS modeling provided a largely over predicted solution. An 18 percent increase in the axial forces was found, with an almost 70 percent increase in the averaged potential energy. The lack of entrainment of the jet's wake into the plate boundary layer, seen by the RANS model, provides a much lower turbulent mixing and thus a much larger increase in the mean potential energy produced. The maximum temperature delta was also over predicted throughout the entirety of the simulation domain. The RANS model did, however, under predict the wake height and width, however this could be attributed to the lower turbulent mixing and spreading of the

temperature profile.

Studying the internal buoyancy forcing of the jet was inconclusive. Likely due to the overpowering momentum forcing of this problem making it indiscernible if the buoyancy forcing see in the heated jet is solely due to the thermal buoyancy within the jet, or in part due to the external buoyancy of the environmental stratification. Nevertheless, the notable difference adding heat to the JICF problem caused, was an approximate two diameter rise in the centerline of the wake, as well as the rest of the wake. Varying the external buoyancy forcing was also inconclusive when comparing the weak and medium stratification profiles. However, when introducing the strong stratification, wake collapse began to occur. This is seen by the reduced wake width and height of the strong stratification simulation downstream of the orifice. The damping of the vertical rise of the centerline and the oscillatory behavior of the horizontal centerline rise also point to this conclusion. Other than these minor differences, the overall profiles and distributions of temperature and velocity remain similar between the weak, medium, and strong stratification strengths compared.

Varying the velocity ratio, and thus the internal momentum of the jet, was by far the most conclusive of the parameter studies conducted. It was shown that for lower velocity ratios, the jet's wake is entrained in the boundary layer of the plate the jet exits from. This causes an increase in turbulent mixing and thus produces a more distributed temperature profile 100 diameters downstream of the jet's orifice. This affect in turn reduced the overall mean potential energy produced by the jet and crossflow interaction. This was confirmed by the low velocity ratio decreasing the mean potential energy by over 20 percent and then high velocity ratio simulation increasing the mean potential energy by almost 200 percent, when compared to the notional case. Along with a deviation for the mean potential energy produced, both the low and high velocity ratio simulations increased the forces seen by the plate by over 15 percent, for the axial forcing.

6.2 Recommended Future Studies

From the conclusions on the behavior of RANS models in comparison with HRLES turbulence models, the recommendation is to utilize the HRLES technique when carrying the wake of a JICF simulation further than 20 diameters downstream of the jet orifice. This will ensure that adequate resolution of the JICF is carried far enough downstream to accurately predict temperature and velocity profiles of the JICF. However, further understanding of all the various turbulence modeling techniques is the next step to ensure that proper capturing of the JICF wake occurs far downstream. As mentioned earlier, the investigation of the heated jet was inconclusive due to the inability to separate the internal and external buoyancy forcing in the simulations presented here. For this reason, and to understand how turbulence modeling techniques affects the thermal transport far downstream of the jet, it is suggested that the expanded turbulence modeling study should include heated and non-heated jets in an isothermal, isohaline stratification environment. This will provide further information

into how and if the turbulence treatment is affected by thermal jets.

Furthermore, investigating lower velocity ratios is another suggested avenue to study. Studying these could shed light on controlling the entrainment of the jet's wake into the plate boundary layer. Understanding this will potentially allow the tuning of turbulence mixing inside the jet's wake and the plate's boundary layer with the possibility of controlling the reduction of the mean potential energy released into the surrounding environment. Potentially the most important work that needs to be done for the high Reynolds number, low velocity ratio JICF problem are experimental campaigns at both full and model scales. These experiments would stand as validation cases for simulations and techniques such as the ones presented here. A greater understanding of the fate and transport of the JICF problems studied here, as well as the ability of computational models to predict these flows can only come from such experiments.

Bibliography

[1] H. Acker. Stack design to avoid smoke nuisance. In *New England Section of The Society of Naval Architects and Marine Engineers*, 1951.

[2] Ya.D. Afanas'ev and S.I. Voropaev. Horizontal submerged jet in a stratified fluid. *Fluid Dynamics*, 28(6):757 – 62, 1993/11/. ISSN 0015-4628. URL http://dx.doi.org/10.1007/BF01049775.

[3] *LES/RANS Modeling of Turbulent Mixing in a Jet in Crossflow at Low Velocity Ratios*, San Diego, CA, January 2016. AIAA.

[4] *Adaptive Detached Eddy Simulations of Jet in Cross Flow*, January 2017. AIAA.

[5] Gary A. Briggs. Diffusion estimation for small emissions. Technical report, Air Resources Atmospheric Turbulence and Diffusion Laboratory, NOAA, Oak Ridge, TN, May 1973.

[6] E. Buckingham. On Physically Similar Systems; Illustrations of the Use of Dimensional Equations. *Physics Review*, 4(4):345–376, 1914.

[7] Dalibor Cavar and Knud Erik Meyer. Les of turbulent jet in cross-flow: Part 1 - a numerical validation study. *International Journal of Heat and Fluid Flow*, 36:18–34, 2012.

[8] Y. R. Chang and K. S. Chen. Prediction of opposing turbulent line jets discharged laterally into confined crossflow. *International Journal of Heat Mass Transfer*, 38(9): 1693–1703, 1995.

[9] Fanghui Chen and Poojitha D. Yapa. Modeling gas separation from a bent deepwater oil and gas jet/plume. *Journal of Marine Systems*, 45:189–203, 2004.

[10] Vincent H. Chu. Turbulent dense plumes in a laminar cross flow. *Journal of Hydraulic Research*, 13(3):263–279, 1975.

[11] Daniele Contini and Alan Robins. Experiments on the rise and mixing in neutral crossflow of plumes from two identical sources for different wind directions. *Atmospheric Environment*, 38:3573–3583, 2004.

[12] R. B. Darden. Jet-induced flow in a stratified reservoir. pages 118p –, 1973/10/.

[13] Lynyrd de Wit, Cees van Rhee, and Geert Keetels. Turbulent interaction of a buoyant jet with cross-flow. *Journal of Hydraulic Engineering*, 140(12), 2014.

[14] J.-M. Most F. Roger, A. Gourara and H.Y. Wang. Numerical investigation o the reactive gas mixing throught interaction between twin square jets side-by-side and a crossflow. *Chemical Engineering Journal*, 238:45–55, 2014.

[15] Loh-Nein Fan. *Turbulent Buoyant Jets into Stratified or Flowing Ambient Fluids*. PhD thesis, Division of Engineering and Applied Science, California Institute of Technology, Pasadena, California, June 1967.

[16] V. Garg and R. Gaugler. Effect of coolant temperature and mass flow on film cooling of turbine blades. *Int. Journal of Heat Mass Transfer*, 40(2):435–445, 1997.

[17] Robert L. Gordier. Studies of fluid jets discharging normally into moving liquid. Series B 28, St. Anthony Falls Hydraulic Laboratory, Univeristy of Minnesota, 1959.

[18] ESI Group. Openfoam-v1806, 2018. URL https://openfoam.com.

[19] B. Gschaider. swak4foam, 2010. URL https://openfoamwiki.net/index.php/Contrib/swak4Foam.

[20] D. P. Hoult, S. R. O'Dea, G. L. Touchton, and R. J. Ketterer. Turbulent plume in a turbulent cross flow: Comparison of wind tunnel tests with field observations. *Journal of the Air Pollution Control Association*, pages 56–60, 1977.

[21] Robert R. Hwang and T. P. Chiang. Buoyant jets in a crossflow of stably stratified fluid. *Atmospheric Environment*, 20(10):1887–1890, 1986.

[22] Robert R. Hwang, Yin-Fan Pon, and Wen-Chang Yang. Multiple-port bouyant jets in density stratified cross flow. *Journal of the Chinese Institute of Engineers*, 13(5): 543–553, 1990.

[23] Project Management Institute Project Management Institute. Ieee draft guide: Adoption of the project management institute (pmi) standard: A guide to the project management body of knowledge (pmbok guide)-2008 (4th edition). *IEEE P1490/D1, May 2011*, pages 27–36, June 2011. doi: 10.1109/IEEESTD.2011.5937011.

[24] R. I. Issa. Solution of the implicitly discretised fluid flow equations by operator-splitting. *Journal of Computational Physics*, 62:40–65, January 1986. doi: 10.1016/0021-9991(86)90099-9.

[25] G.S. Janowitz. On wakes in stratified fluids. *Journal of Fluid Mechanics*, 33 (3):417 – 32, 2 Sept. 1968. ISSN 0022-1120. URL http://dx.doi.org/10.1017/S0022112068001412.

[26] Yasuhiro Kamotani and Isaac Gerber. Experiments on a turbulent jet in a cross flow. *AIAA*, 10(11):1425–1429, November 1972.

[27] J. F. Keffer and W. D. Baines. The round turbulent jet in a cross-wind. *Journal of Fluid Mechanics*, 15:481–496, 1963.

[28] J.F. Kennedy and R.A. Froebel. Two-dimensional turbulent wakes in density-stratified liquids. pages 8 –, New York, NY, United States, 1964.

[29] P. R. Kulkarni, S. N. Singh, and V. Seshadri. Behaviour of ship funnel exhaust in the wake of a bluff body. *Marine CFD*, 2005.

[30] P. R. Kulkarni, S. N. Singh, and V. Seshadri. Parametric studies of exhaust smoke-superstructure interaction on a naval ship using cfd. *Computers and Fluids*, 36:794–816, 2007.

[31] J. W. Lavelle. Buoyancy-driven plumes in rotating, stratified cross flows: Plume dependence on rotation, turbulent mixing, and cross-flow strength. *Journal of Geophysical Research*, 102(C2):3405–3420, February 1997.

[32] Y. Hu Z. Lu Haibo Jiang M. Zhou, Hao Jiang and C. Li. Analyzing of mixing performace determination factors fro the structure of radial multiple jets-in-crossflow. *Chinese Journal of Chemical Engineering*, 2019.

[33] B. R. Morton. On a momentum-mass flux diagram for turbulent jets, plumes and wakes. *Journal of Fluid Mechanics*, 10:101–112, 1961.

[34] B. R. Morton and A. Ibbetson. Jets deflected in a crossflow. *Experimental Thermal and Fluid Science*, 12:112–133, 1996.

[35] B.R. Morton. Entrainment models for laminar jets, plumes, and wakes. *Physics of Fluids*, 10(10):2120 – 2127, 1967. URL http://dx.doi.org/10.1063/1.1762007.

[36] C.S. Konig M.R. Mokhtarzadeh-Dehghan and A.G. Robins. Numerical study of single and two interacting turbulent plumes in atmospheric cross flow. *Atmospheric Environment*, 40:3909–3923, 2006.

[37] S. Muppidi and K. Mahesh. Direct numerical simulation of round turbulent jets in crossflow. *Journal of Fluid Mechanics*, 574.

[38] T. H. New, T. T. Lim, and S. C. Luo. Elliptic jets in cross-flow. *Journal of Fluid Mechanics*, 494:119–140, 2003.

[39] T. H. New, T. T. Lim, and S. C. Luo. A flow field study of an elliptic jet in cross flow using dpiv technique. *Experiments in Fluids*, 36:604–618, 2004.

[40] T. H. New, T. T. Lim, and S. C. Luo. Effects of jet velocity profiles on a round jet in cross-flow. *Experiments in Fluids*, 40:859–875, 2006.

[41] Joongcheol Paik. Numerical simulation of thermal discharges in crossflow. *IEEE*, pages 328–332, 2011.

[42] R. Peyret. Unsteady evolution of a horizontal jet in a stratified fluid. *Journal of Fluid Mechanics*, 78(1):49 – 63, 1976/11/05. ISSN 0022-1120. URL http://dx.doi.org/10.1017/S0022112076002322.

[43] C. H. B. Priestley. A working theory of the bent-over plume of hot gas. *Quarterly Journal of the Royal Meteorological Society*, pages 165–176, 1956.

[44] F.S. Sarikurt and Y.A. Hassan. Large eddy simulations of erosion of a stratified layer by a buoyant jet. *International Journal of Heat and Mass Transfer*, 112:354 – 65, Sept. 2017. ISSN 0017-9310. URL http://dx.doi.org/10.1016/j.ijheatmasstransfer.2017.04.134.

[45] K. Shahzad, B. A. Fleck, and D. J. Wilson. Small scale modeling of vertical surface jets in cross-flow: Reynolds number and downwash effects. *Journal of Fluids Engineering*, 129:311–318, March 2007.

[46] P. J. Stockhausen, C. B. Clark, and J. F. Kennedy. Three-dimensional momentumless wakes in density-stratified liquids. pages 112p –, 1966/06/.

[47] R. I. Sykes, W. S. Lewellen, and S. F. Parker. On the vorticity dynamics of a turbulent jet in a crossflow. *Journal of Fluid Mechanics*, 168:393–413, 1986.

[48] V. S. Tupitsyn and Yu. D. Chashechkin. Free convection above a point source of heat in a stratified fluid. article 2, The Academy of Sciences of the USSR, 1981.

[49] W. P. M. van de Watering. The growth of a turbulent wake in a density-stratified fluid. pages 56p –, 1966/11/.

[50] J. Wu. Collapse of turbulent wakes in densitystratified media. pages 2p –, 1965/01/.

[51] Duo Xu and Jun Chen. Experimental study of stratified jet by simultaneous measurements of velocity and density fields. *Experiments in Fluids*, 53(1):145 – 62, 2012/07/. ISSN 0723-4864. URL http://dx.doi.org/10.1007/s00348-012-1275-7.

[52] PAO YH. Laminar flow of stably stratified fluid past flat plate. *Journal of Fluid Mechanics*, 34(pt 4):795 – 808, 1968. ISSN 00221120.

Appendices

Appendix A

Point Source Generation

The Buckingham Π theorem generally states that a system with n variables, has $p = n - m$ number of dimensionless constants that can be derived. Where m is the number of overall dimensions the system entails [6]. Before applying this analysis to the point source generation, the variables of interest need to be determined. These variables will eventually formulate the equation for the point source to be implemented. The dimensional units of the source term are also required. The latter of these two will be tackled first due to its simplistic nature. To start, the scalar tranport equation on which the source term is to be applied is investigated. This is eq. (3.3) and rewritten here for ease of reference.

$$\frac{\partial \Phi}{\partial t} + \frac{\partial U_j \Phi}{\partial x_j} = k_\Phi \frac{\partial^2 \Phi}{\partial x_j \partial x_j} + \frac{\partial}{\partial x_j} \overline{u_j' \phi'} + S_\Phi$$

Again, Φ is the scalar and S_Φ is the source term to be determined. For the definition of the source term to hold, the dimensions of both the source term S_Φ and the temporal derivative must match. Since the dimensions of the temporal derivative has base dimensions of θ/T, where θ is the scalar's dimension and T is the base temporal dimension, the source term must also have those dimensions. For the problem of a thermal source, these would equate to temperature (Kelvin or Celcius) for θ and time (seconds) for T. The second of the two earlier mentioned requirements must now be addressed. For this the desired variables that will formulate the source term are sought. To start with, the volume V over which the source is applied and the density ρ of the fluid to which the source is applied, are required. Being that this source term is a thermal source, another variable that is desired as an input, is the power P applied to the source. Since heat is applied to a fluid, the specific heat of the fluid C_h is also required. Table A.1 outlines the basic variables just mentioned, and their respective base units.

Variable	S_ϕ	V	P	C_h	ρ
Units	θ/T	L^3	ML^2/T^3	$L^2/T^2\theta$	M/L^3

Table A.1: Base units for variables used in Buckingham Pi analysis.

With the determination of the necessary variables, and their base units, the number of dimensionless parameters can be determined by $p = n - m$. Recalling that n is the number

of variables and that m is the number of base units these variables contain, the following is found: $n = 5$ and $m = 4$. This ultimately leads to $p = n - m = 1$ and thus only a single dimensionless parameter is expected to come from this analysis. With the setup complete, the determination of the formulation of the source term can begin with the following expression.

$$(S_\Phi)(C_h)^a(P)^b(\rho)^c(V)^d = (1)$$

Subsituting the base dimenions, found in Table A.1, for each variable to obtain the following form.

$$\left(\frac{\theta}{T}\right)\left(\frac{L^2}{T^2\theta}\right)^a\left(\frac{ML^2}{T^3}\right)^b\left(\frac{M}{L^3}\right)^c\left(L^3\right)^d = (\theta)^0(M)^0(L)^0(T)^0$$

With this formulation, the exponents $a - d$ can be solved for by setting the exponents for each base dimension equal to each other. Firstly a can be solved for using the following expression:

$$\begin{gathered}\theta: \ 1 + -a + 0 + 0 + 0 = 0 \\ a = 1\end{gathered}$$

Following this same approach and substituting the value found for a, the exponents $b - d$ can be determined as follows:

$$\begin{gathered}T: \ -1 + \overset{1}{\cancel{-2a}} + -3b + 0 + 0 = 0 \\ b = -1\end{gathered}$$

$$\begin{gathered}M: \ 0 + 0 + \overset{-1}{\cancel{b}} + c + 0 = 0 \\ c = 1\end{gathered}$$

$$\begin{gathered}L: \ 0 + \overset{1}{\cancel{2a}} + \overset{-1}{\cancel{2b}} + \overset{1}{\cancel{-3c}} + 3d = 0 \\ d = 1\end{gathered}$$

Substituting the newly found exponents into the origial expression, the following form can be found for the expression of the source term.

$$\left(\frac{\theta}{T}\right)\left(\frac{T^2\theta}{L^2}\right)\left(\frac{ML^2}{T^3}\right)\left(\frac{M}{L^3}\right)\left(L^3\right) = (S_\Phi)(C_h)(P)^{-1}(\rho)(V)$$

Rearranging to aquire the final form of the source term as follows:

$$S_\Phi = \frac{P}{C_h \rho V}$$

Appendix B

PHS Data Plots

B.1 2D Plots

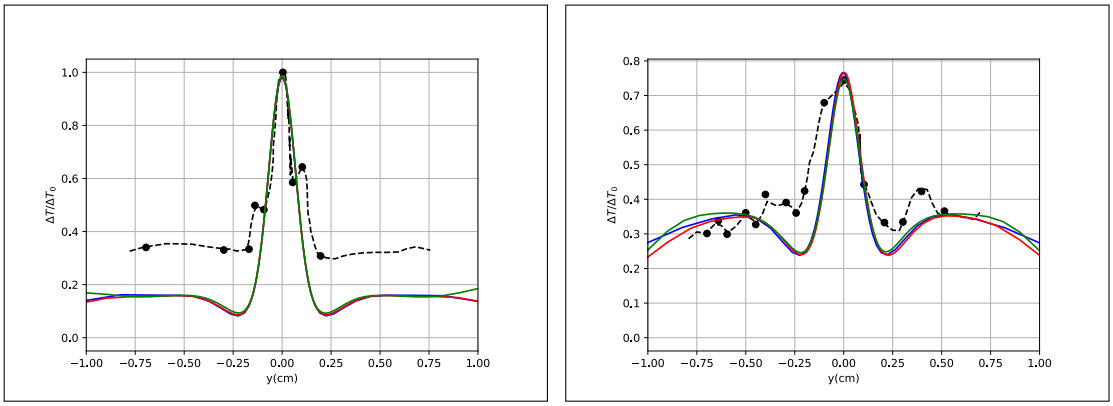

(a)

(b)

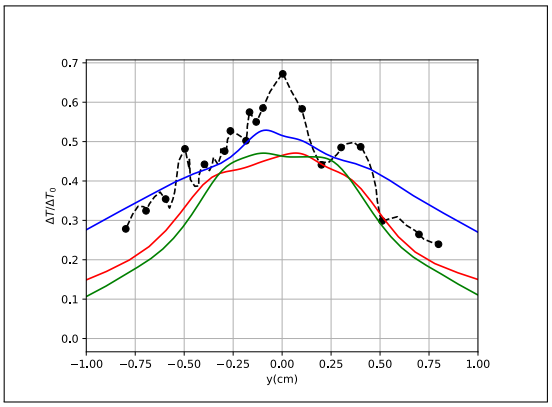

(c)

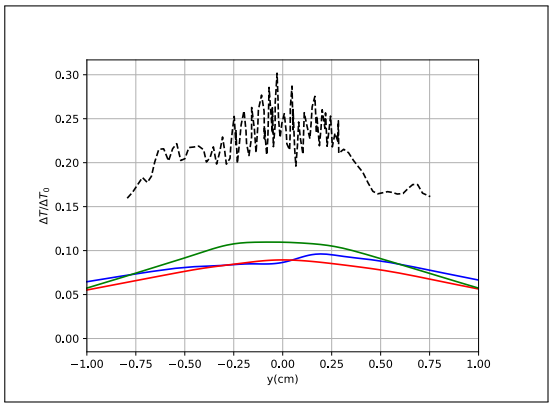

(d)

Figure B.1: Transverse temperature delta plots for the Grid Study. : Coarse Mesh, : Medium Mesh, : Fine Mesh, : Experimental data. Plotting locations are (a)-(d) z_0, z_1, z_2, and z_3, respectively.

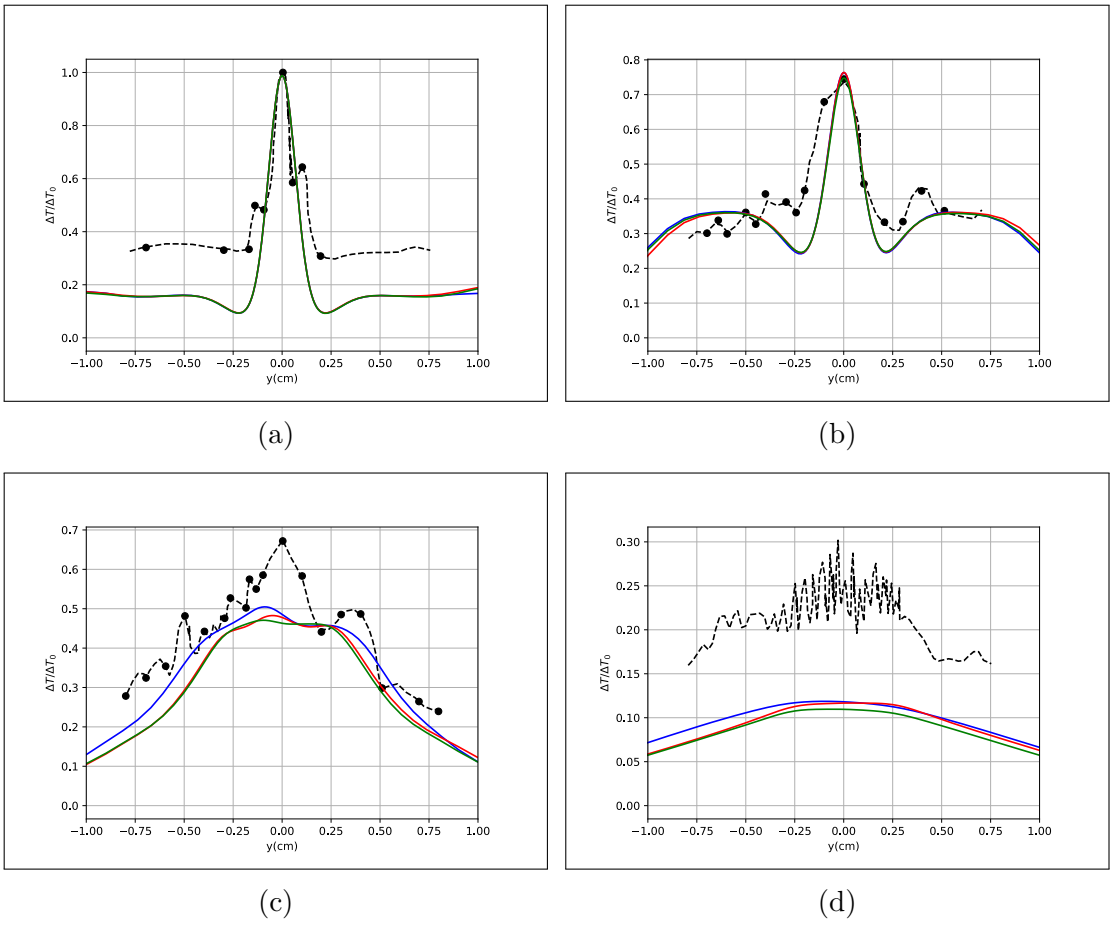

Figure B.2: Transverse temperature delta plots for the Time-Step Study. : $\Delta t = 0.002$, : $\Delta t = 0.001414$, : $\Delta t = 0.001$, : Experimental data. Plotting locations are (a)-(d) z_0, z_1, z_2, and z_3, respectively.

B.2 Verification

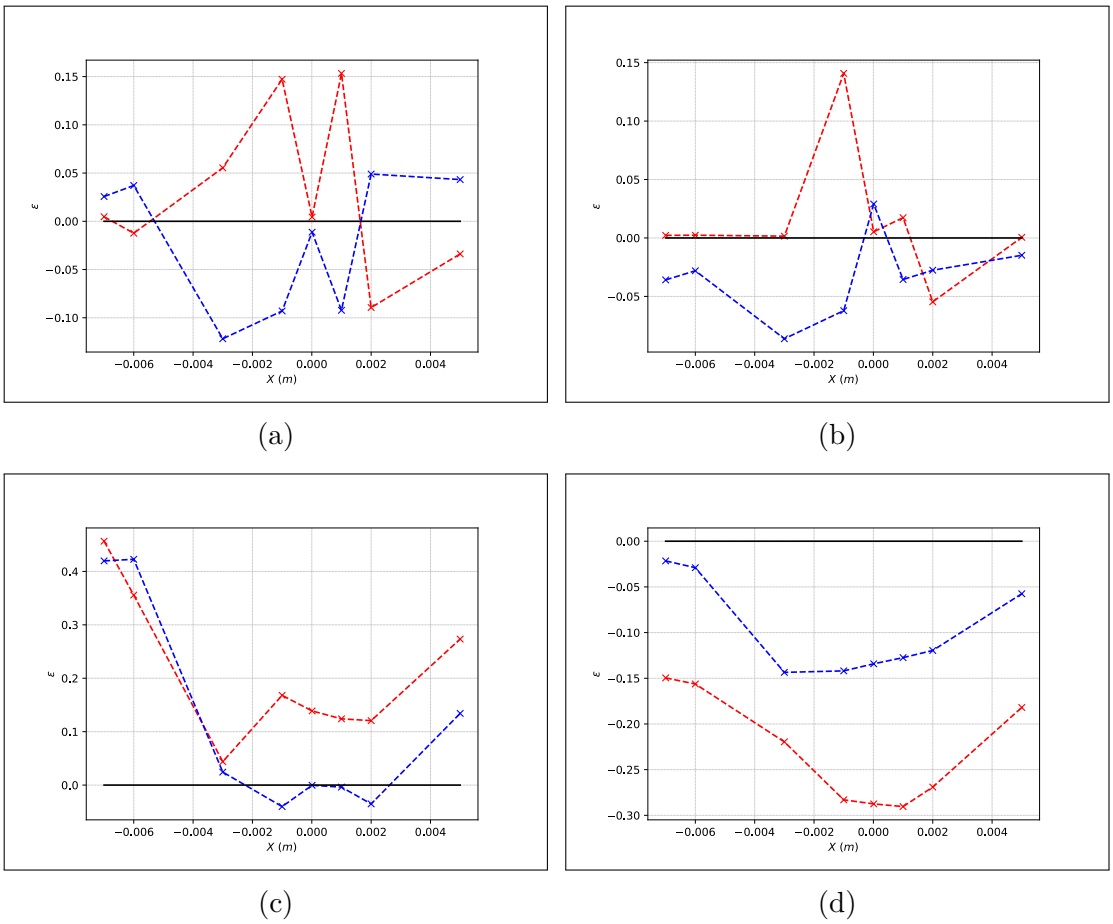

Figure B.3: Verification error calculated at data points (listed in Table 4.6) for the Grid Study. — : Coarse-Medium, — : Medium-Fine Grid Error. Plotting locations are (a)-(d) z_0, z_1, z_2, and z_3, respectively.

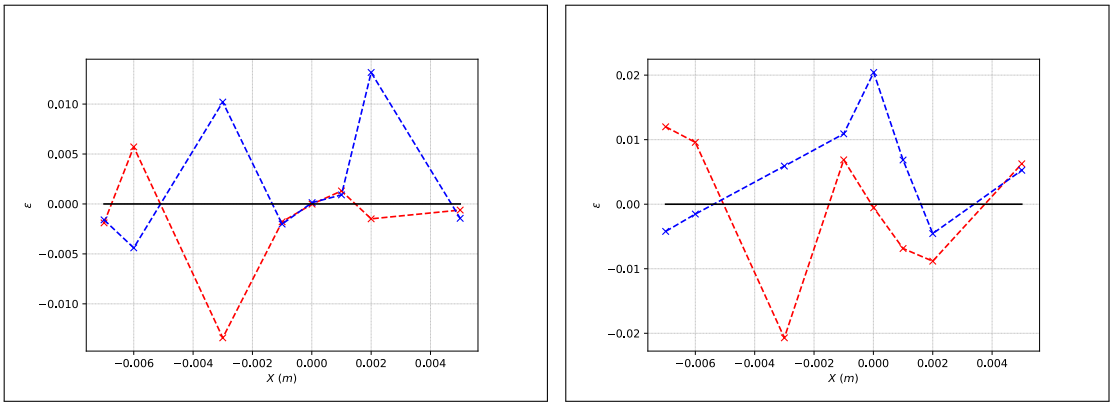

(a) (b)

(c) (d)

Figure B.4: Verification error calculated at data points (listed in Table 4.6) for the Time-step Study. : 0.002 - 0.001414, : 0.001414 - 0.001 Time-step Error. Plotting locations are (a)-(d) z_0, z_1, z_2, and z_3, respectively.

B.3 Validation

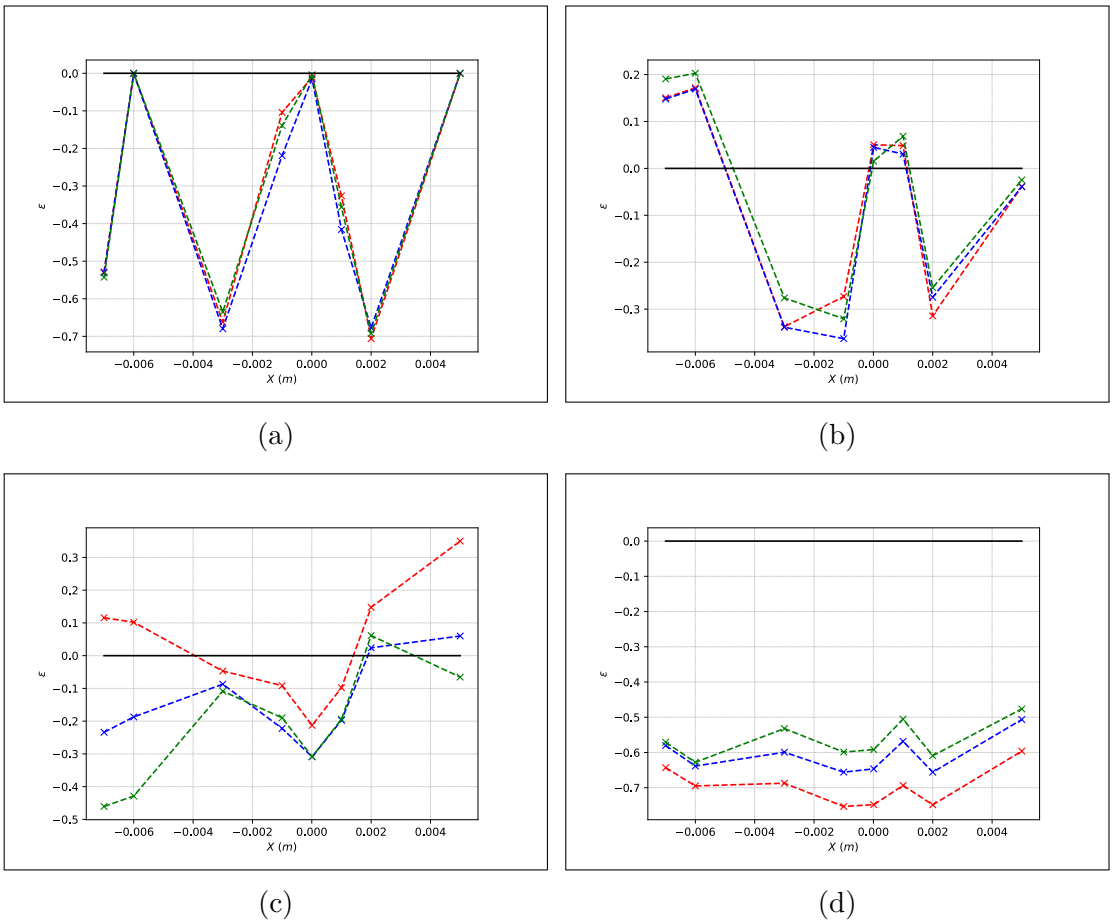

Figure B.5: Validation error calculated at data points (listed in Table 4.6) for the Grid Study. : Coarse, : Medium, : Fine Grid Error. Plotting locations are (a)-(d) z_0, z_1, z_2, and z_3, respectively.

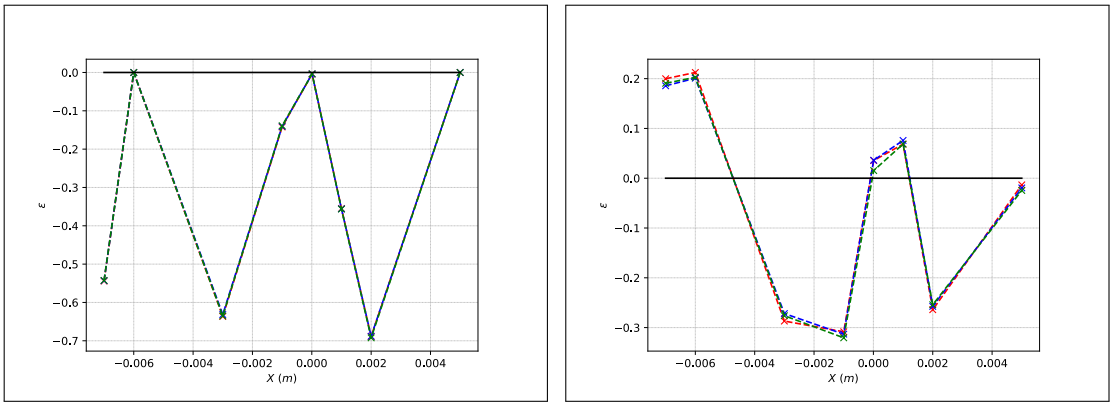

(a)

(b)

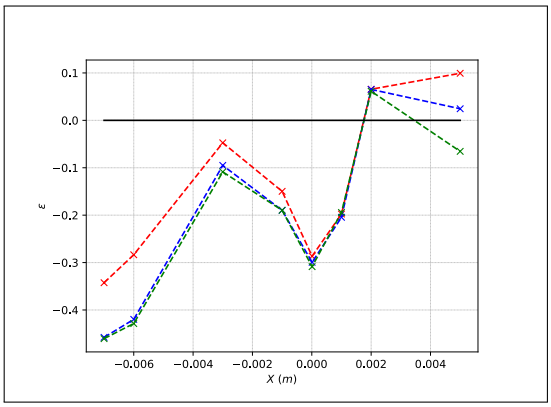

(c)

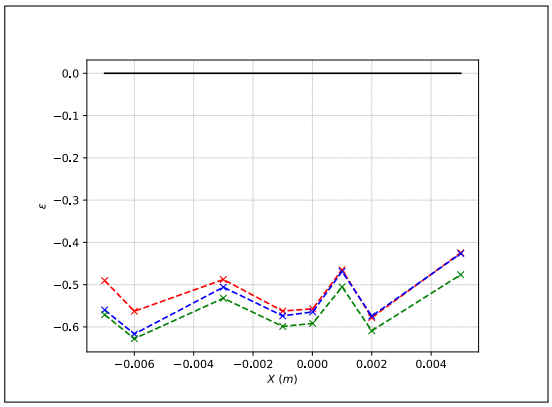

(d)

Figure B.6: Validation error calculated at data points (listed in Table 4.6) for the Time-step Study. : 0.002, : 0.001414, : 0.001 Time-step Error. Plotting locations are (a)-(d) z_0, z_1, z_2, and z_3, respectively.

Appendix C

JICF Verification: Grid Study

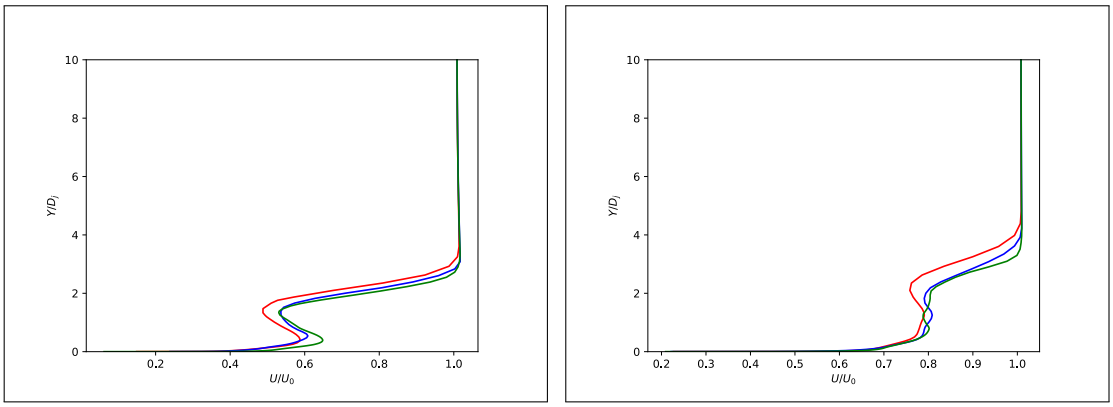

(a) $X/D = 5$

(b) $X/D = 10$

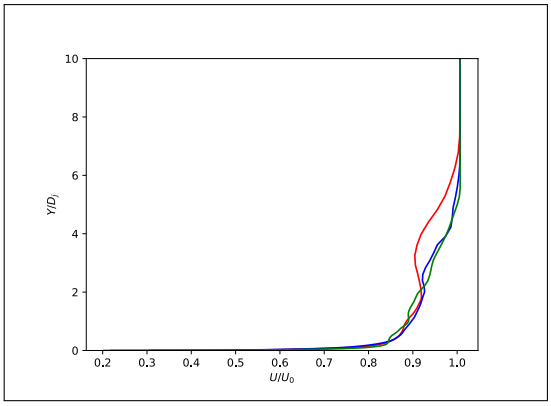

(c) $X/D = 20$

Figure C.1: Axial Velocity plots for the Grid Study. : Coarse, : Medium, : Fine.

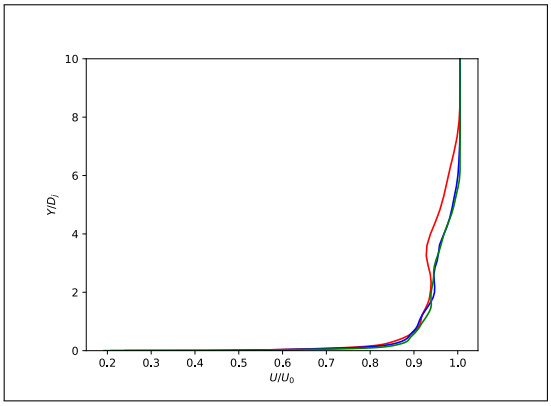

(d) $X/D = 50$

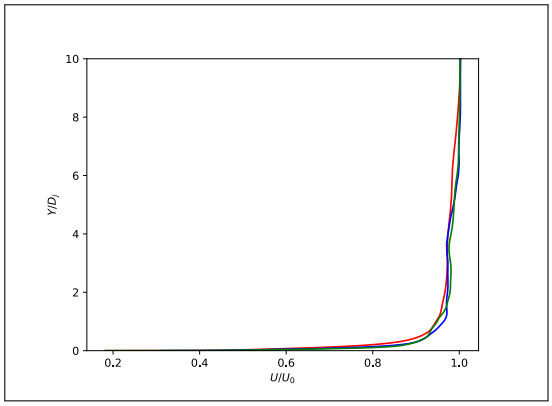

(e) $X/D = 100$

Figure C.1: Axial Velocity plots for the Grid Study. : Coarse, : Medium, : Fine.(cont.)

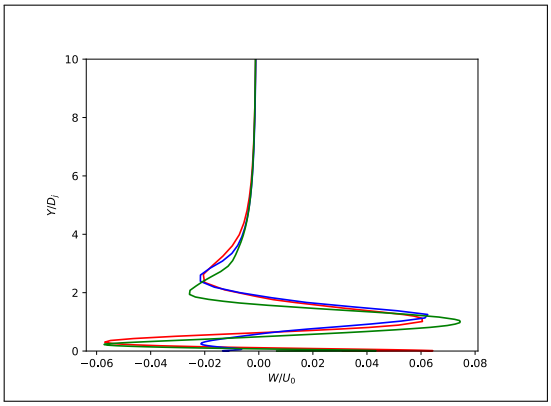

(a) $X/D = 5$

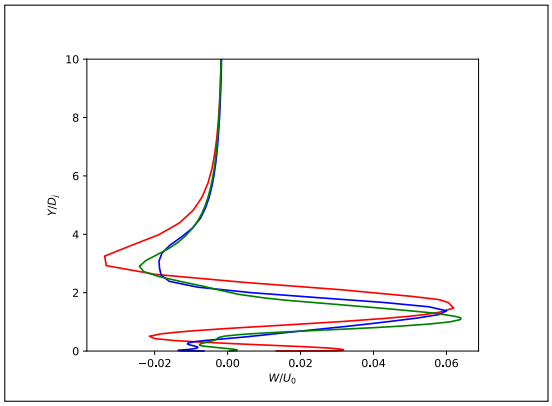

(b) $X/D = 10$

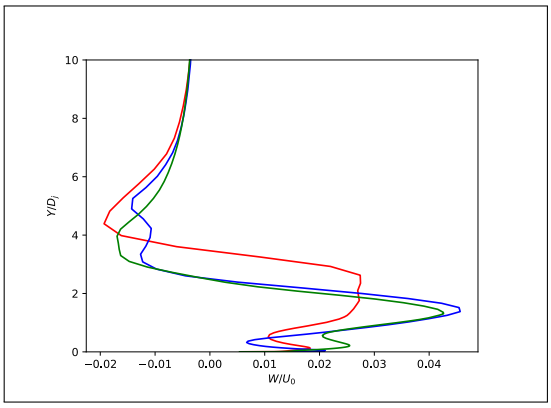

(c) $X/D = 20$

Figure C.2: Vertical Velocity plots for the Grid Study. : Coarse, : Medium, : Fine.

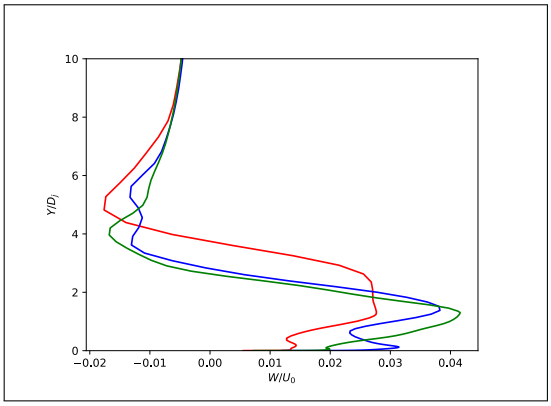

(d) $X/D = 50$

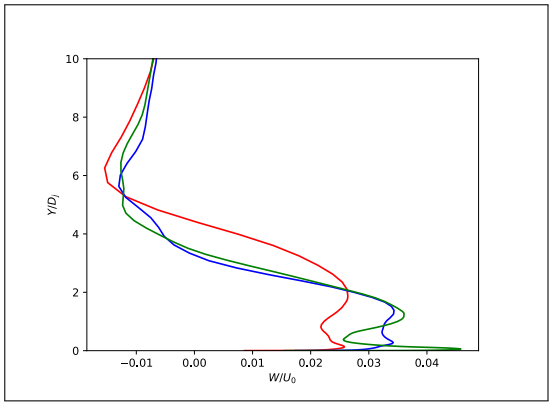

(e) $X/D = 100$

Figure C.2: Vertical Velocity plots for the Grid Study. : Coarse, : Medium, : Fine.(cont.)

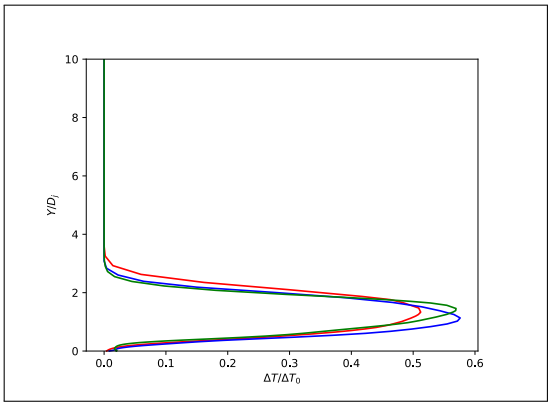

(a) $X/D = 5$

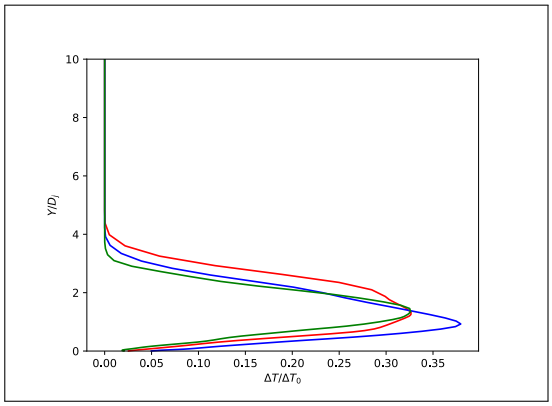

(b) $X/D = 10$

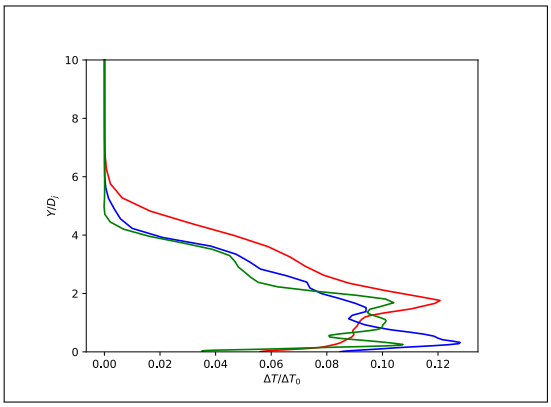

(c) $X/D = 20$

Figure C.3: Temperature Delta plots for the Grid Study. : Coarse, : Medium, : Fine.

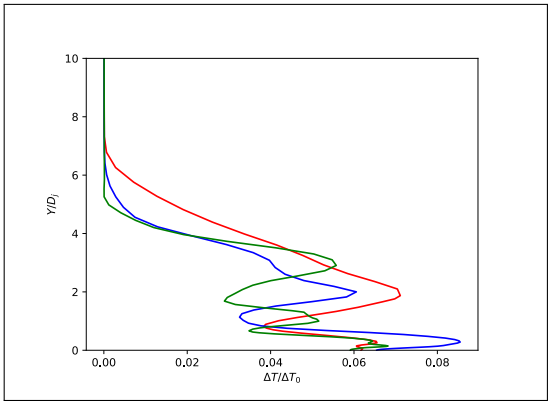

(d) $X/D = 50$

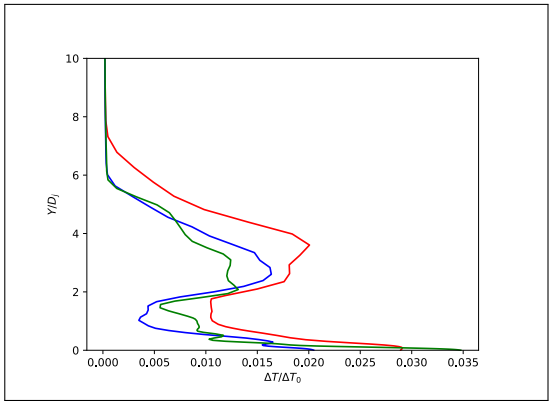

(e) $X/D = 100$

Figure C.3: Temperature Delta plots for the Grid Study. : Coarse, : Medium, : Fine. (cont.)

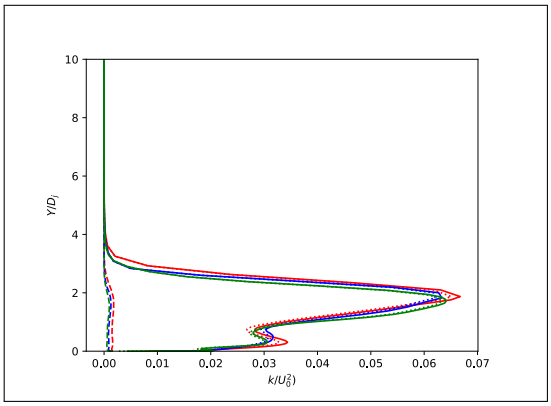

(a) $X/D = 5$

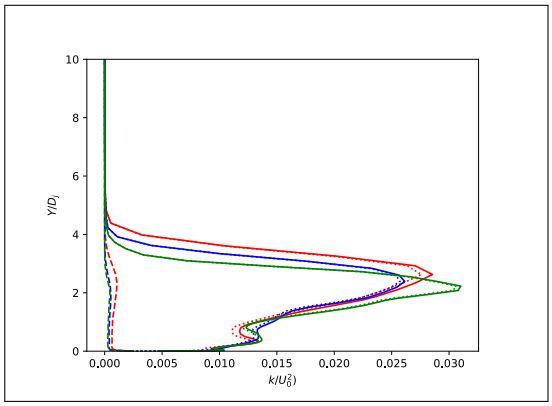

(b) $X/D = 10$

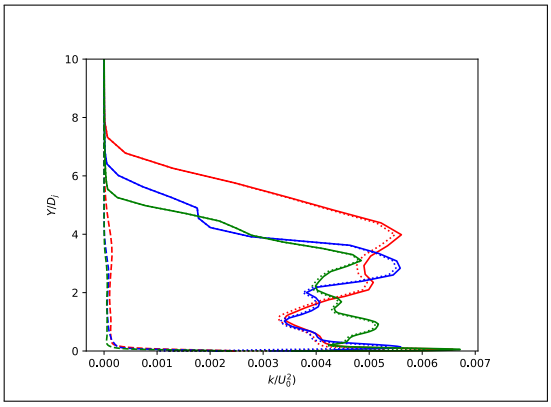

(c) $X/D = 20$

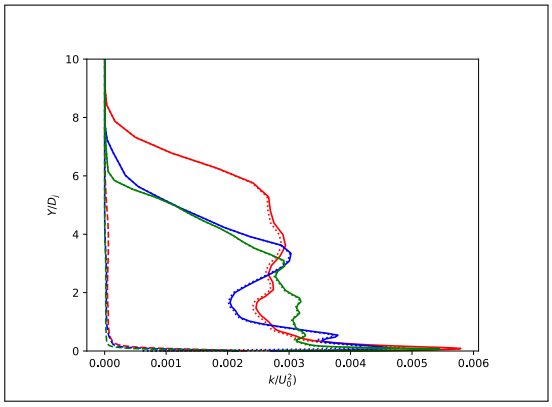

(d) $X/D = 50$

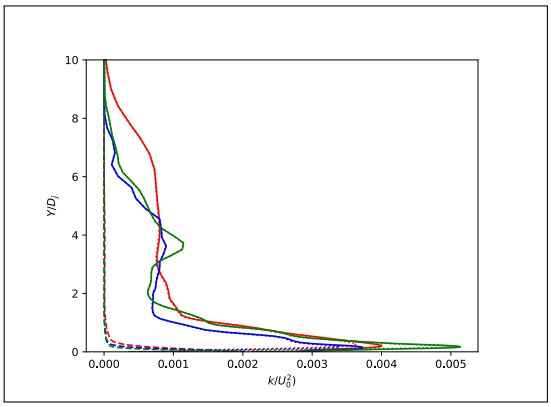

(e) $X/D = 100$

Figure C.4: Turbulent Kinetic Energy plots for the Grid Study. : Coarse, : Medium, : Fine. Dotted: Resolved, Dashed: Modeled, Solid: Total (Resolved + Modeled).

Appendix D

JICF Turbulence Study

D.1 3D Visualizations

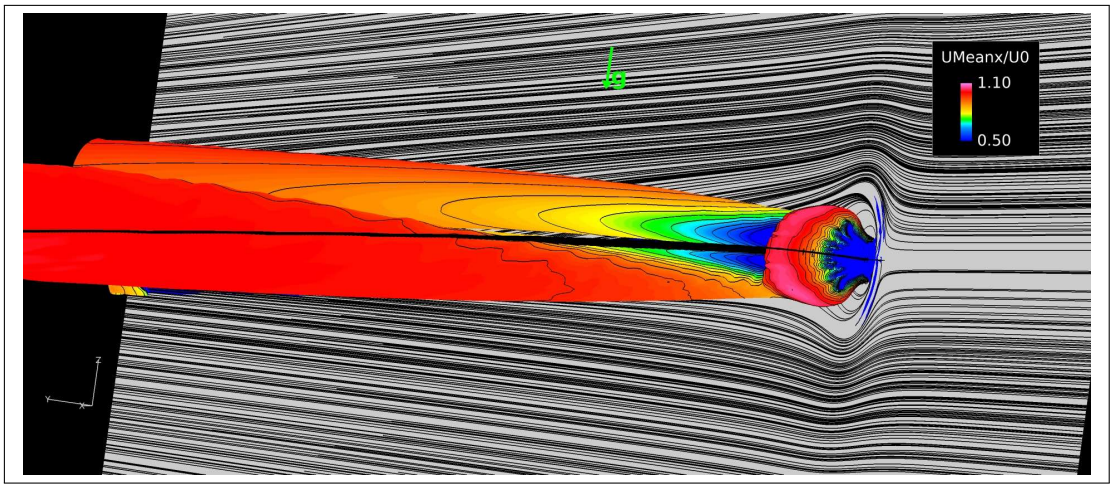

(a) RANS

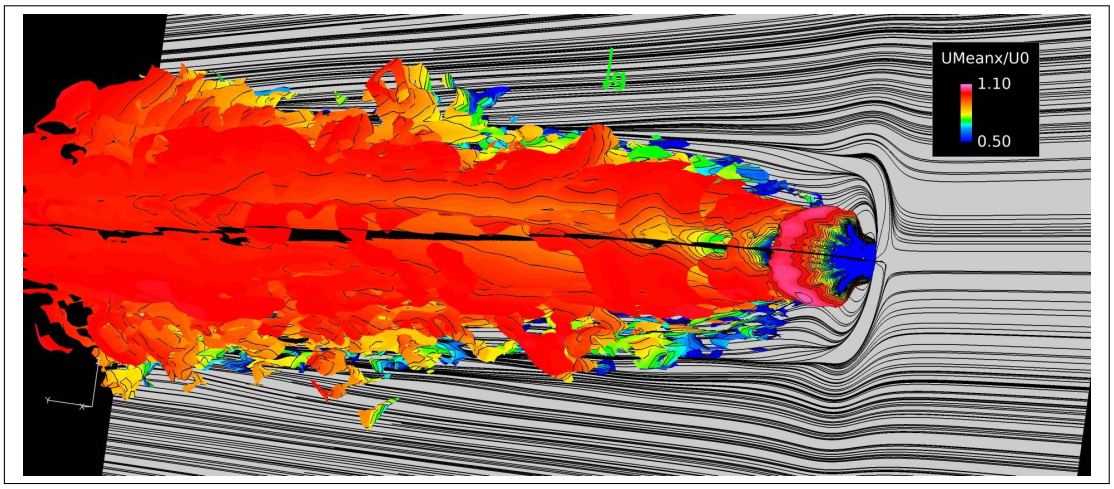

(b) HRLES

Figure D.1: Visualization of Q-criterion for $(400D/U_0)^2Q = 0.1$, colored by Axial Velocity.

D.2 2D/3D Visualizations

D.2.1 Axial Velocity

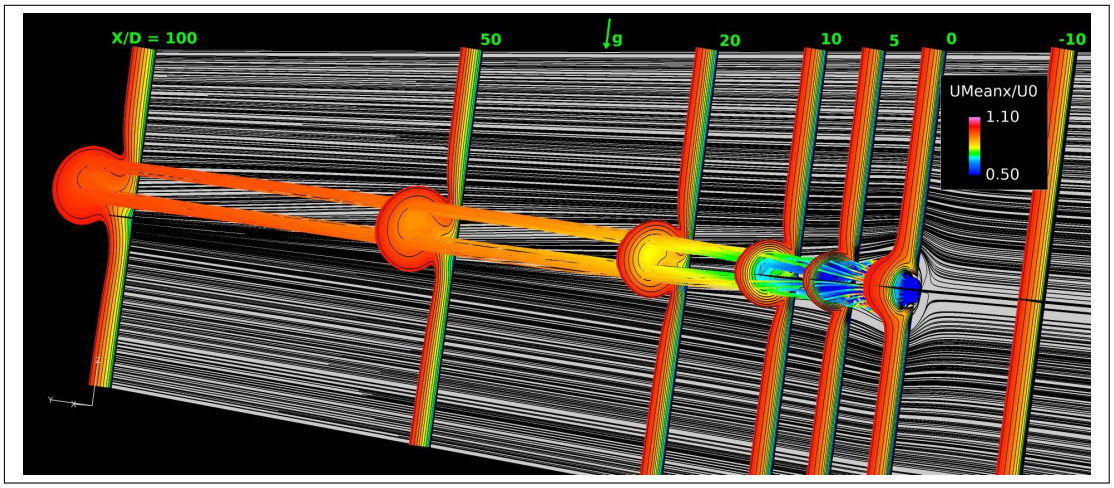

(a) RANS

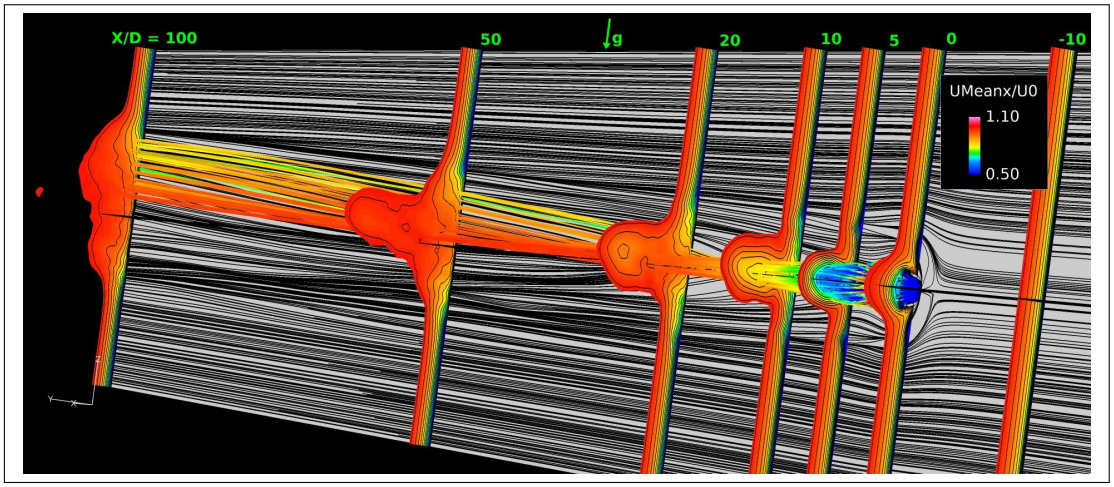

(b) HRLES

Figure D.2: Spacial evolution of cross plane contours colored by Axial Velocity, with streamlines emerging from the jet.

D.2.2 Temperature Delta

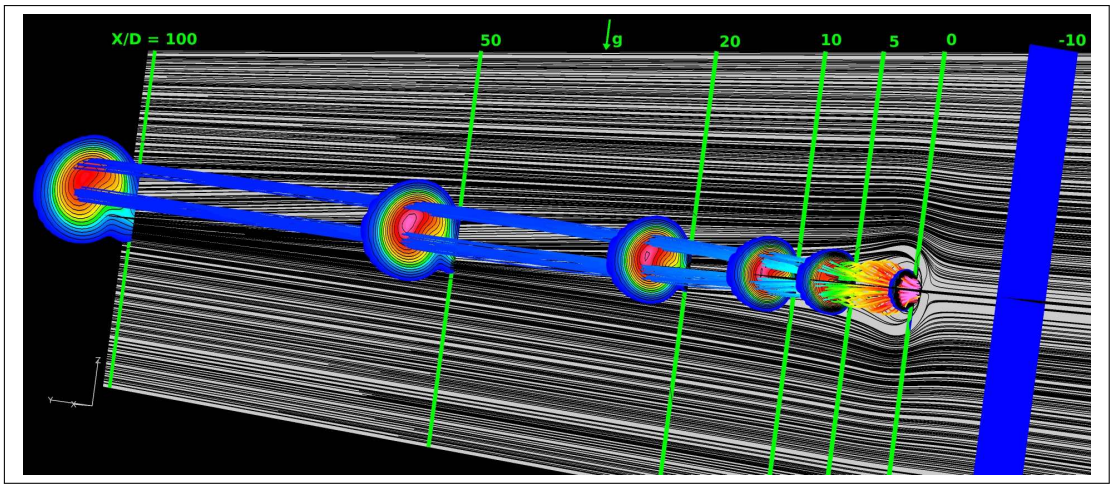

(a) RANS

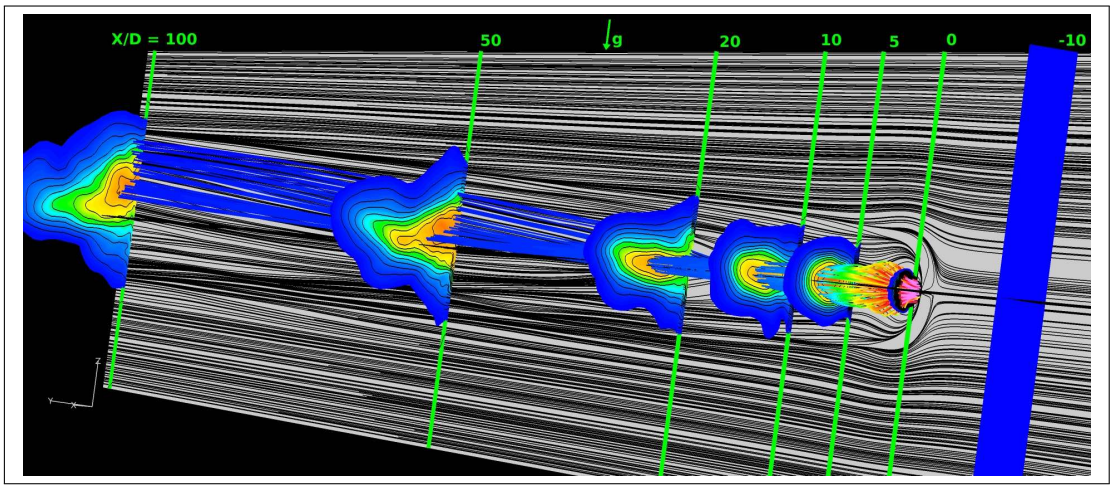

(b) HRLES

Figure D.3: Spacial evolution of cross plane contours colored by Temperature Delta, with streamlines emerging from the jet. (Maximum contour value varies with axial location given by the expression, $\Delta T^*_{MAX} = 4/3(X/D)^{-2/3}$)

D.3 Data Plots

D.3.1 Boundary Layer Profiles

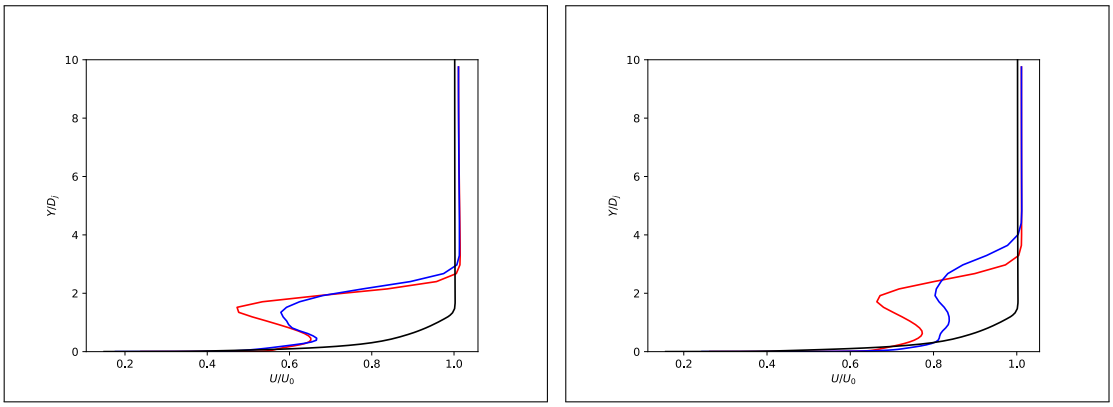

(a) $X/D = 5$ (b) $X/D = 10$

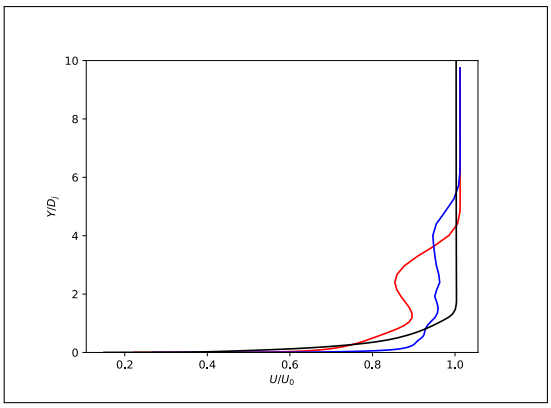

(c) $X/D = 20$

Figure D.4: Axial Velocity plots for the Turbulence Model Study. — : RANS, — : HRLES

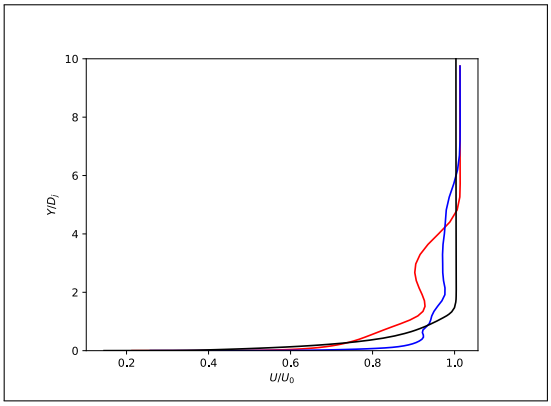

(d) $X/D = 50$

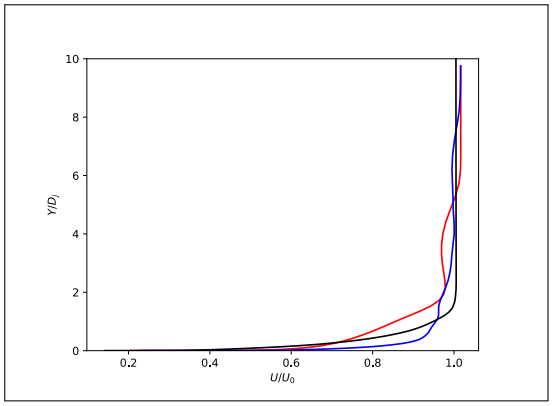

(e) $X/D = 100$

Figure D.4: Axial Velocity plots for the Turbulence Model Study. : RANS, : HRLES(cont.)

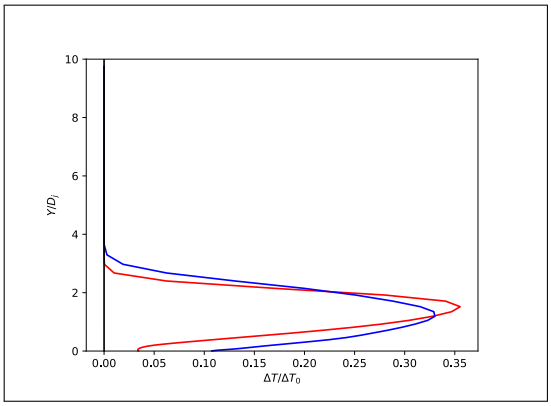

(a) $X/D = 5$

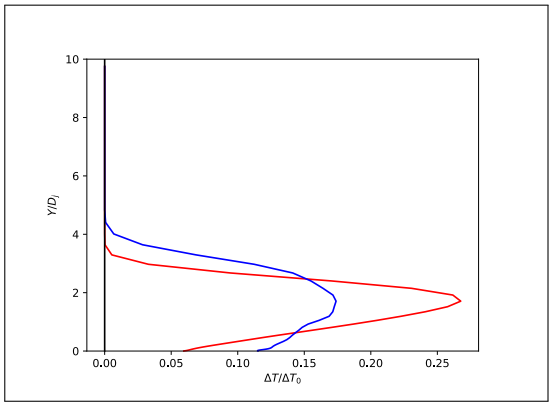

(b) $X/D = 10$

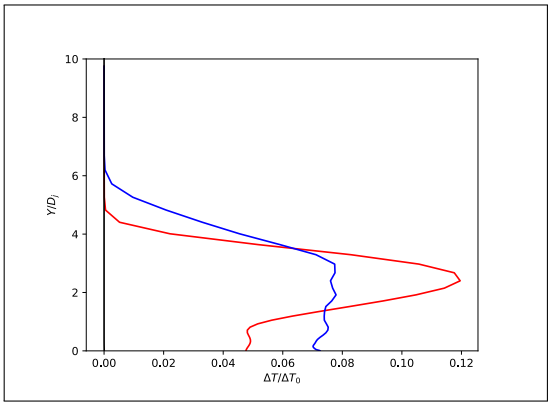

(c) $X/D = 20$

Figure D.5: Temperature Delta plots for the Turbulence Model Study. : RANS, : HRLES

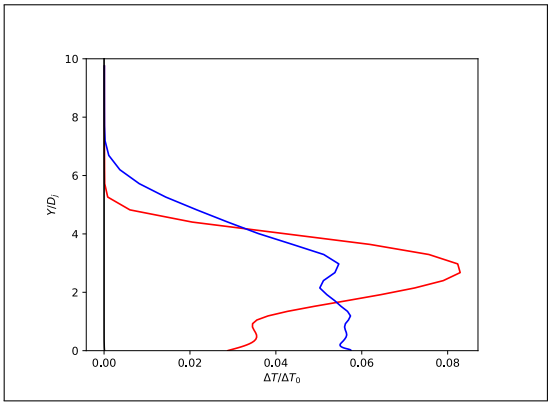

(d) $X/D = 50$

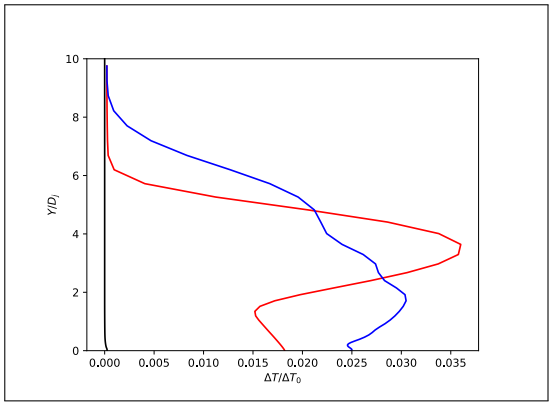

(e) $X/D = 100$

Figure D.5: Temperature Delta plots for the Turbulence Model Study. : RANS, : HRLES(cont.)

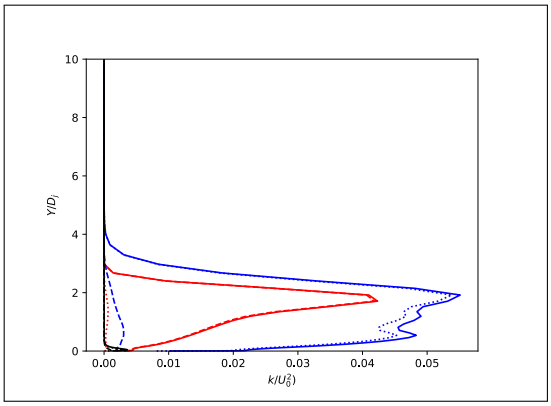

(a) $X/D = 5$

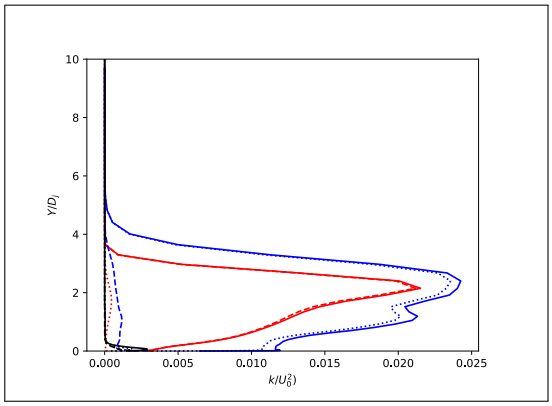

(b) $X/D = 10$

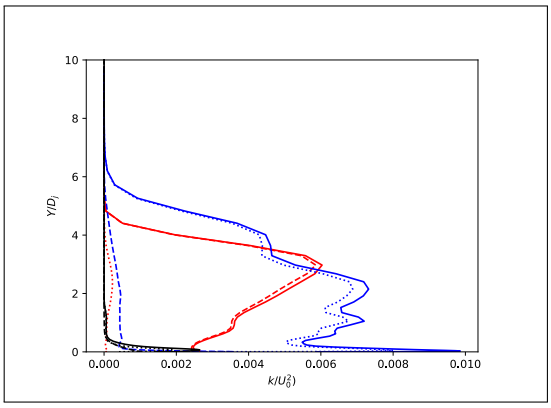

(c) $X/D = 20$

Figure D.6: Turbulent Kinetic Energy plots for the Turbulence Model Study. : RANS, : HRLES

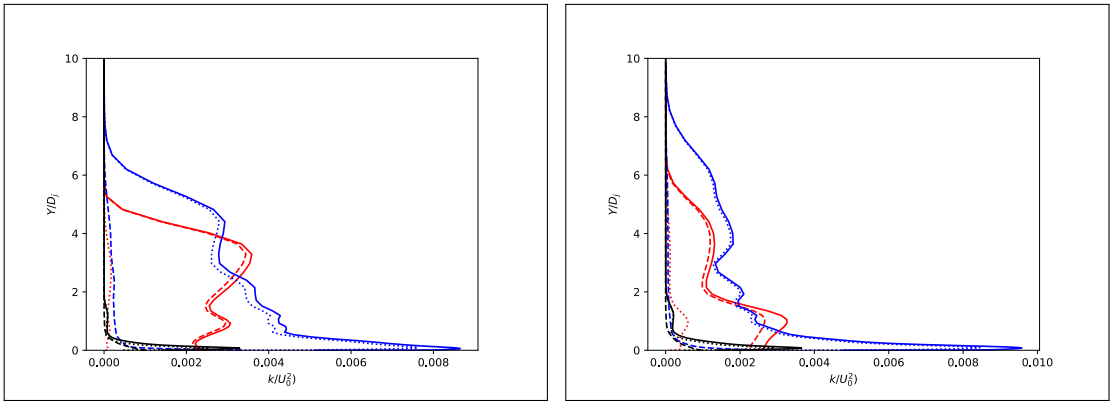

(d) $X/D = 50$ (e) $X/D = 100$

Figure D.6: Turbulent Kinetic Energy plots for the Turbulence Model Study. : RANS, : HRLES(cont.)

D.3.2 Wake Plots

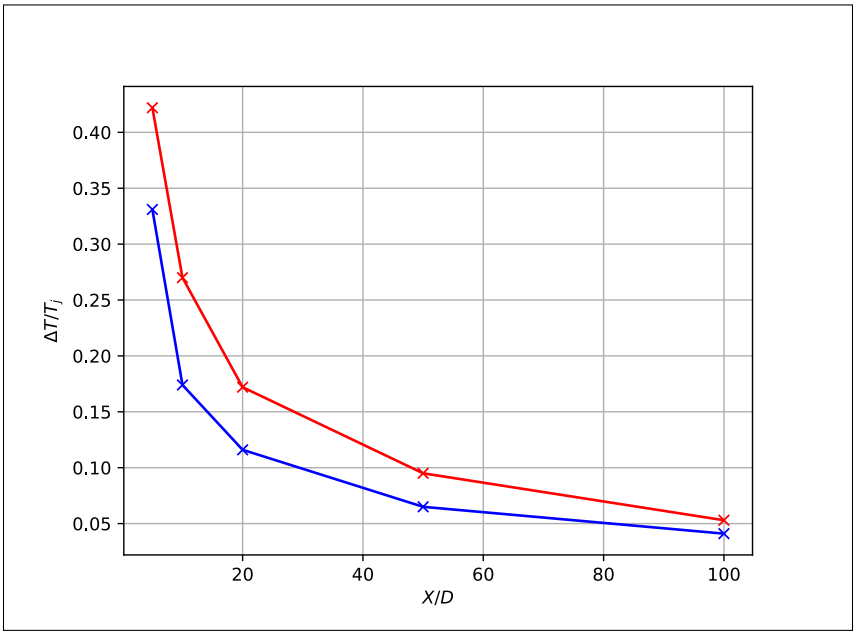

Figure D.7: Centerline Temperature Delta for the Turbulence Model Study. : RANS, : HRLES.

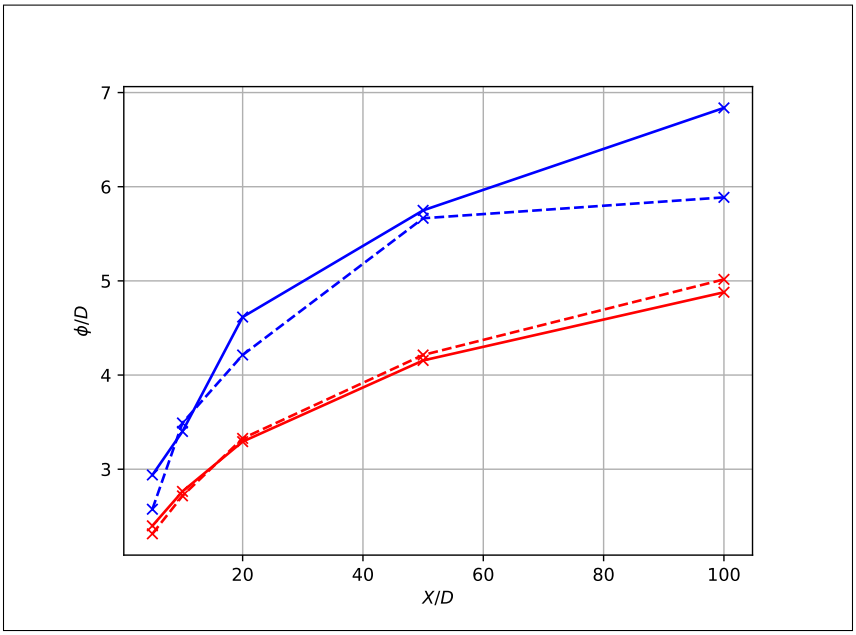

Figure D.8: Wake Height (Dashed) and Width (Solid) for the Turbulence Model Study. : RANS, : HRLES.

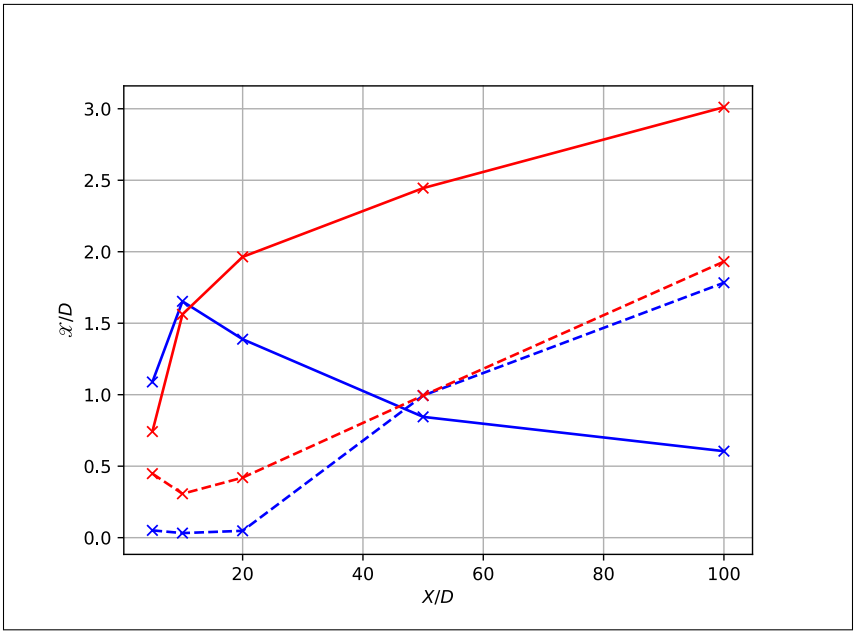

Figure D.9: Centerline Wake Vertical (Dashed) and Horizontal (Solid) position for the Turbulence Model Study. : RANS, : HRLES.

D.4 Cross Plane Contours

D.4.1 Axial Velocity

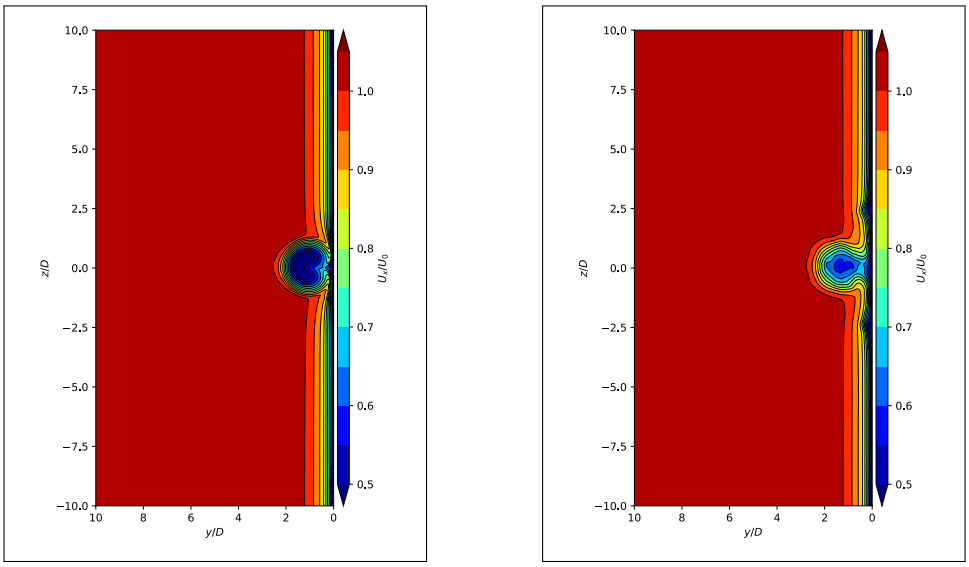

(a) RANS (b) HRLES

Figure D.10: Axial Velocity cross plane controus at $X/D = 5$.

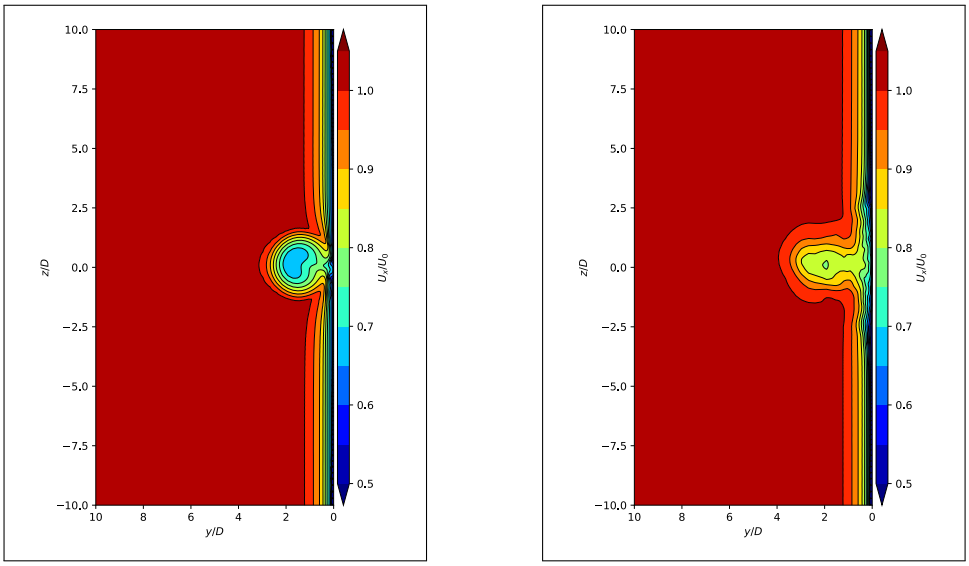

(a) RANS (b) HRLES

Figure D.11: Axial Velocity cross plane controus at $X/D = 10$.

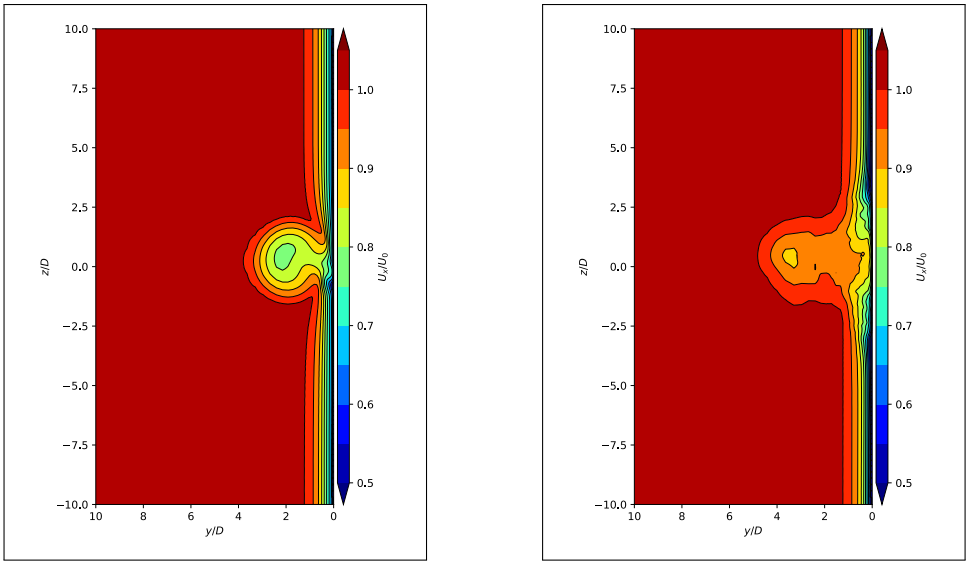

(a) RANS (b) HRLES

Figure D.12: Axial Velocity cross plane controus at $X/D = 20$.

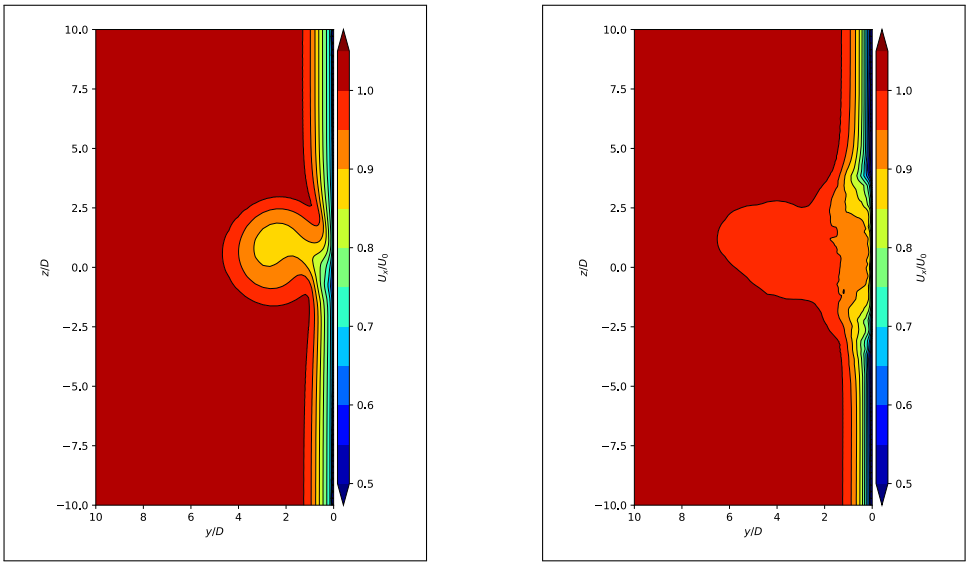

(a) RANS (b) HRLES

Figure D.13: Axial Velocity cross plane controus at $X/D = 50$.

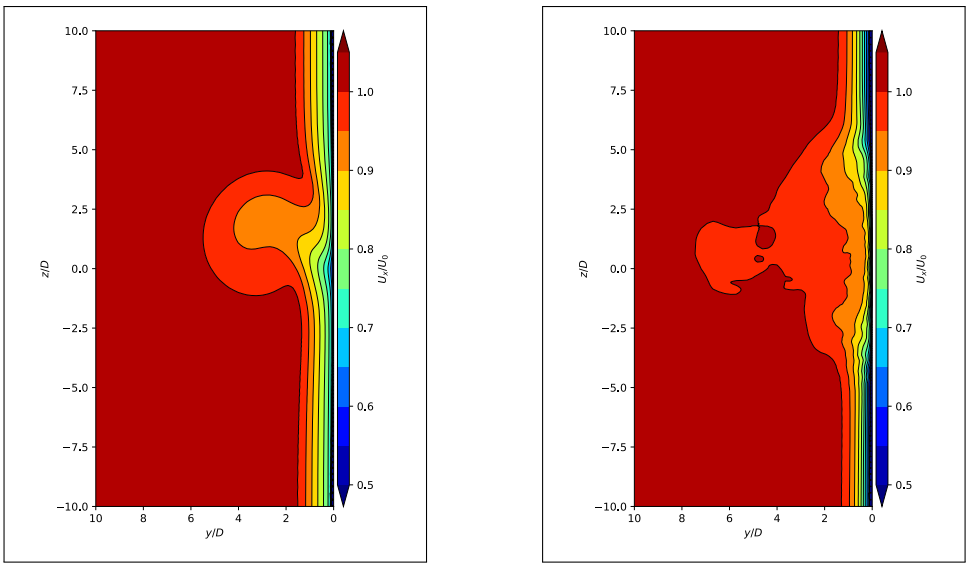

(a) RANS (b) HRLES

Figure D.14: Axial Velocity cross plane controus at $X/D = 100$.

D.4.2 Temperature Delta

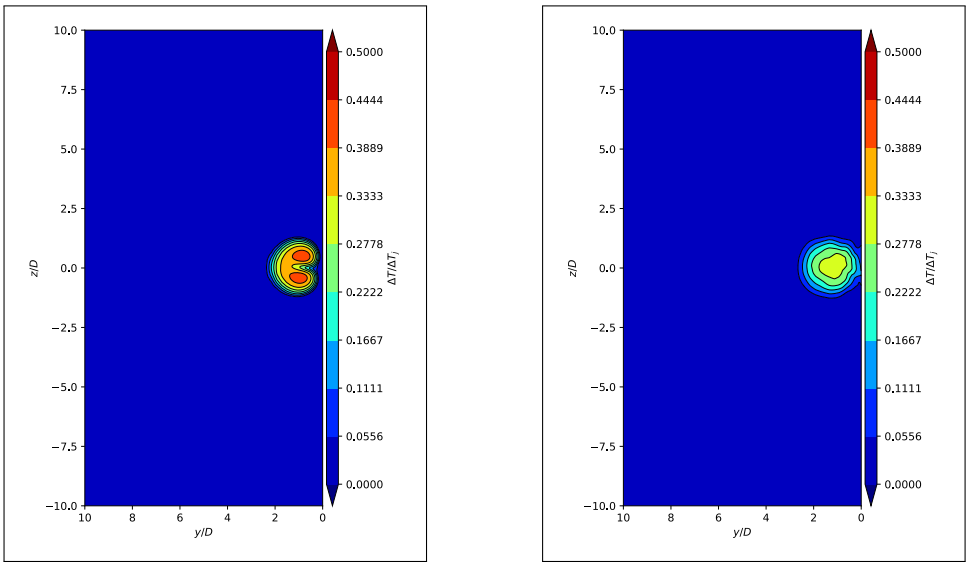

(a) RANS (b) HRLES

Figure D.15: Temperature Delta cross plane controus at $X/D = 5$.

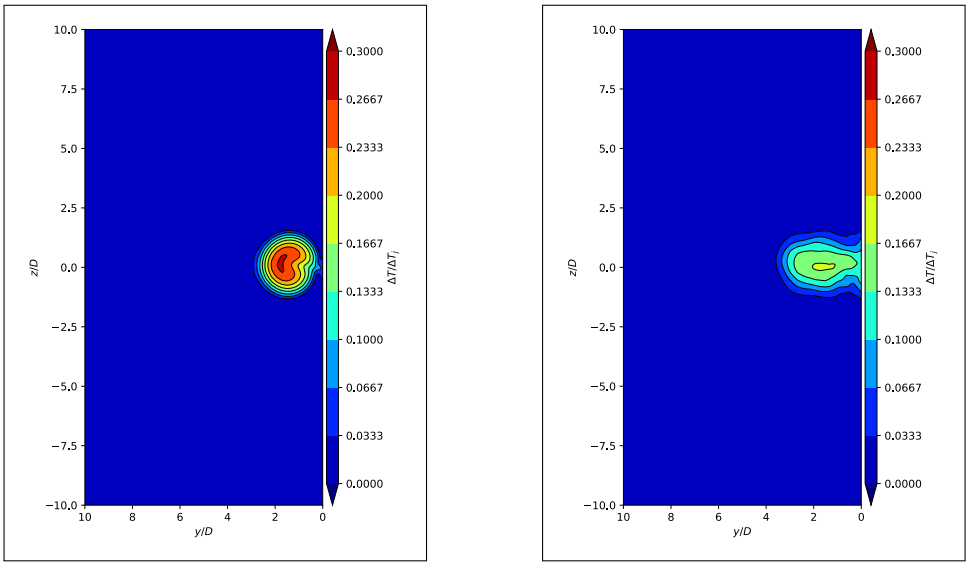

(a) RANS (b) HRLES

Figure D.16: Temperature Delta cross plane controus at $X/D = 10$.

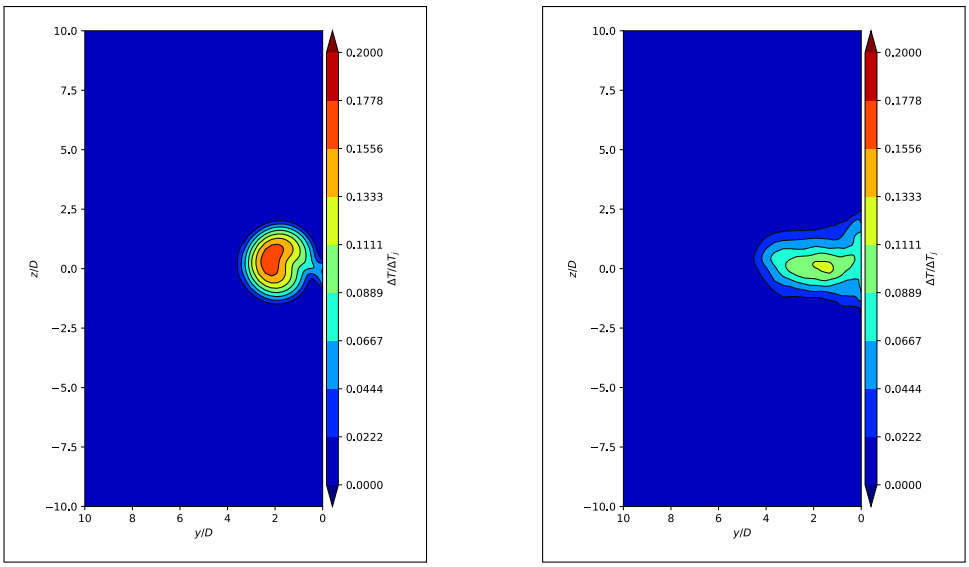

(a) RANS (b) HRLES

Figure D.17: Temperature Delta cross plane controus at $X/D = 20$.

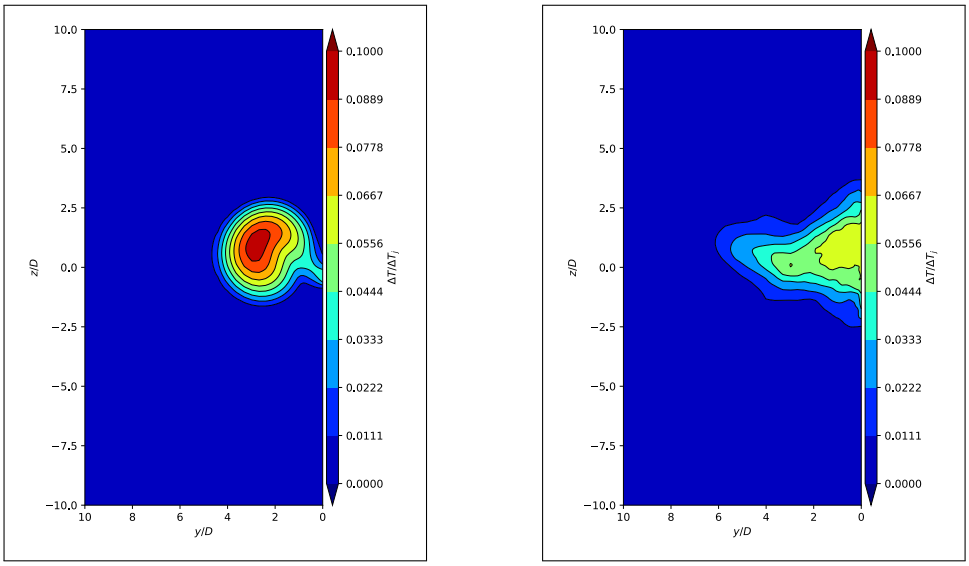

(a) RANS (b) HRLES

Figure D.18: Temperature Delta cross plane controus at $X/D = 50$.

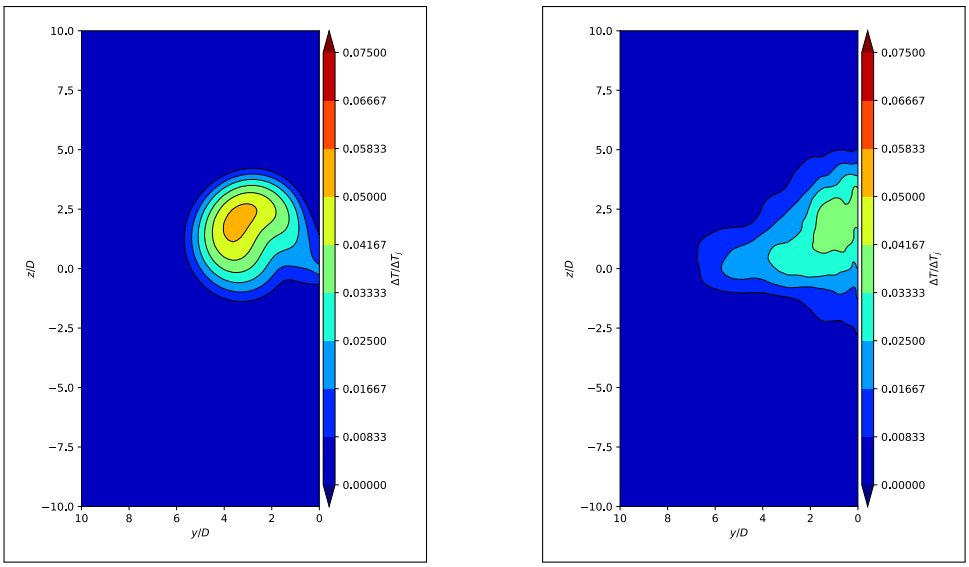

(a) RANS (b) HRLES

Figure D.19: Temperature Delta cross plane controus at $X/D = 100$.

Appendix E

JICF Heated Study

E.1 3D Visualizations

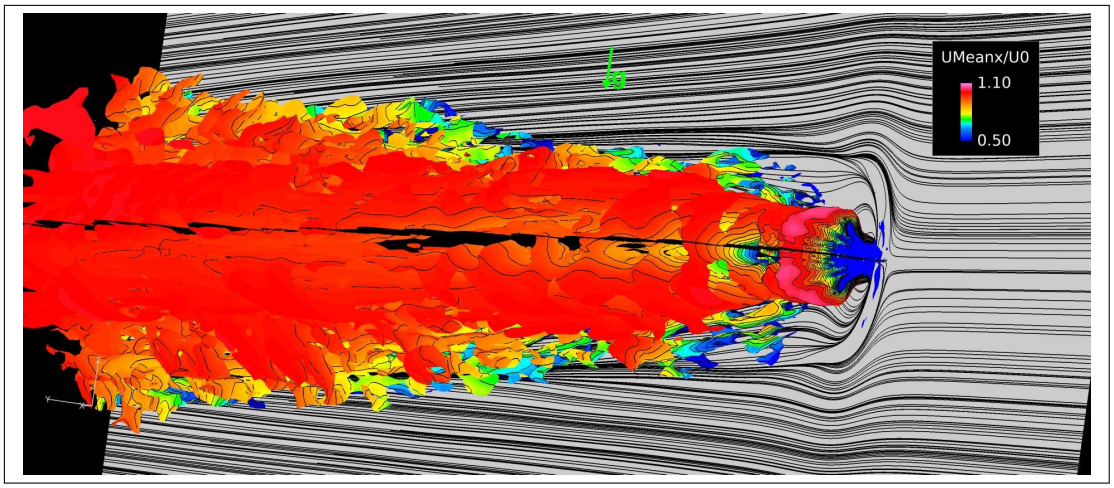

(a) Non-Heated

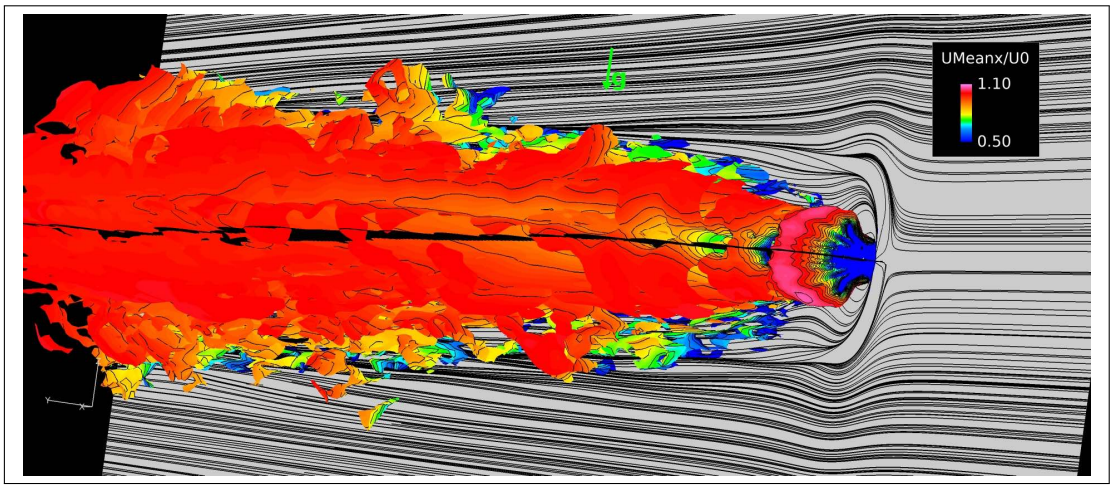

(b) Heated

Figure E.1: Visualization of Q-criterion for $(400D/U_0)^2Q = 0.1$, colored by Axial Velocity.

E.2 2D/3D Visualizations

E.2.1 Axial Velocity

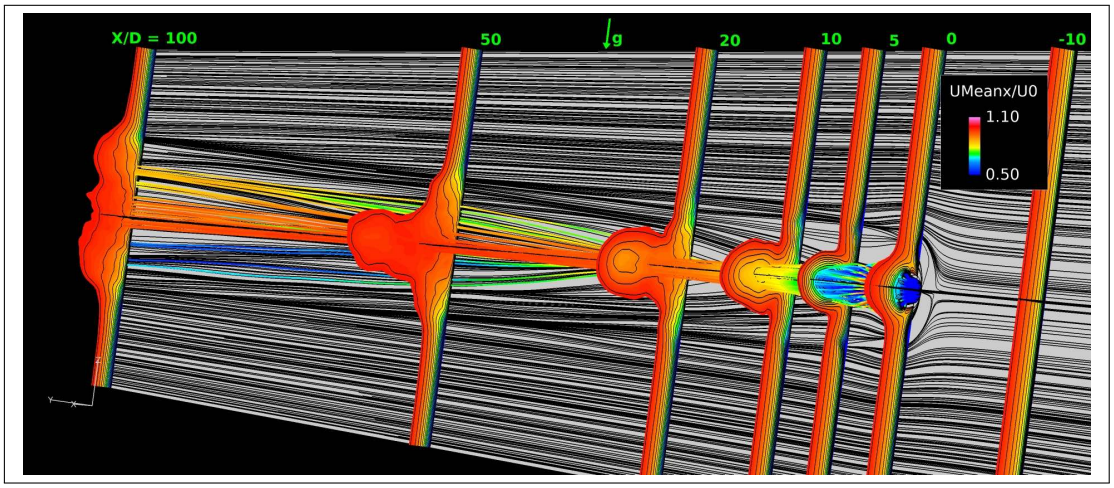

(a) Non-Heated

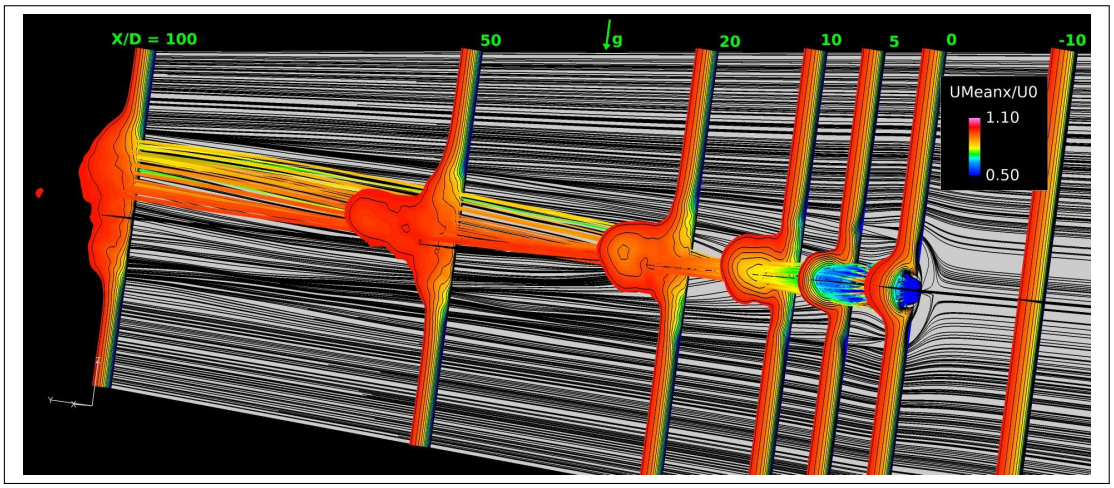

(b) Heated

Figure E.2: Spacial evolution of cross plane contours colored by Axial Velocity, with streamlines emerging from the jet.

E.2.2 Scalar Tracer Concentration

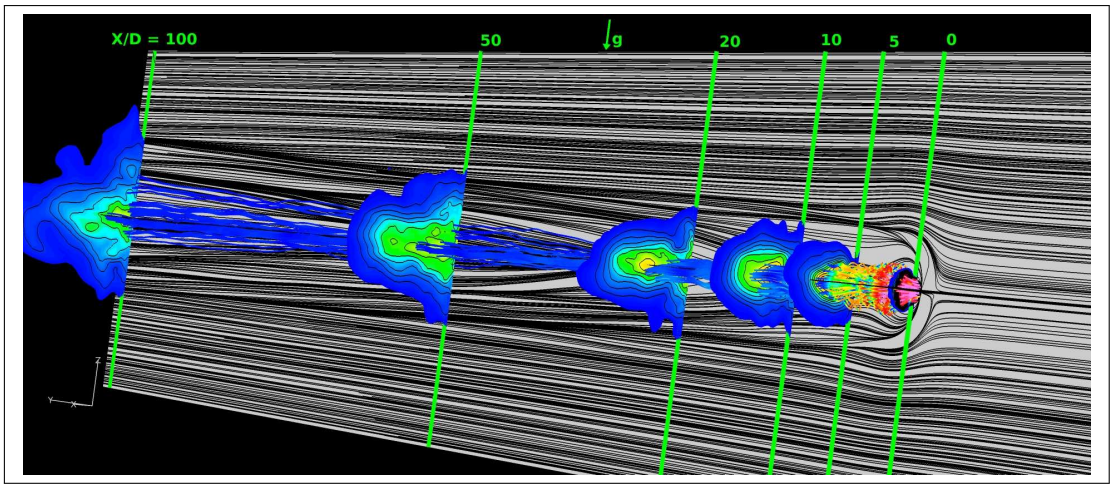

(a) Non-Heated

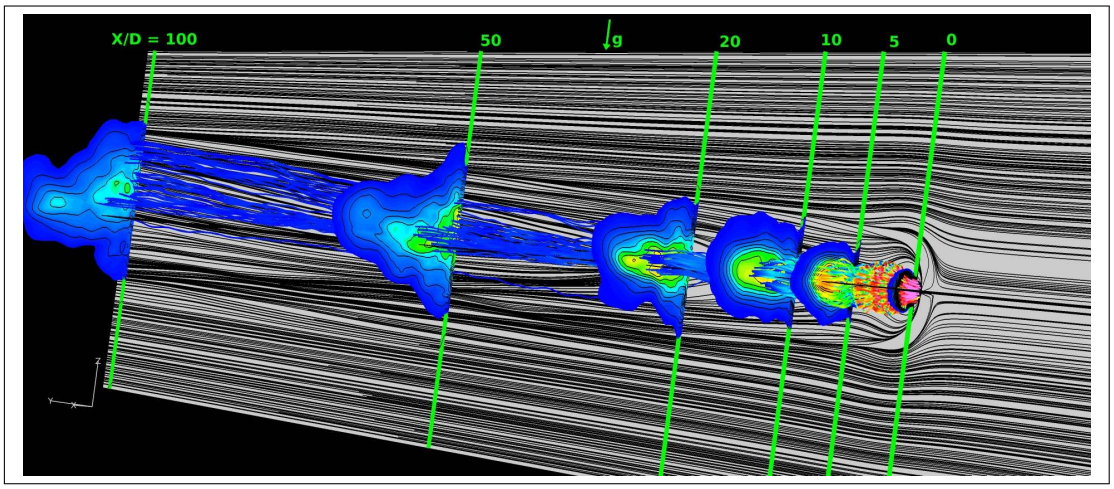

(b) Heated

Figure E.3: Spacial evolution of cross plane contours colored by Tracer Concentration, with streamlines emerging from the jet. (Maximum contour value varies with axial location given by the expression, $C_{MAX} = 4/3(X/D)^{-2/3}$)

E.3 Data Plots

E.3.1 Boundary Layer Profiles

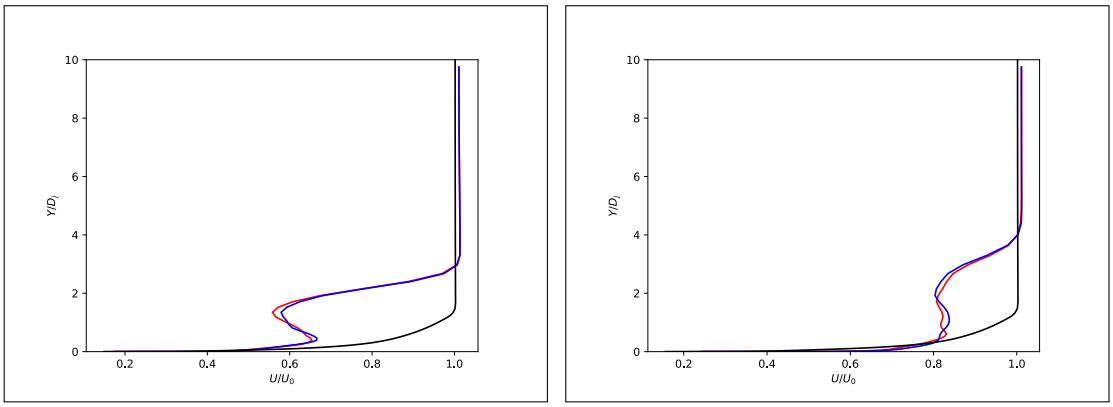

(a) $X/D = 5$

(b) $X/D = 10$

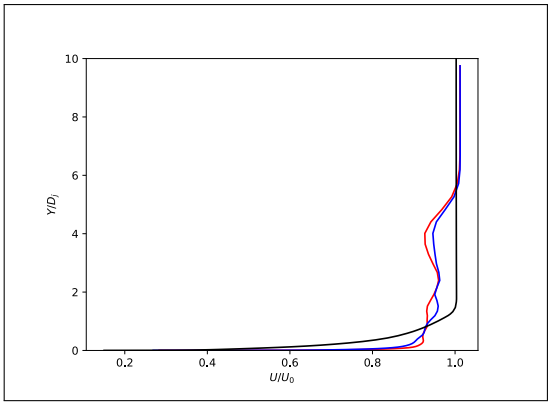

(c) $X/D = 20$

Figure E.4: Axial Velocity plots for the Heated Study. : Non-Heated, : Heated, : No-jet calculation.

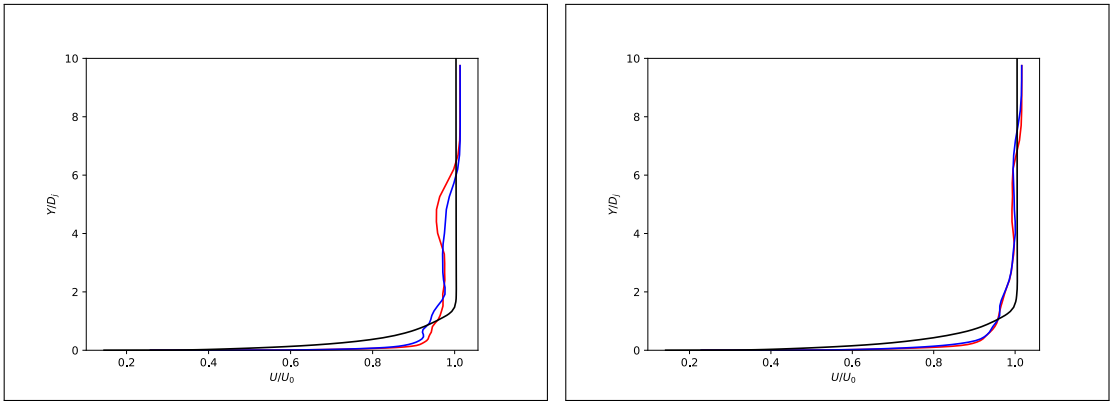

(d) $X/D = 50$ (e) $X/D = 100$

Figure E.4: Axial Velocity plots for the Heated Study. : Non-Heated, : Heated, : No-jet calculation.(cont.)

E.3.2 Wake Plots

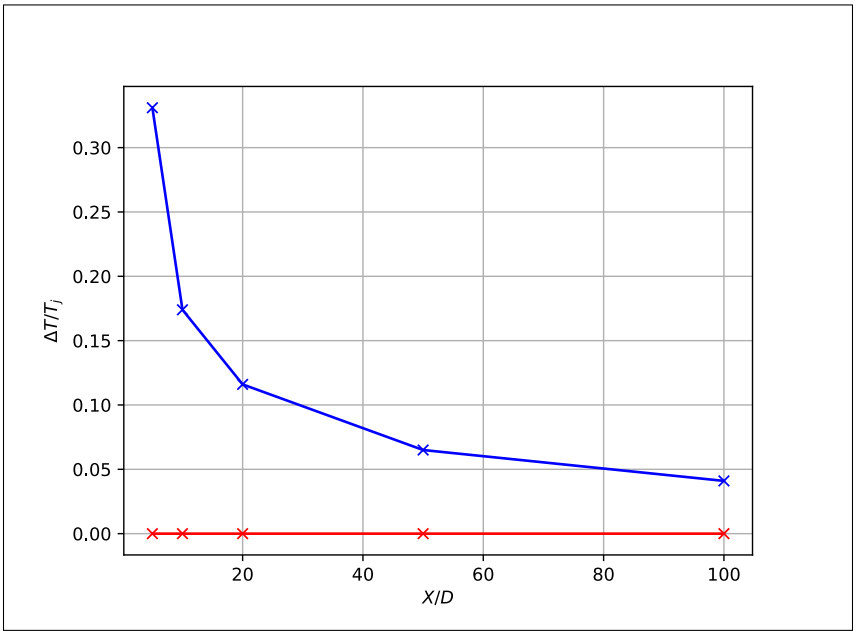

Figure E.5: Centerline Temperature Delta for the Heated Study. : Non-Heated, : Heated.

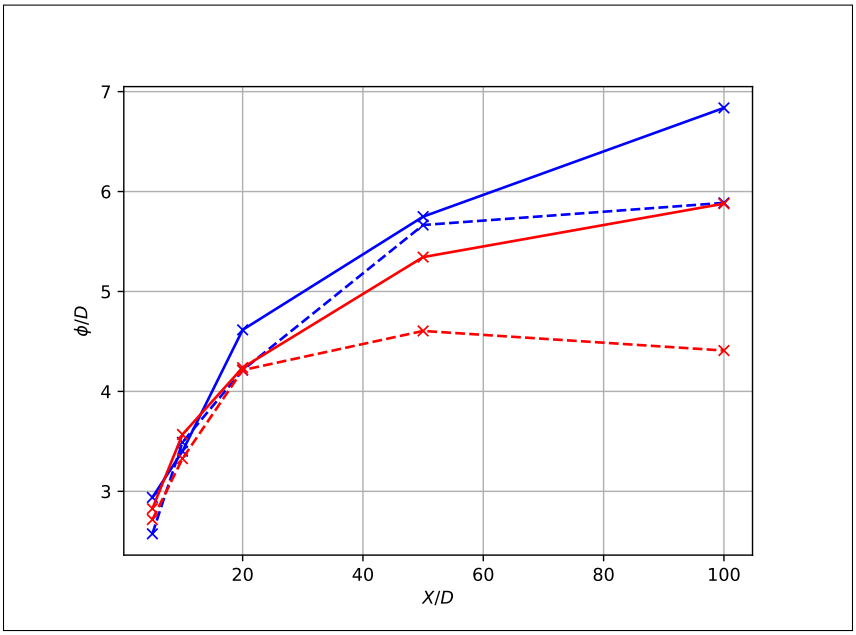

Figure E.6: Wake Height (Dashed) and Width (Solid) for the Heated Study. : Non-Heated, : Heated.

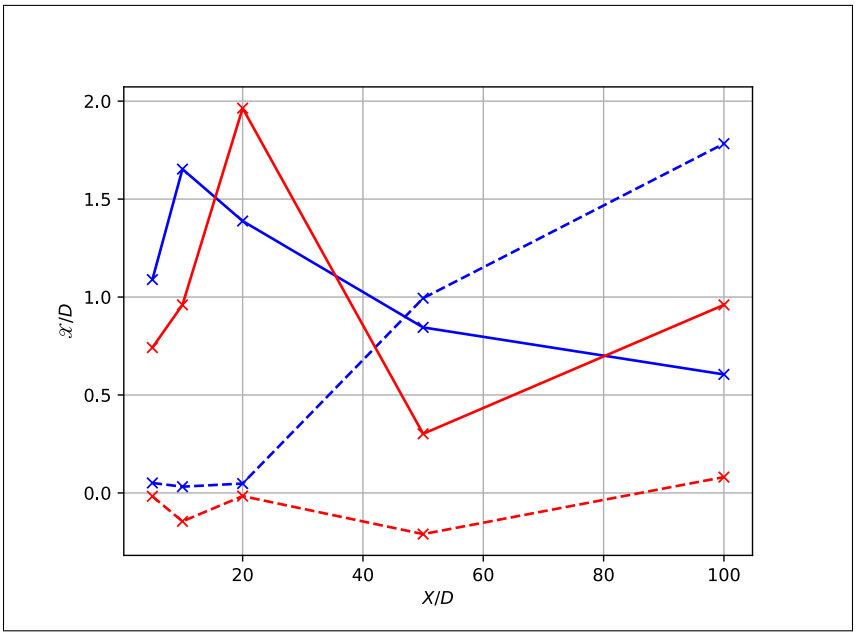

Figure E.7: Centerline Wake Vertical (Dashed) and Horizontal (Solid) position for the Heated Study. : Non-Heated, : Heated.

E.4 Cross Plane Contours

E.4.1 Axial Velocity

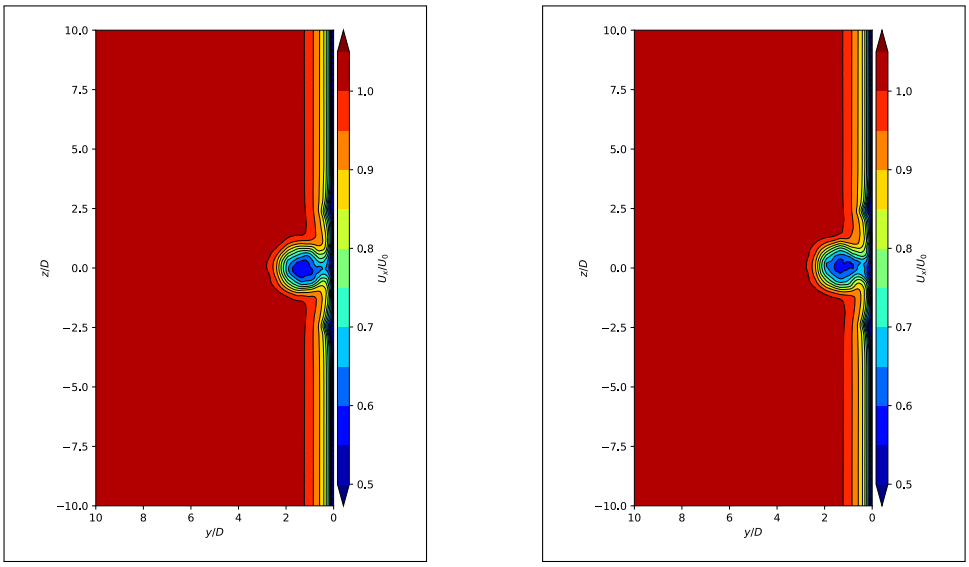

(a) Non-Heated (b) Heated

Figure E.8: Axial Velocity cross plane controus at $X/D = 5$.

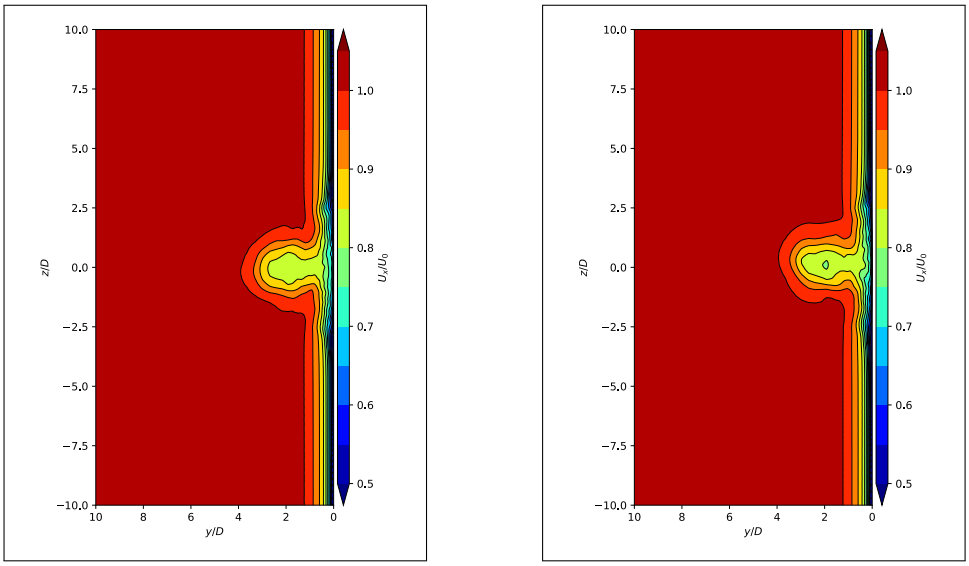

(a) Non-Heated (b) Heated

Figure E.9: Axial Velocity cross plane controus at $X/D = 10$.

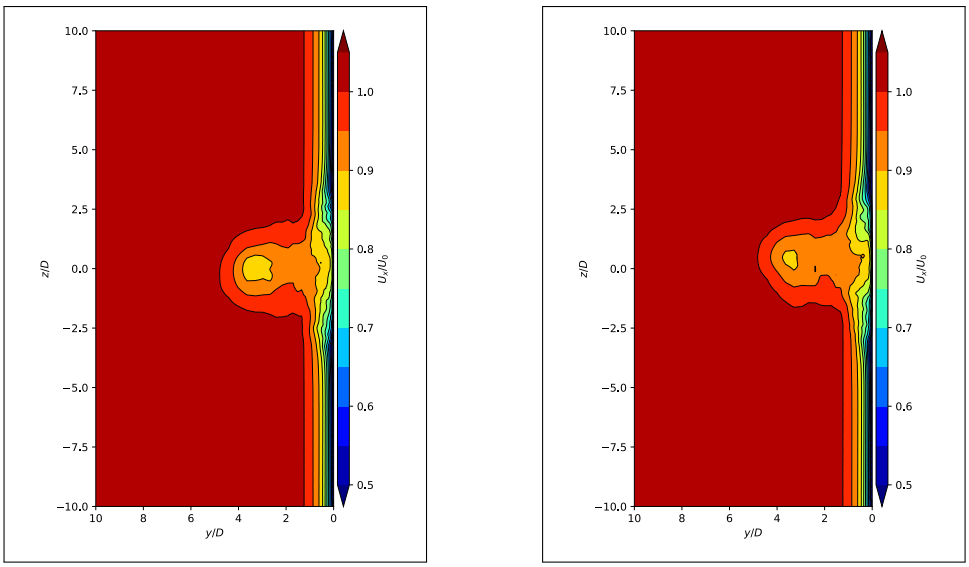

(a) Non-Heated (b) Heated

Figure E.10: Axial Velocity cross plane controus at $X/D = 20$.

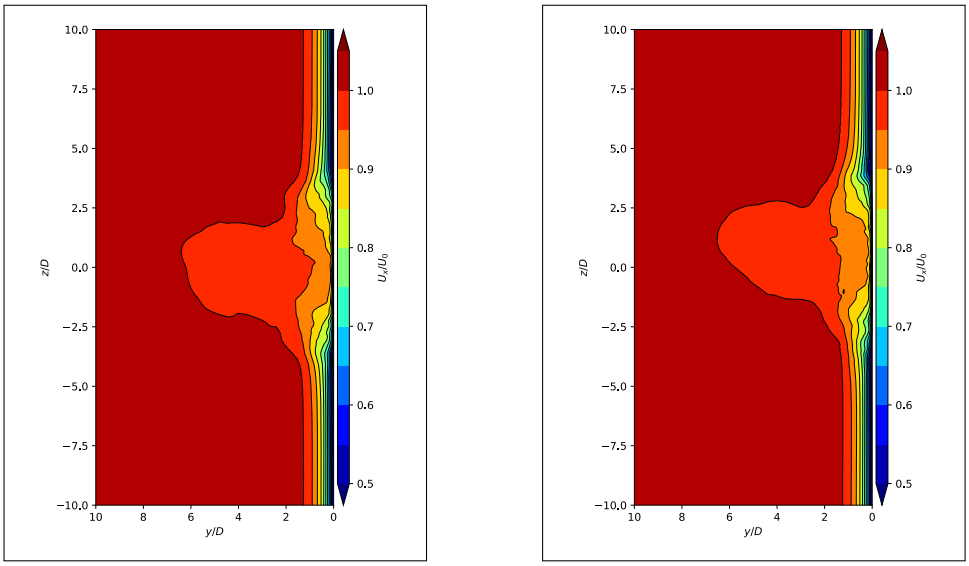

(a) Non-Heated (b) Heated

Figure E.11: Axial Velocity cross plane controus at $X/D = 50$.

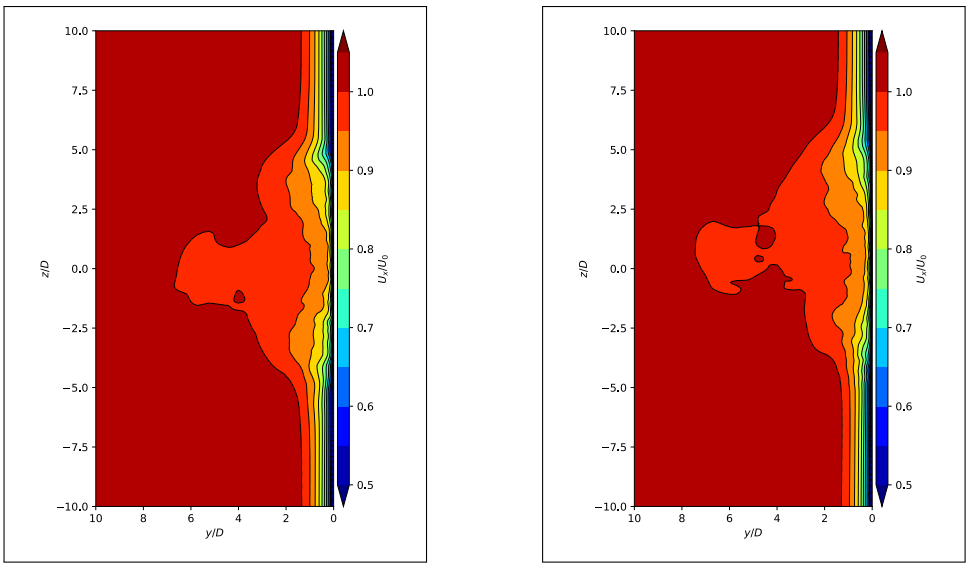

(a) Non-Heated (b) Heated

Figure E.12: Axial Velocity cross plane controus at $X/D = 100$.

E.4.2 Temperature Delta

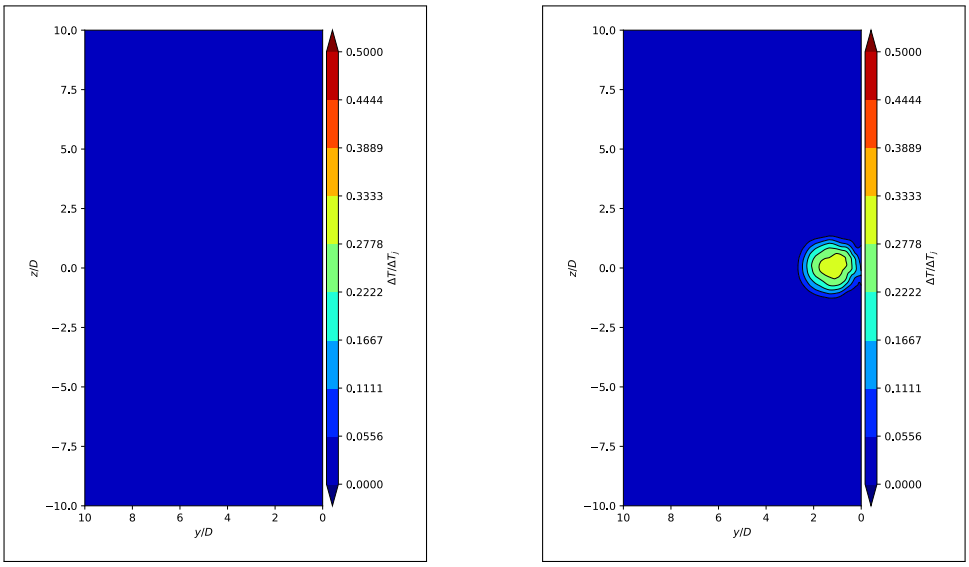

(a) Non-Heated (b) Heated

Figure E.13: Temperature Delta cross plane controus at $X/D = 5$.

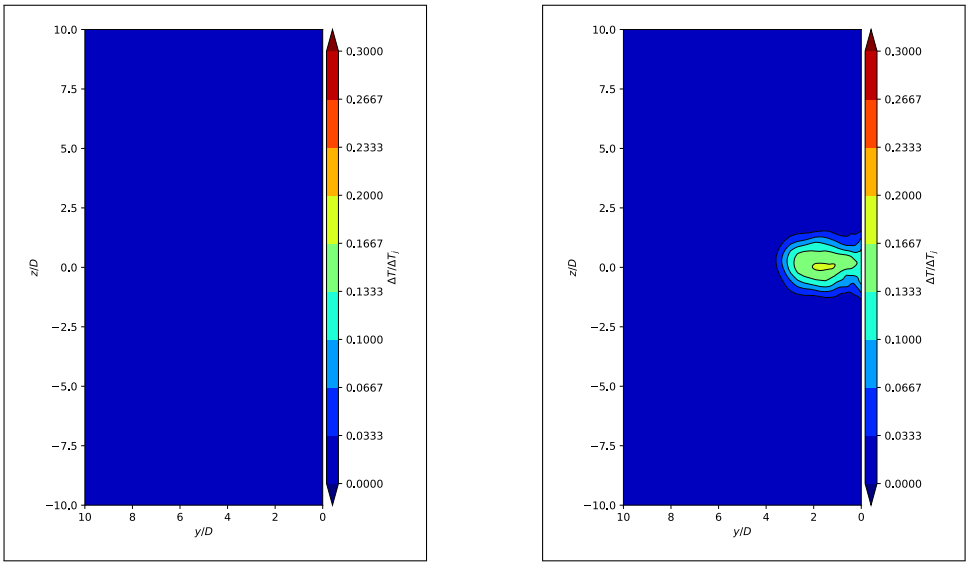

(a) Non-Heated (b) Heated

Figure E.14: Temperature Delta cross plane controus at $X/D = 10$.

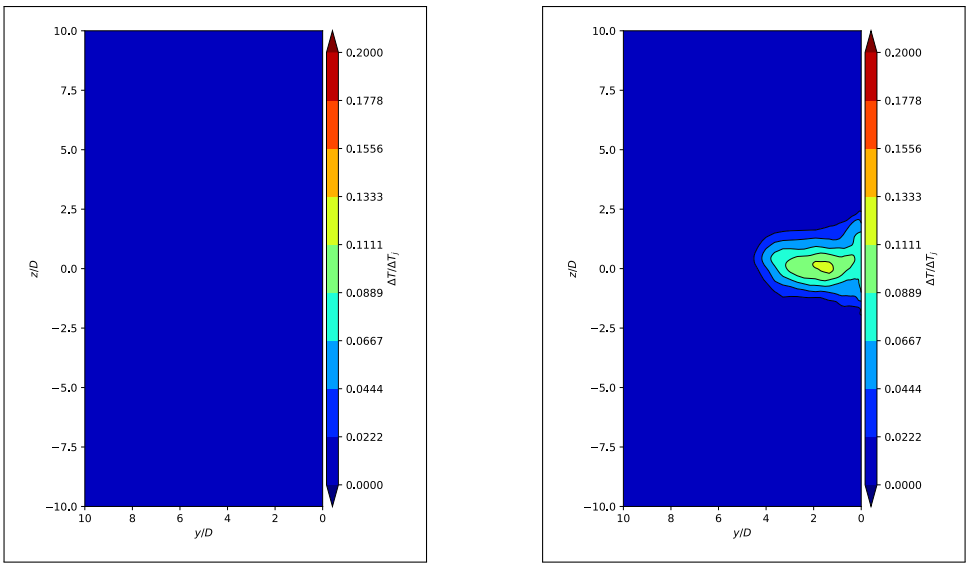

(a) Non-Heated (b) Heated

Figure E.15: Temperature Delta cross plane controus at $X/D = 20$.

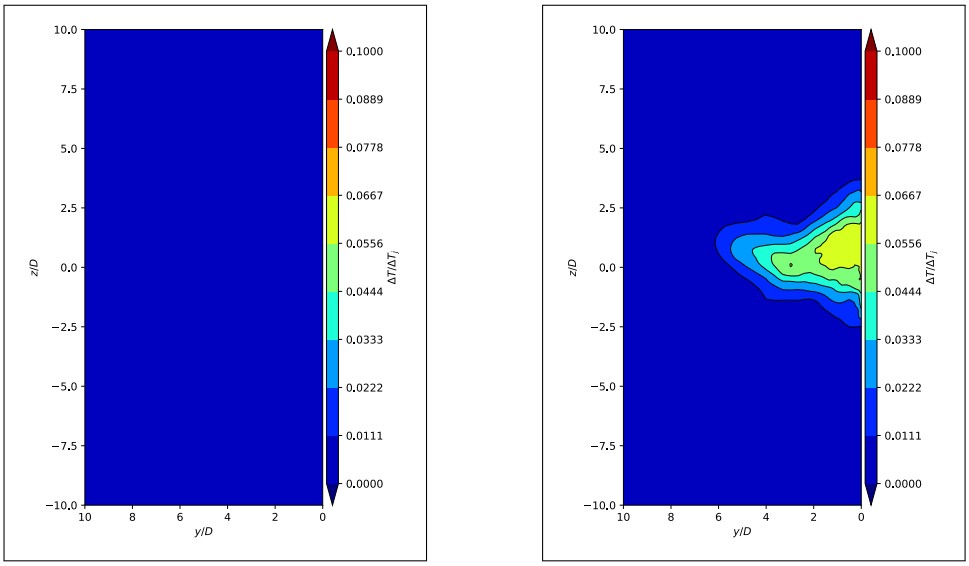

(a) Non-Heated (b) Heated

Figure E.16: Temperature Delta cross plane controus at $X/D = 50$.

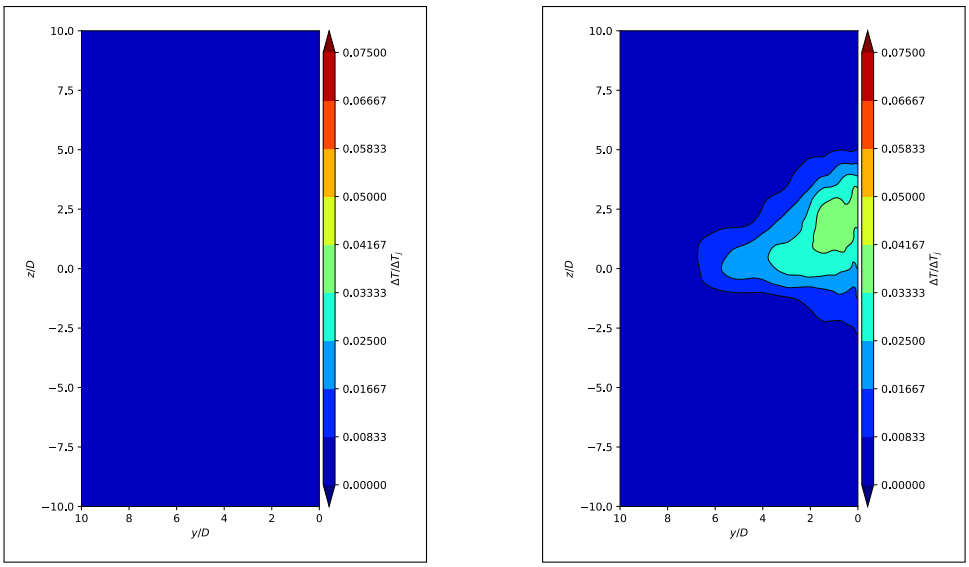

(a) Non-Heated (b) Heated

Figure E.17: Temperature Delta cross plane controus at $X/D = 100$.

Appendix F

JICF Stratification Study

F.1 3D Visualizations

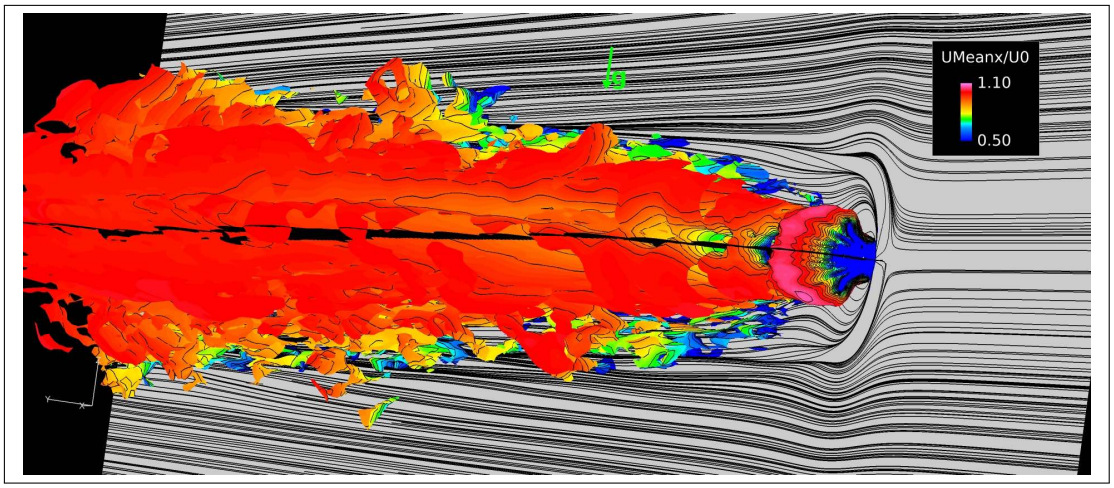

(a) Weak

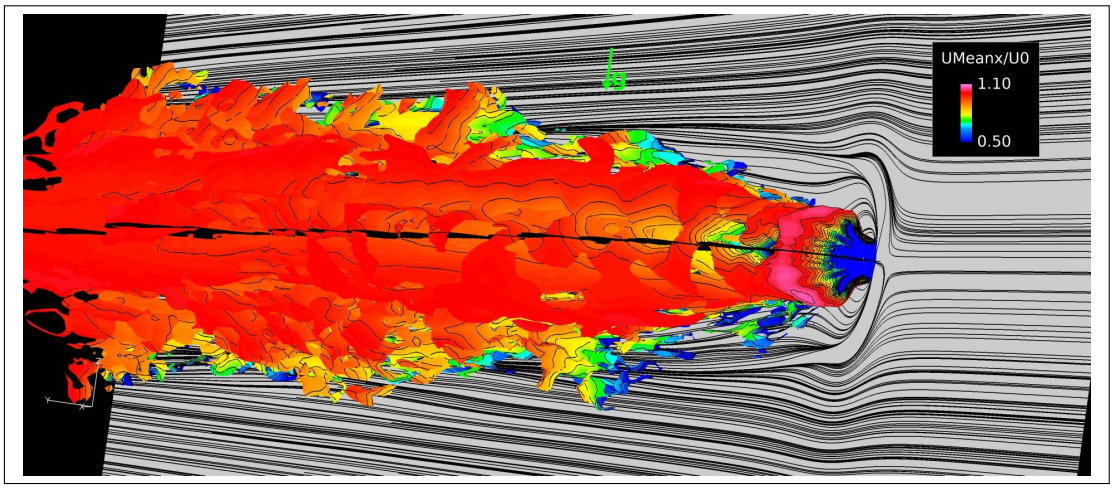

(b) Medium

Figure F.1: Visualization of Q-criterion for $(400D/U_0)^2Q = 0.1$, colored by Axial Velocity.

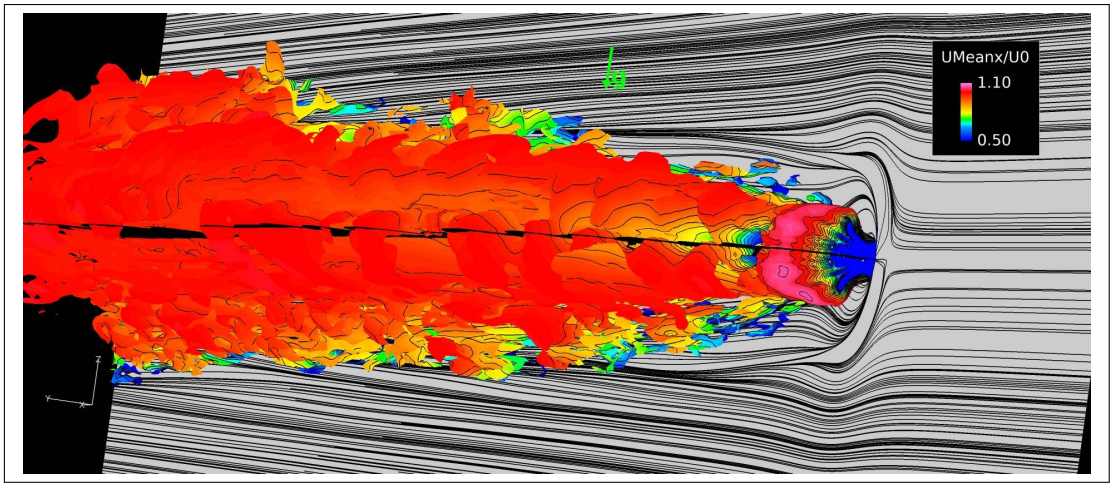

(c) Strong

Figure F.1: Visualization of Q-criterion for $(400D/U_0)^2Q = 0.1$, colored by Axial Velocity.(cont.)

F.2 2D/3D Visualizations

F.2.1 Axial Velocity

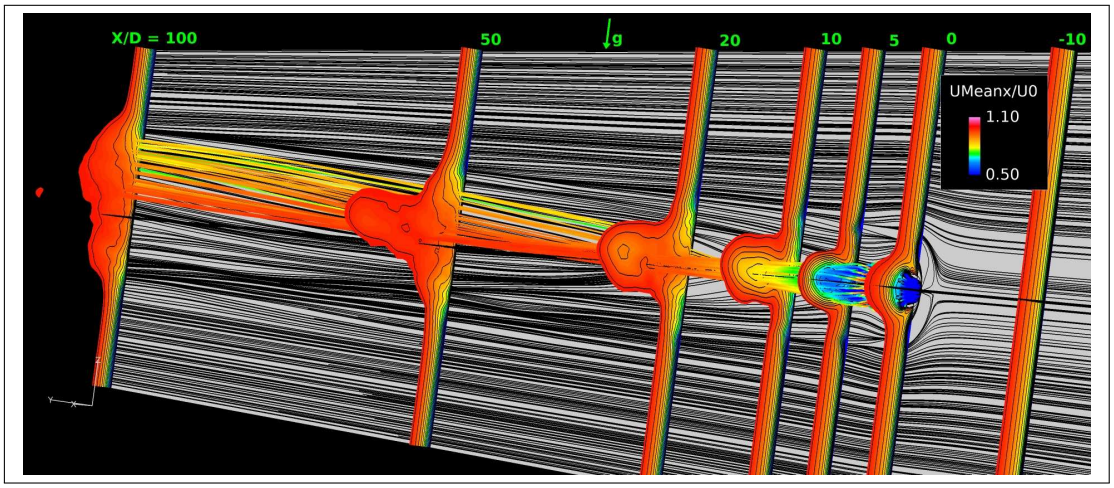

(a) Weak

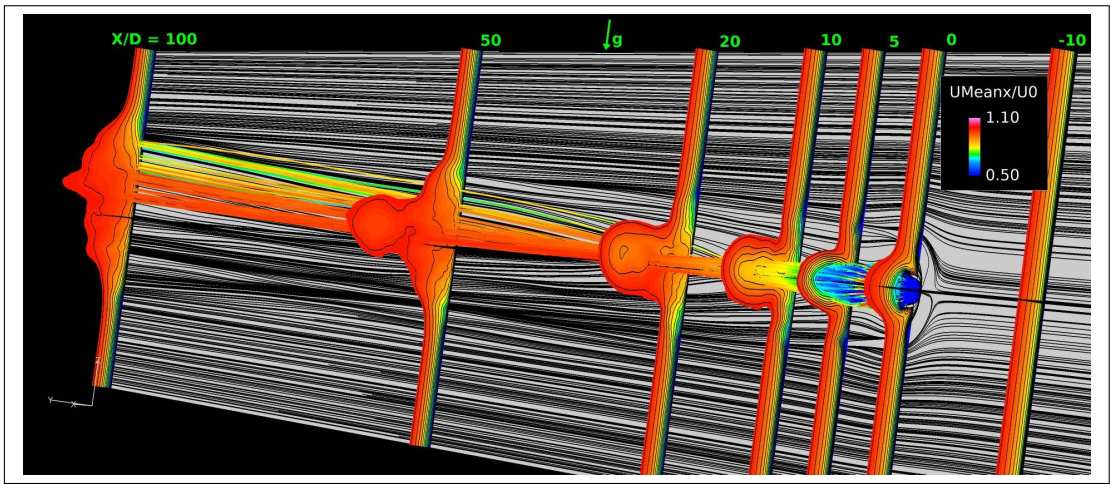

(b) Medium

Figure F.2: Spacial evolution of cross plane contours colored by Axial Velocity, with streamlines emerging from the jet.

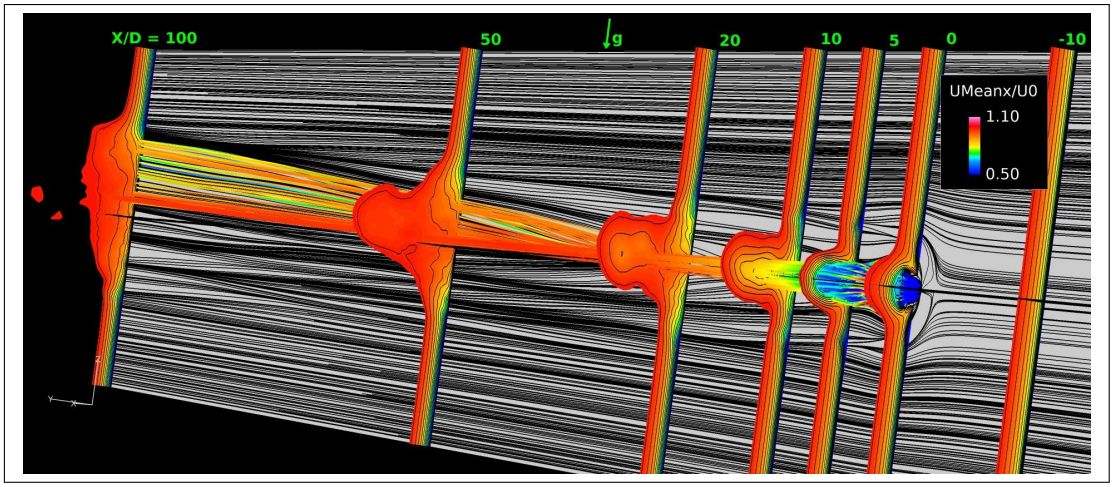

(c) Strong

Figure F.2: Spacial evolution of cross plane contours colored by Axial Velocity, with streamlines emerging from the jet. (cont.)

F.2.2 Temperature Delta

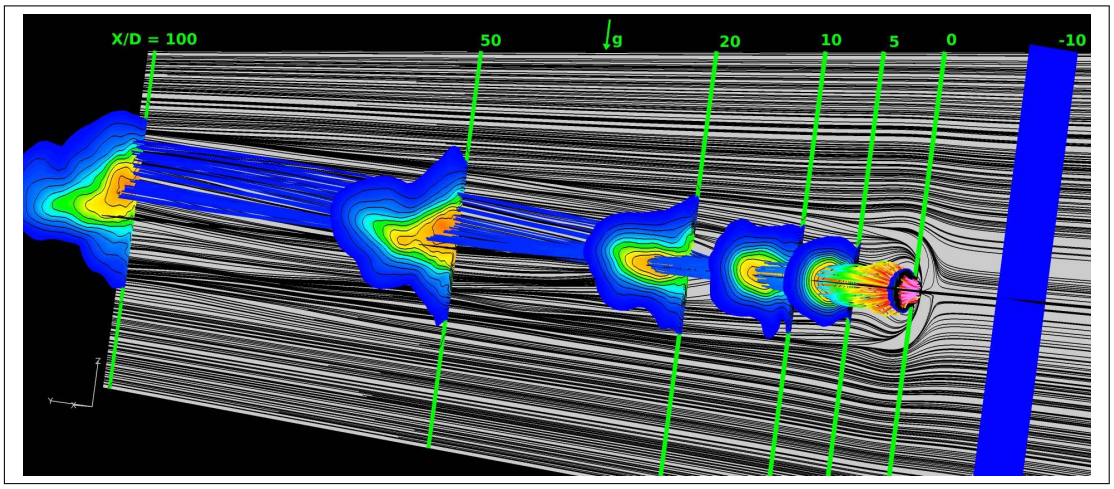

(a) Weak

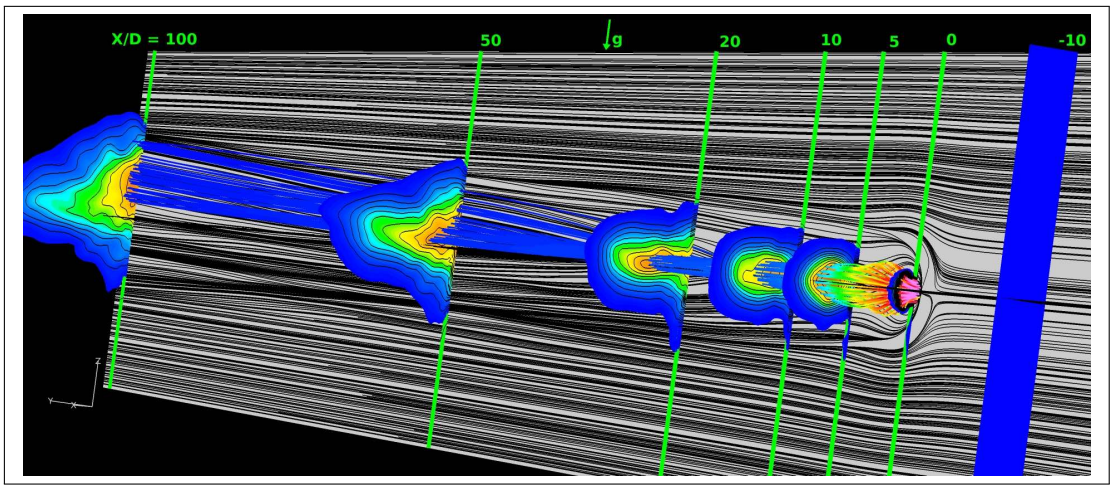

(b) Medium

Figure F.3: Spacial evolution of cross plane contours colored by Temperature Delta, with streamlines emerging from the jet. (Maximum contour value varies with axial location given by the expression, $\Delta T^*_{MAX} = 4/3(X/D)^{-2/3}$)

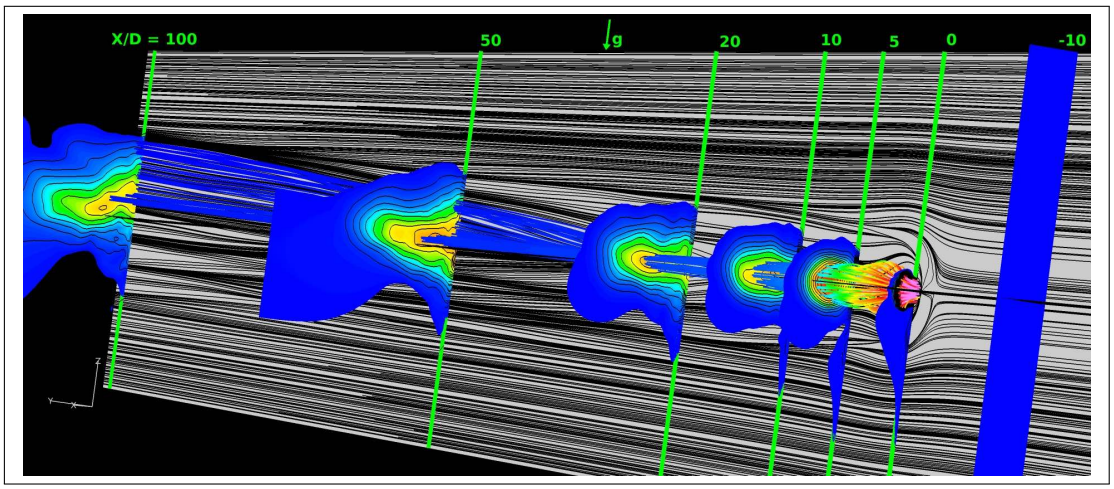

(c) Strong

Figure F.3: Spacial evolution of cross plane contours colored by Temperature Delta, with streamlines emerging from the jet. (Maximum contour value varies with axial location given by the expression, $\Delta T^*_{MAX} = 4/3(X/D)^{-2/3}$)(cont.)

F.3 Data Plots

F.3.1 Boundary Layer Profiles

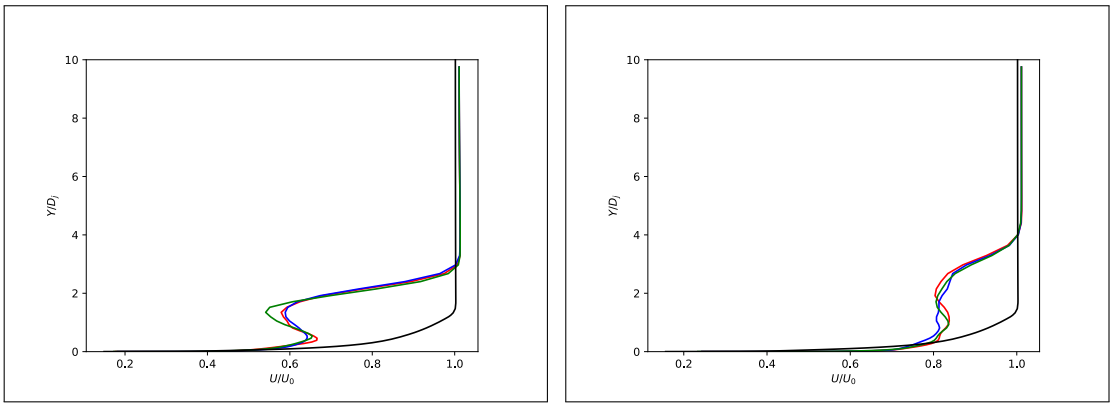

(a) $X/D = 5$ (b) $X/D = 10$

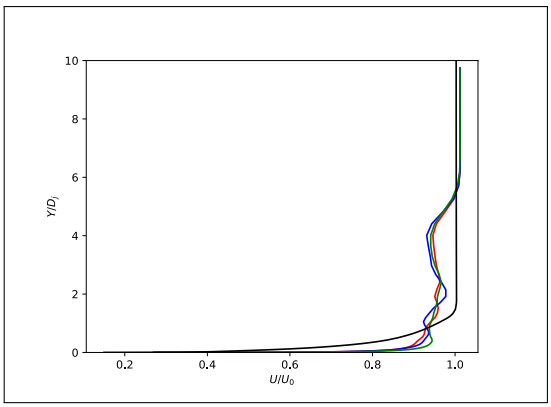

(c) $X/D = 20$

Figure F.4: Axial Velocity plots for the Stratification Study. : Weak, : Medium, : Strong, : No-jet calculation.

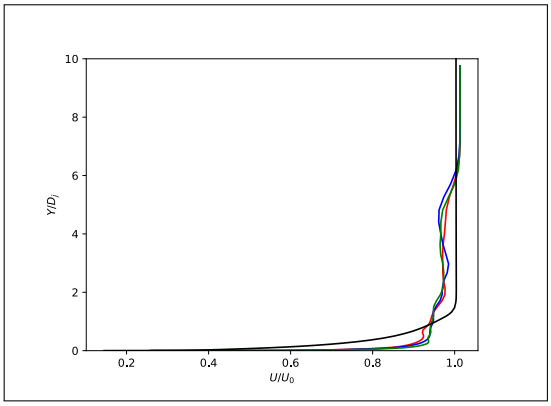

(d) $X/D = 50$

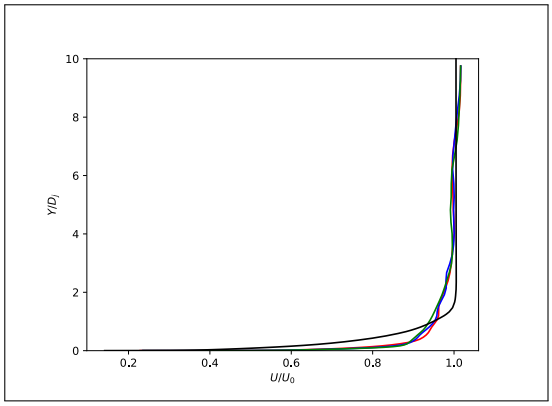

(e) $X/D = 100$

Figure F.4: Axial Velocity plots for the Stratification Study. : Weak, : Medium, : Strong, : No-jet calculation.(cont.)

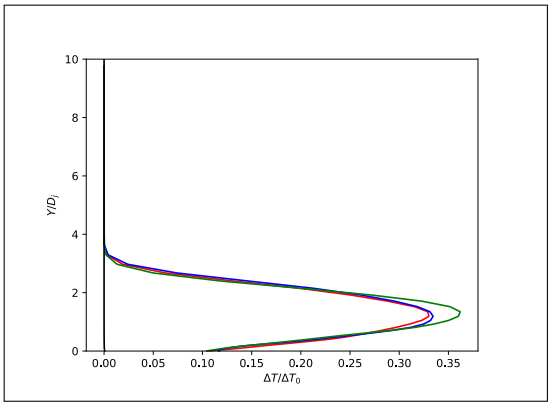

(a) $X/D = 5$

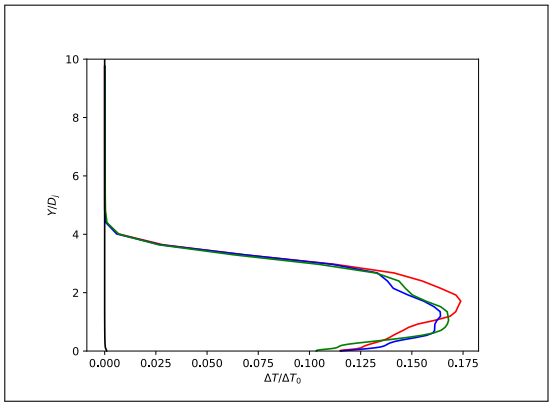

(b) $X/D = 10$

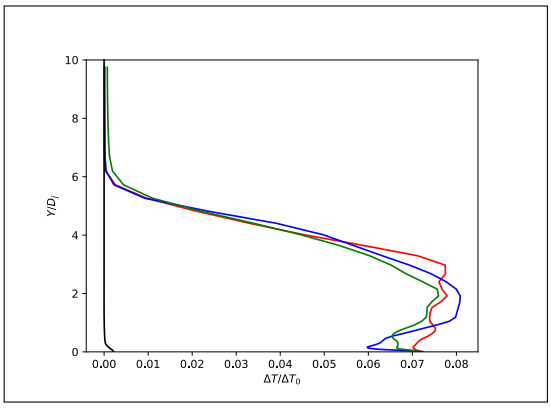

(c) $X/D = 20$

Figure F.5: Temperature Delta plots for the Stratification Study. : Weak, : Medium, : Strong, : No-jet calculation.

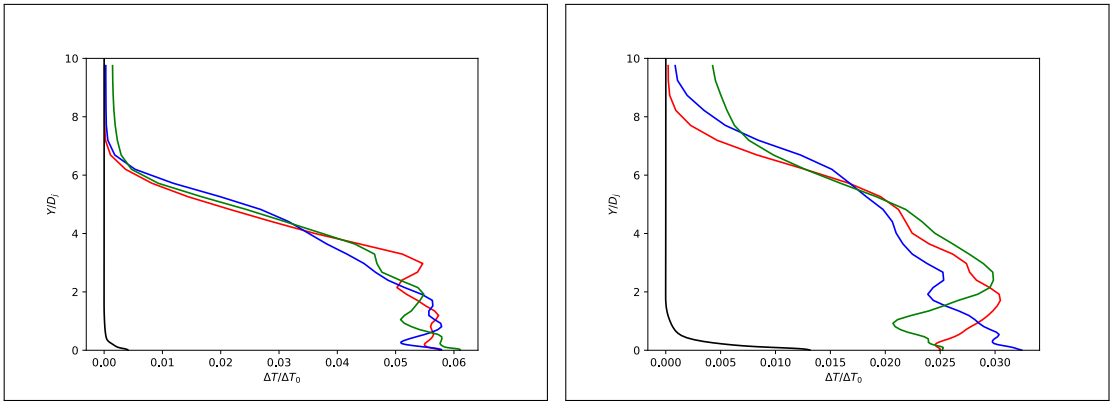

(d) $X/D = 50$ (e) $X/D = 100$

Figure F.5: Temperature Delta plots for the Stratification Study. : Weak, : Medium, : Strong, : No-jet calculation.(cont.)

F.3.2 Wake Plots

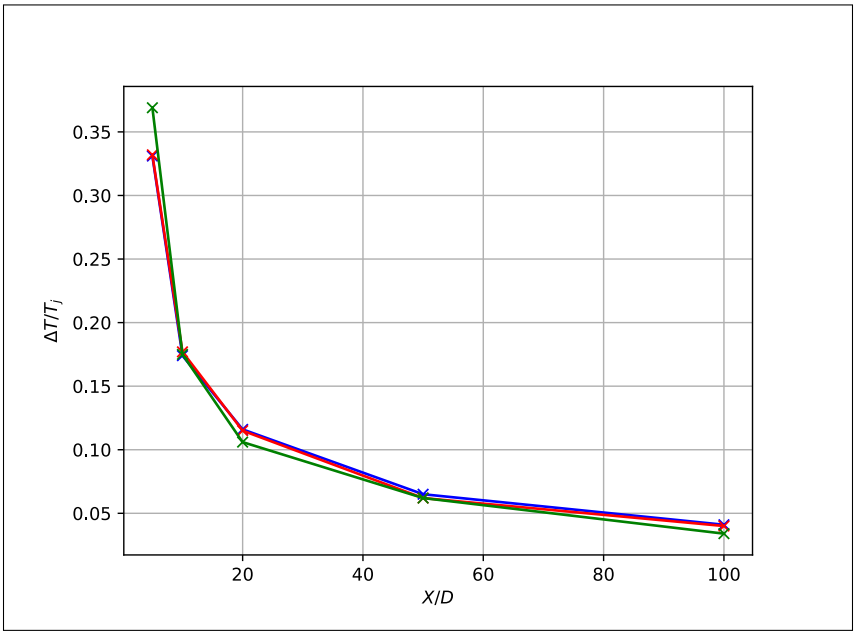

Figure F.6: Centerline Temperature Delta for the Stratification Study. : Weak, : Medium, : Strong.

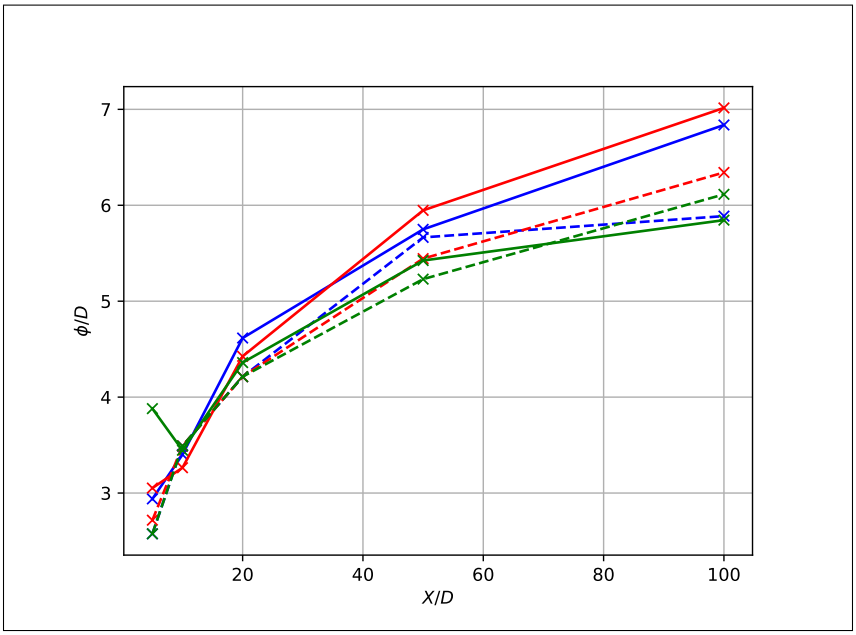

Figure F.7: Wake Height (Dashed) and Width (Solid) for the Stratification Study. : Weak, : Medium, : Strong.

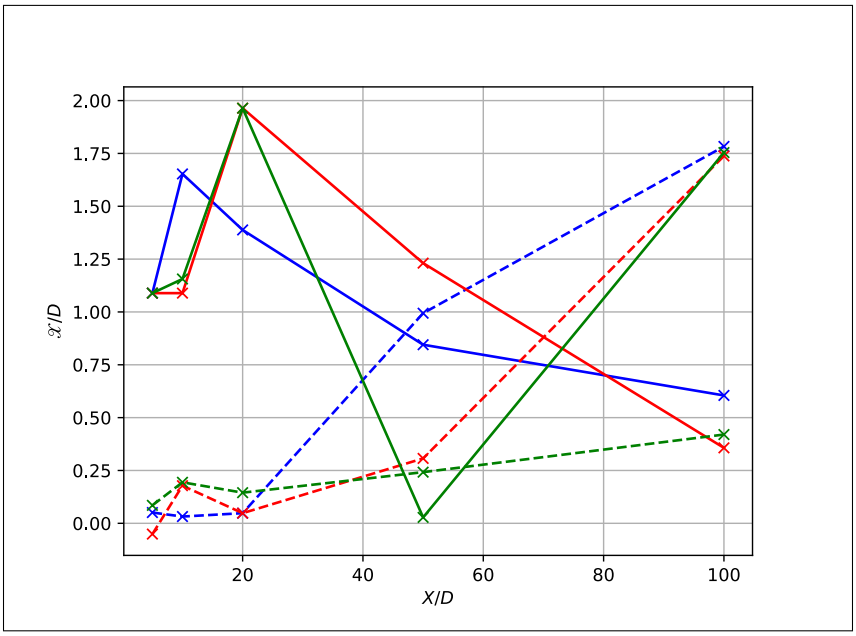

Figure F.8: Centerline Wake Vertical (Dashed) and Horizontal (Solid) position for the Stratification Study. : Weak, : Medium, : Strong.

F.4 Cross Plane Contours

F.4.1 Axial Velocity

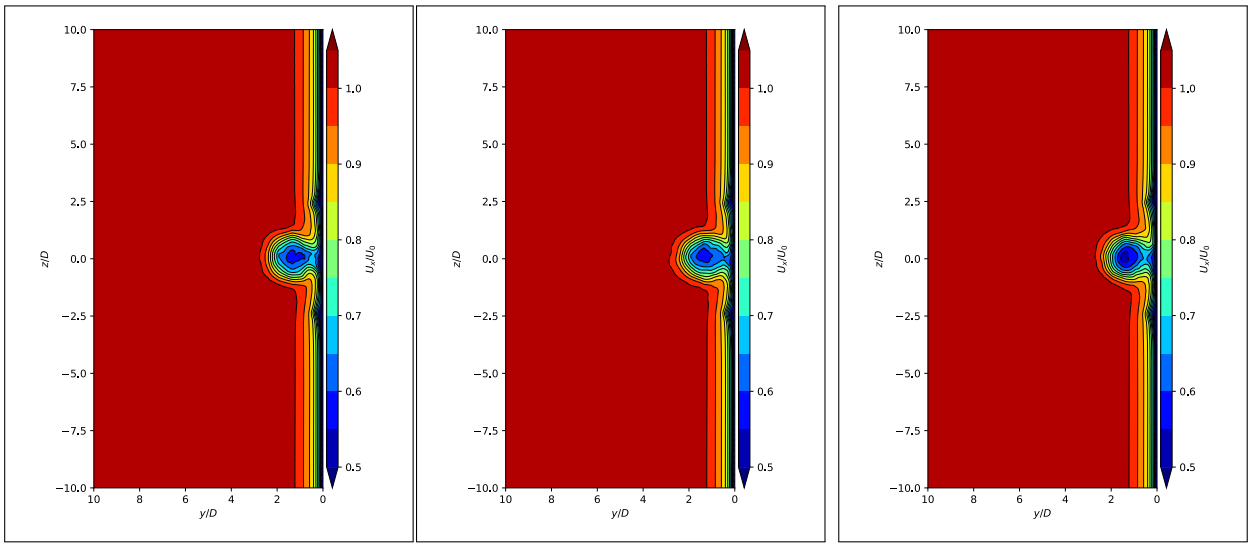

(a) Weak (b) Medium (c) Strong

Figure F.9: Axial Velocity cross plane controus at $X/D = 5$.

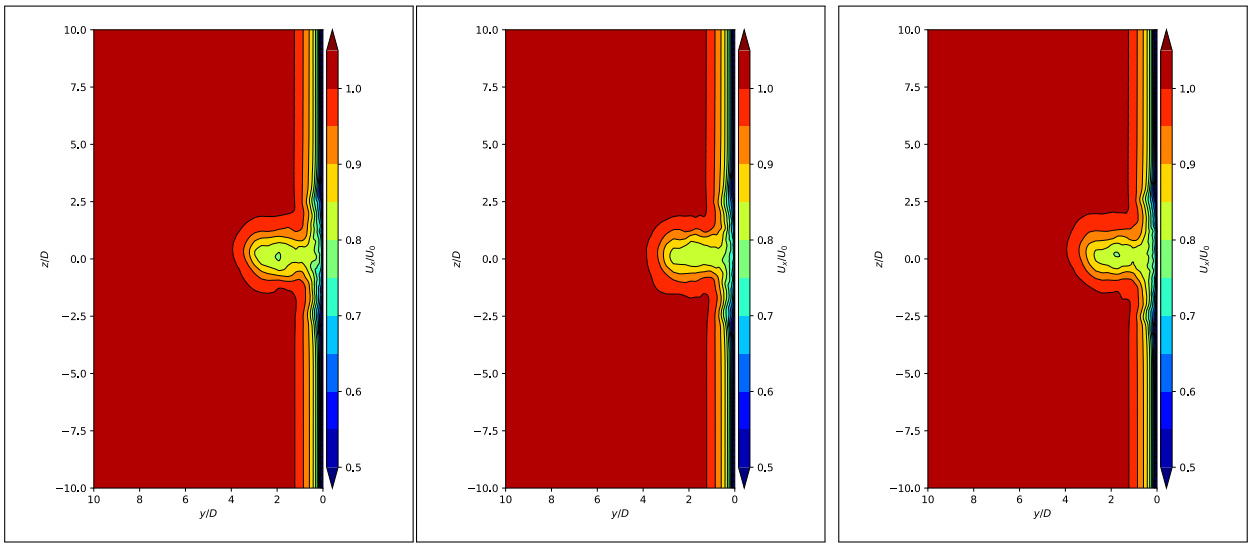

(a) Weak (b) Medium (c) Strong

Figure F.10: Axial Velocity cross plane controus at $X/D = 10$.

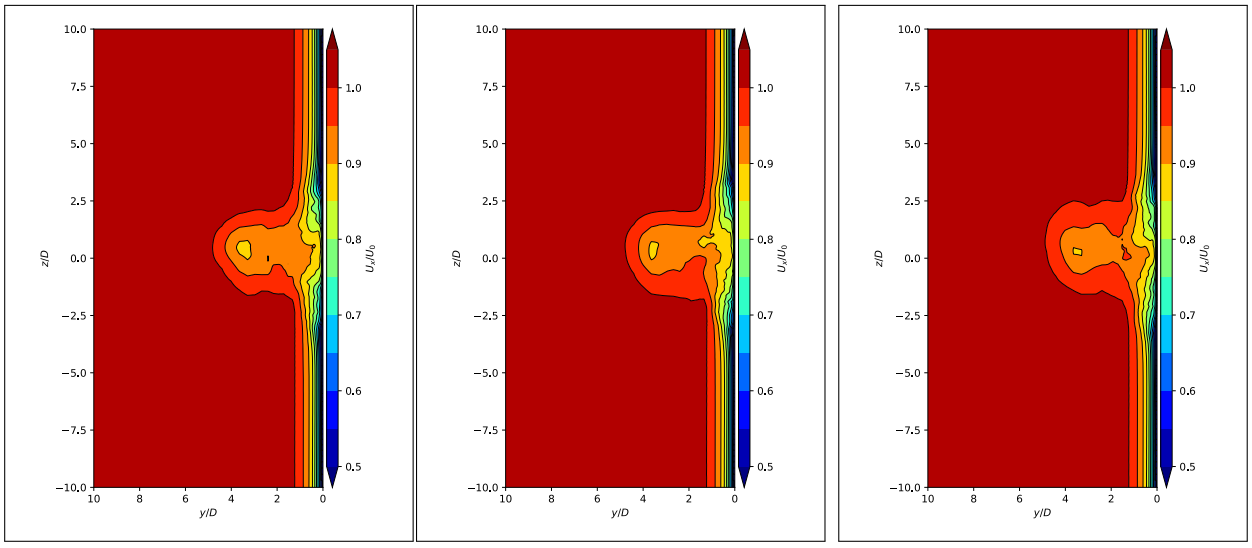

(a) Weak (b) Medium (c) Strong

Figure F.11: Axial Velocity cross plane controus at $X/D = 20$.

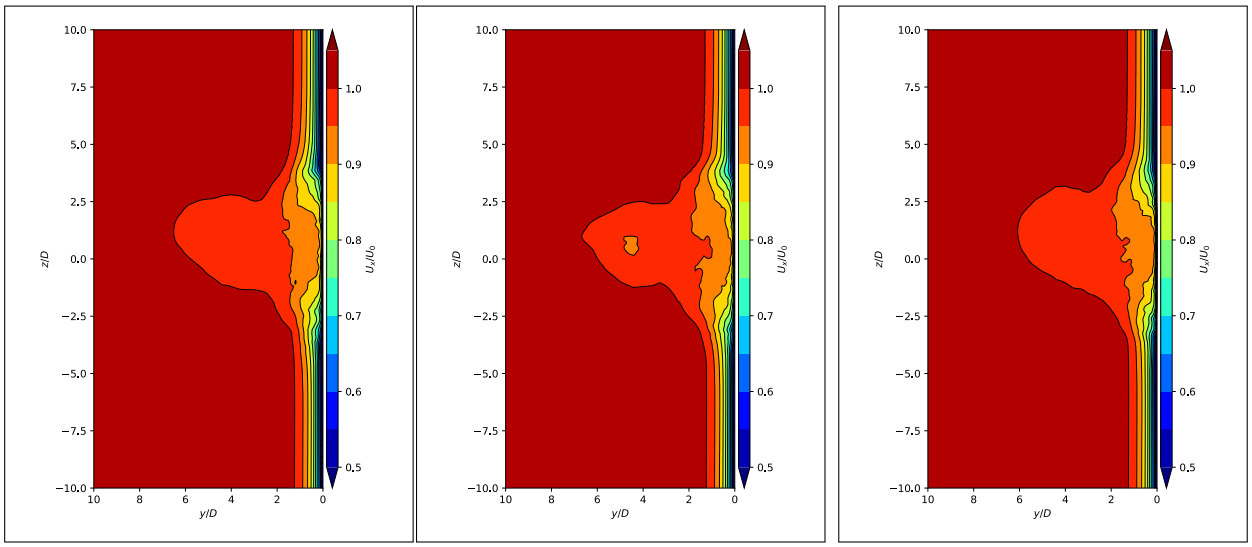

(a) Weak (b) Medium (c) Strong

Figure F.12: Axial Velocity cross plane controus at $X/D = 50$.

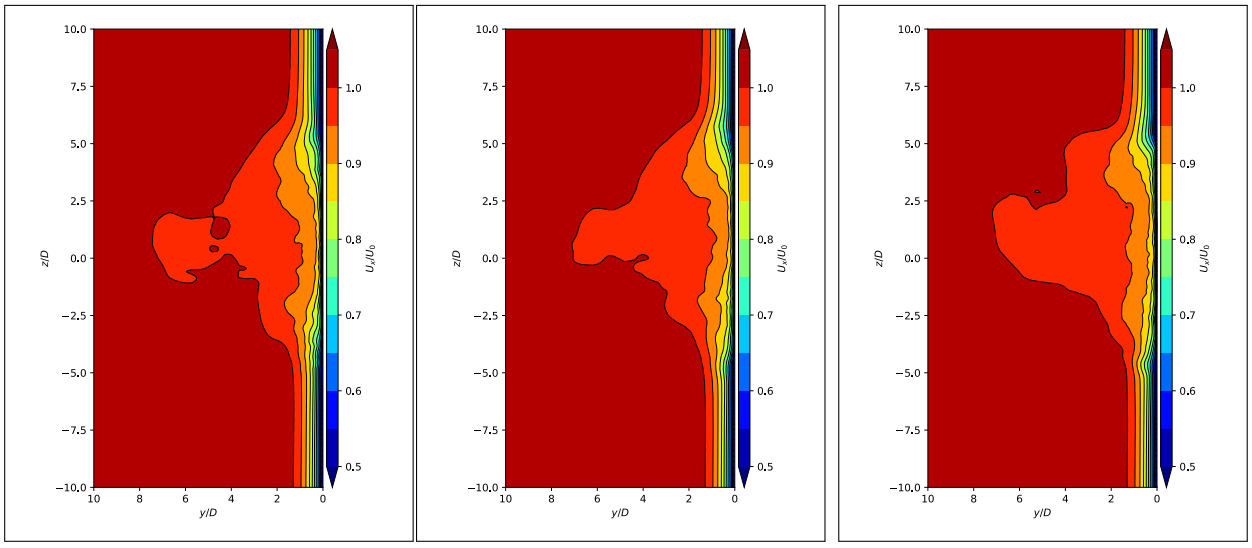

(a) Weak (b) Medium (c) Strong

Figure F.13: Axial Velocity cross plane controus at $X/D = 100$.

F.4.2 Temperature Delta

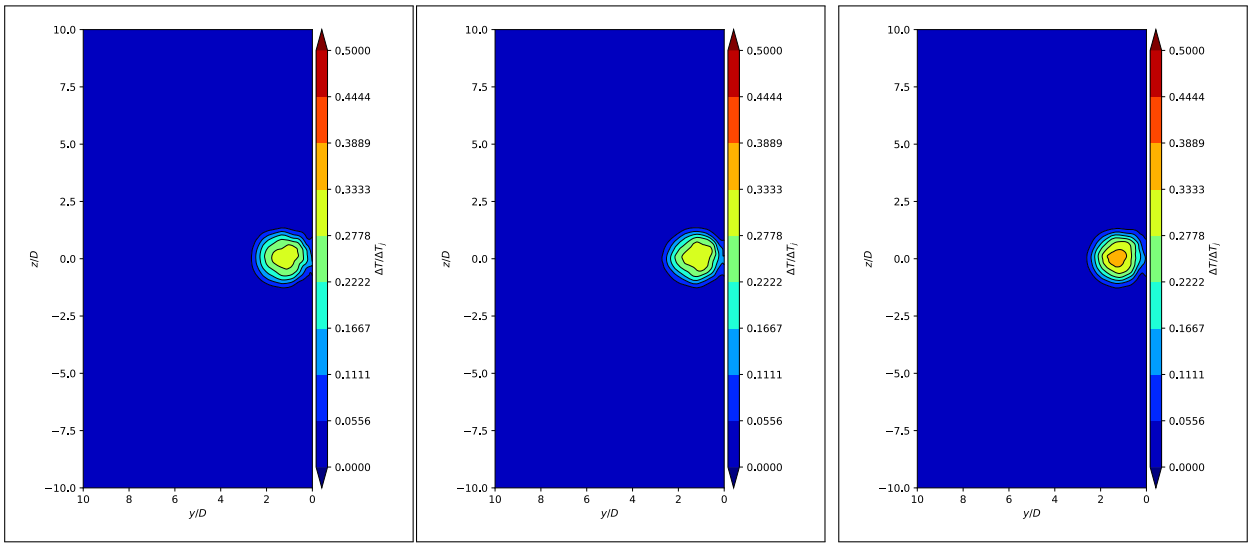

(a) Weak (b) Medium (c) Strong

Figure F.14: Temperature Delta cross plane controus at $X/D = 5$.

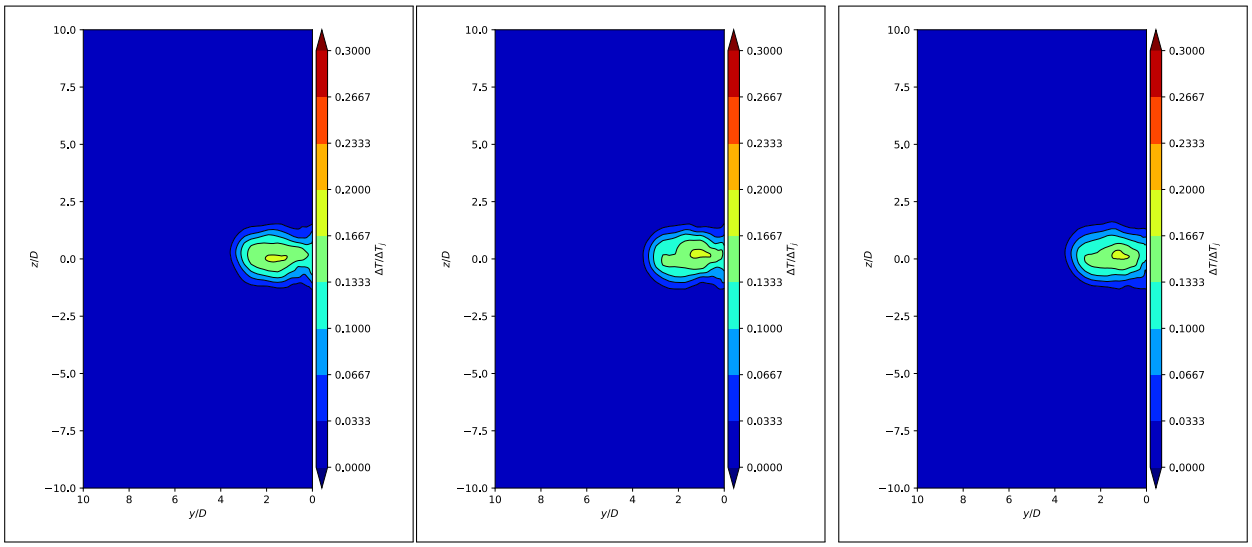

(a) Weak (b) Medium (c) Strong

Figure F.15: Temperature Delta cross plane controus at $X/D = 10$.

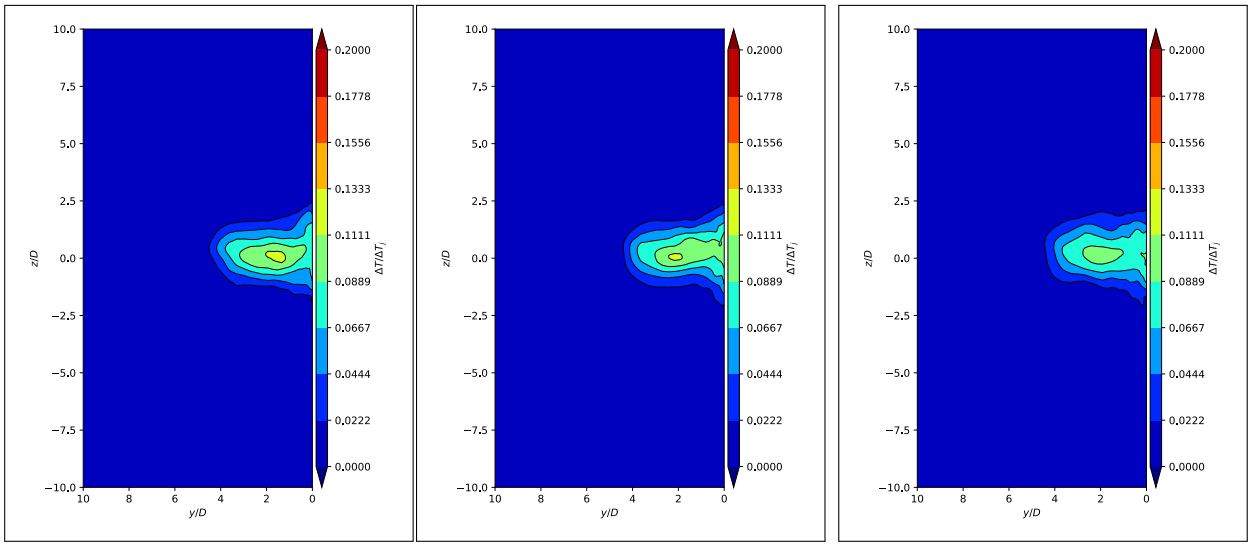

(a) Weak (b) Medium (c) Strong

Figure F.16: Temperature Delta cross plane controus at $X/D = 20$.

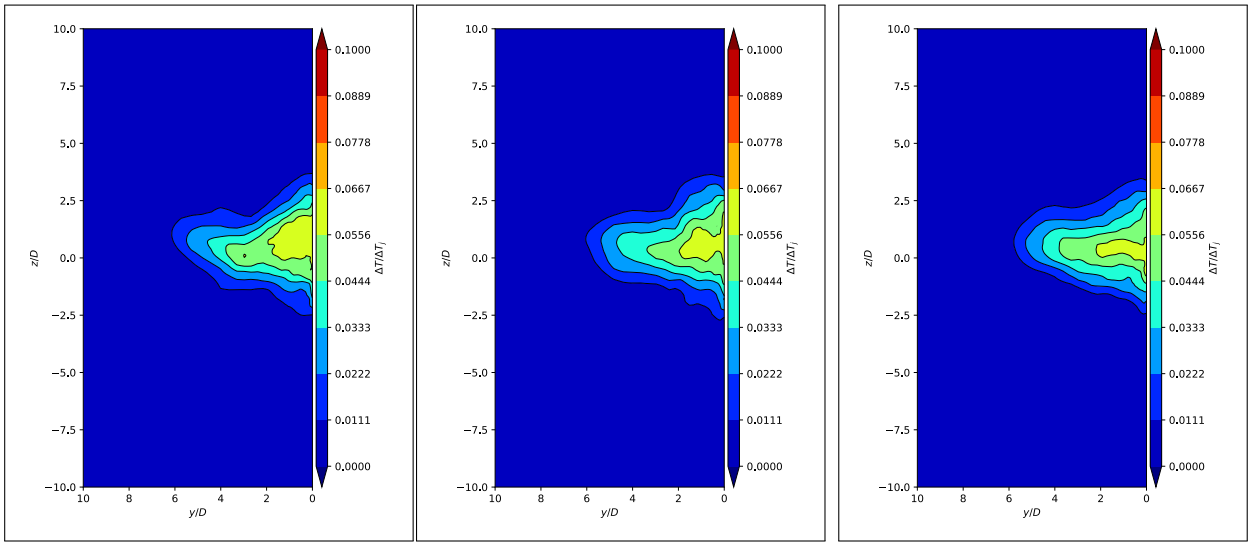

(a) Weak (b) Medium (c) Strong

Figure F.17: Temperature Delta cross plane controus at $X/D = 50$.

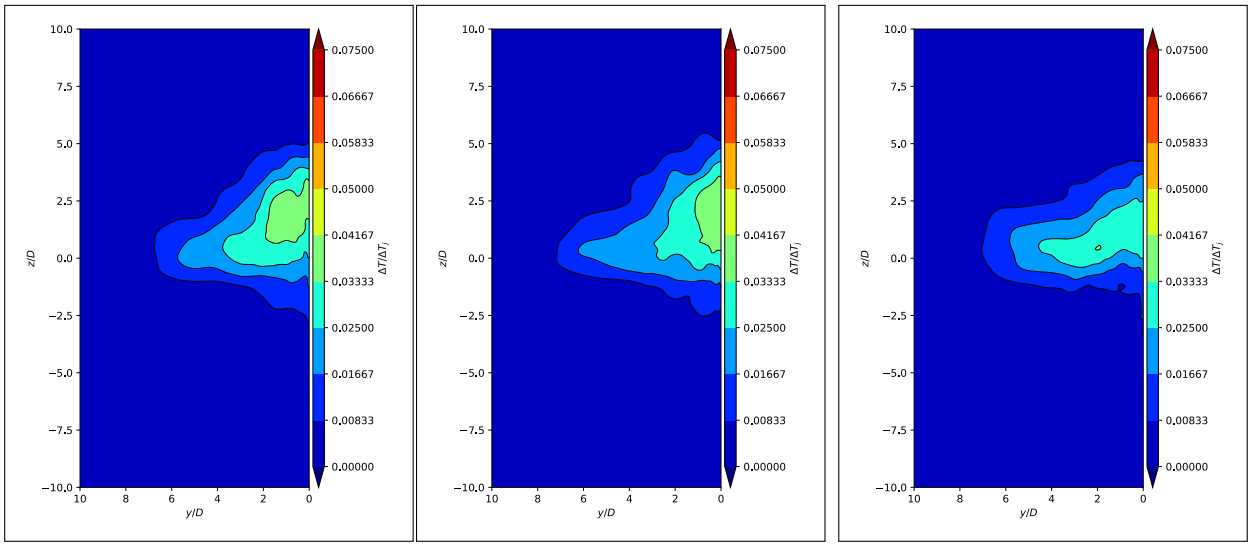

(a) Weak (b) Medium (c) Strong

Figure F.18: Temperature Delta cross plane controus at $X/D = 100$.

Appendix G

JICF Velocity Ratio Study

G.1 3D Visualizations

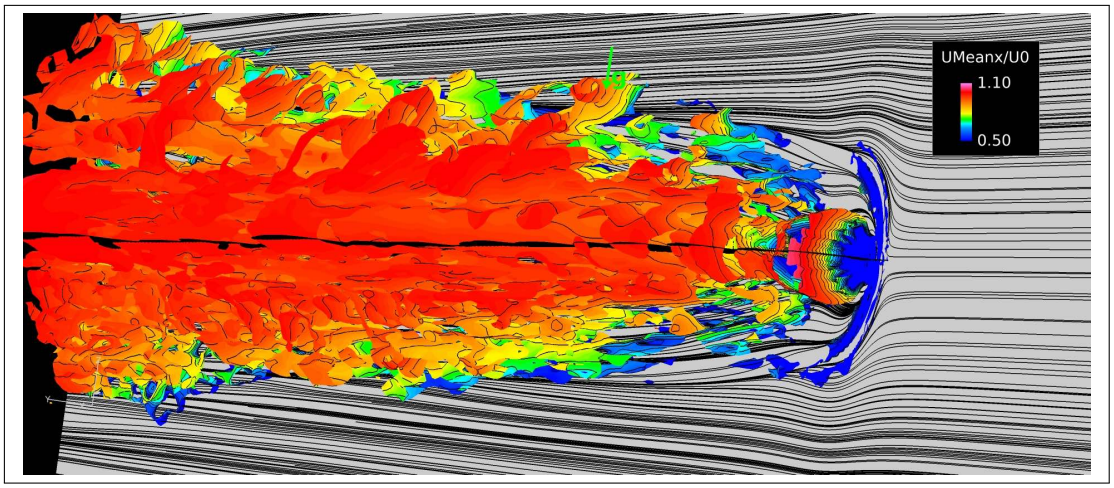

(a) $r = 0.5$

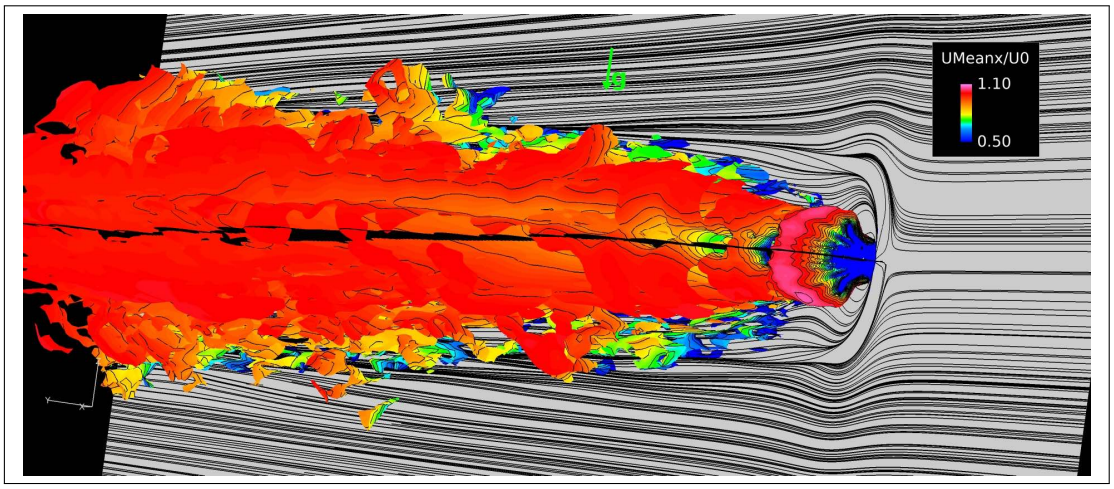

(b) $r = 1.0$

Figure G.1: Visualization of Q-criterion for $(400D/U_0)^2Q = 0.1$, colored by Axial Velocity.

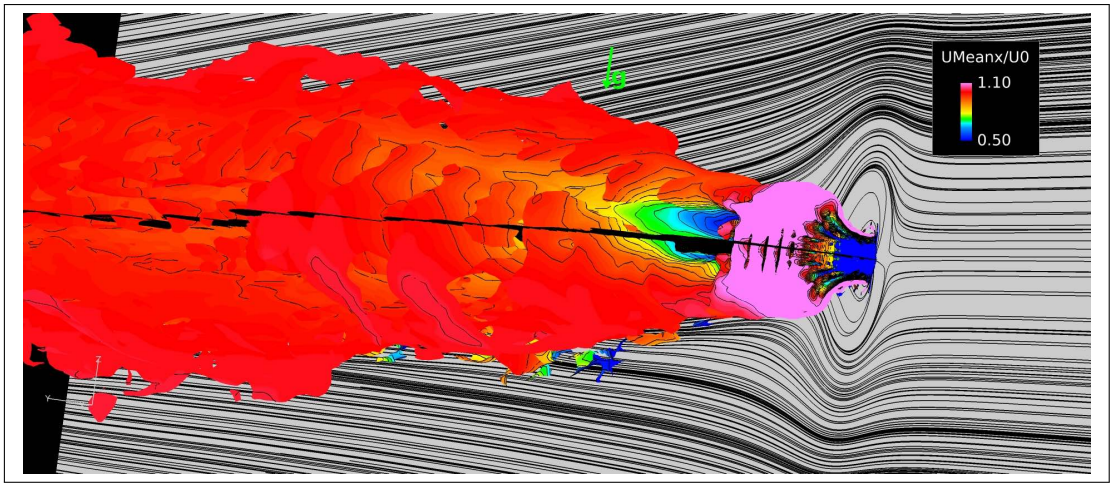

(c) $r = 2.0$

Figure G.1: Visualization of Q-criterion for $(400D/U_0)^2Q = 0.1$, colored by Axial Velocity.(cont.)

G.2 2D/3D Visualizations

G.2.1 Axial Velocity

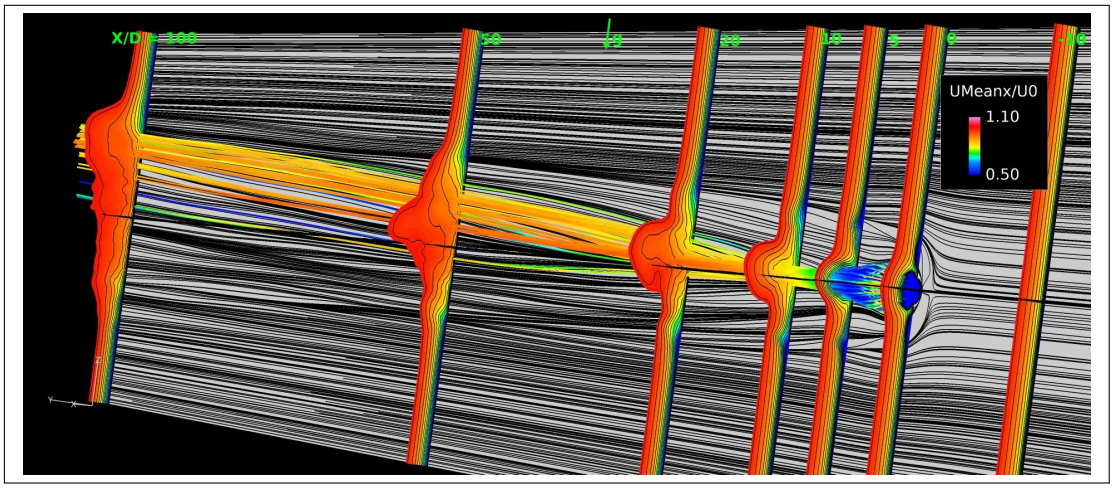

(a) $r = 0.5$

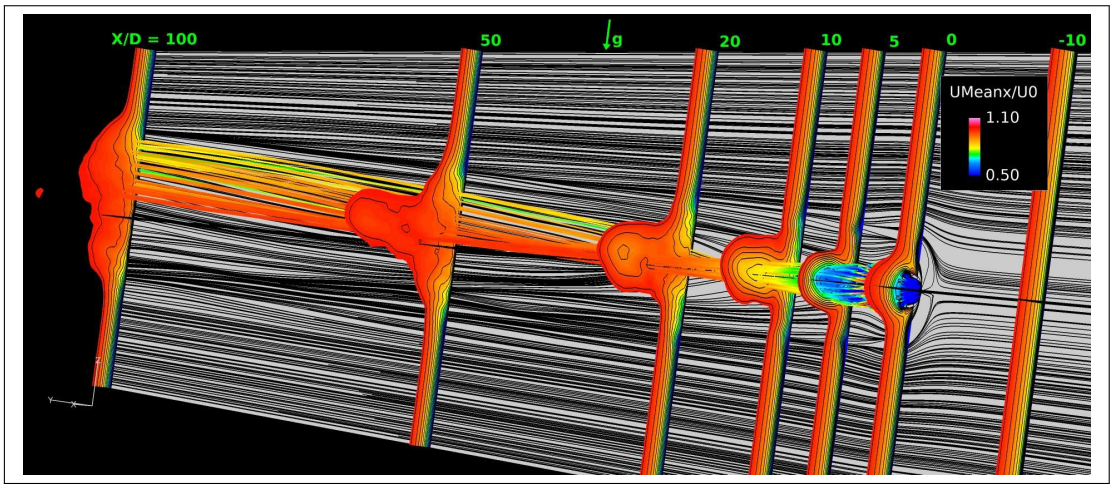

(b) $r = 1.0$

Figure G.2: Spacial evolution of cross plane contours colored by Axial Velocity, with streamlines emerging from the jet.

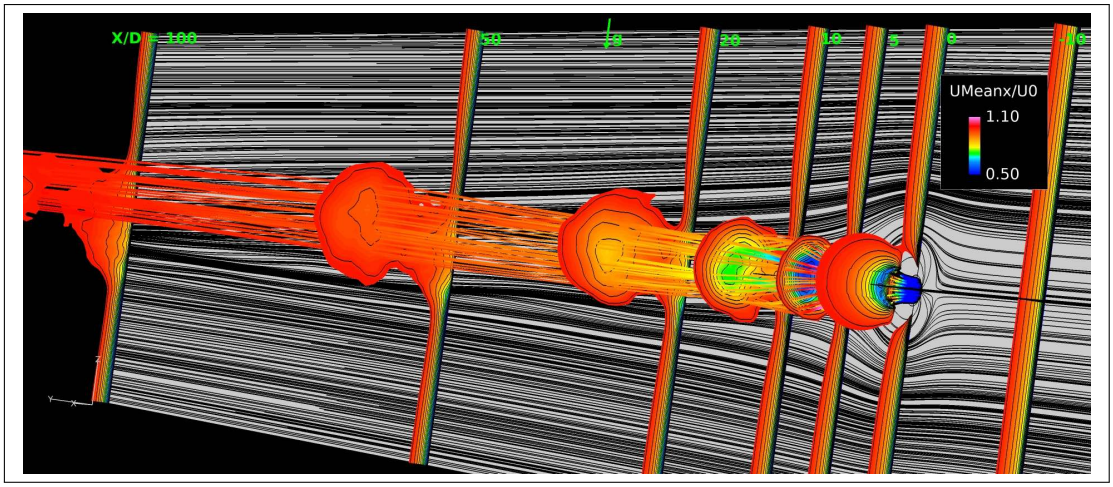

(c) $r = 2.0$

Figure G.2: Spacial evolution of cross plane contours colored by Axial Velocity, with streamlines emerging from the jet. (cont.)

G.2.2 Temperature Delta

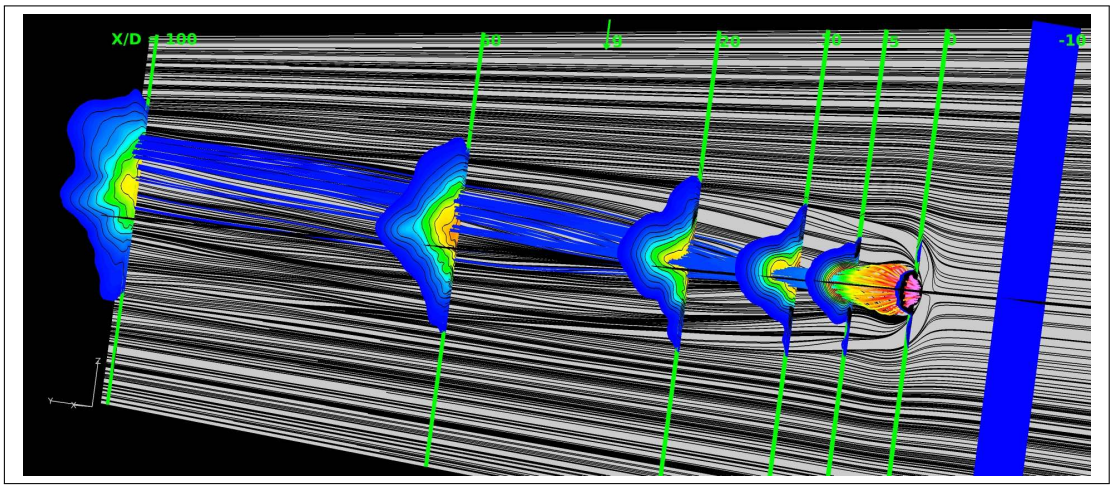

(a) $r = 0.5$

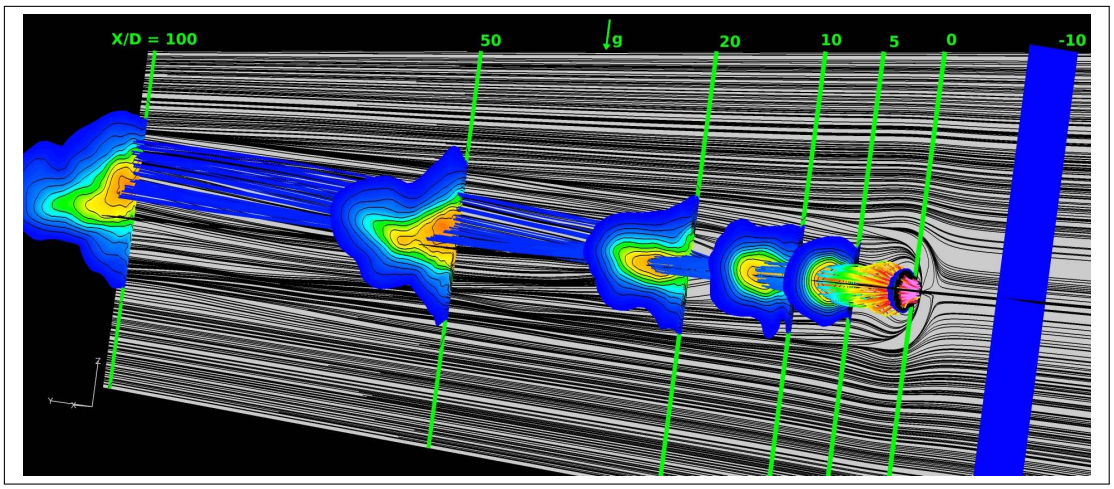

(b) $r = 1.0$

Figure G.3: Spacial evolution of cross plane contours colored by Temperature Delta, with streamlines emerging from the jet. (Maximum contour value varies with axial location given by the expression, $\Delta T^*_{MAX} = 4/3(X/D)^{-2/3}$)

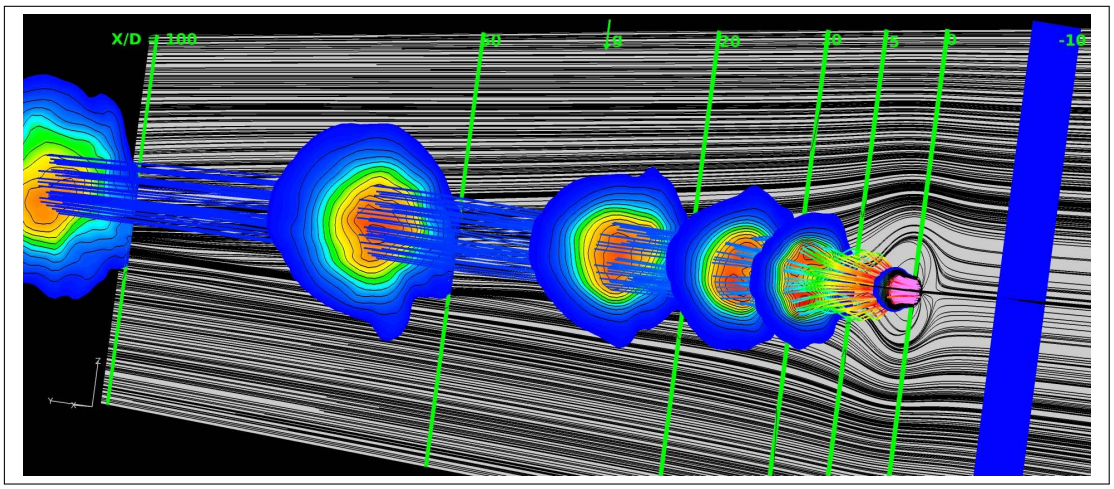

(c) $r = 2.0$

Figure G.3: Spacial evolution of cross plane contours colored by Temperature Delta, with streamlines emerging from the jet. (Maximum contour value varies with axial location given by the expression, $\Delta T^*_{MAX} = 4/3(X/D)^{-2/3}$)(cont.)

G.3 Data Plots

G.3.1 Boundary Layer Profiles

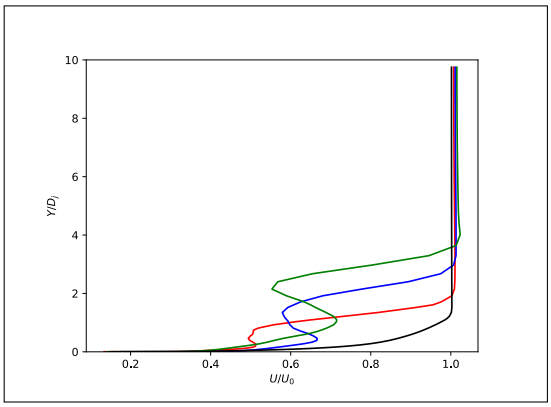

(a) $X/D = 5$

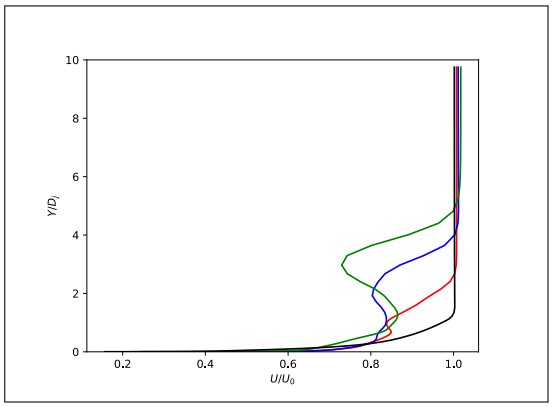

(b) $X/D = 10$

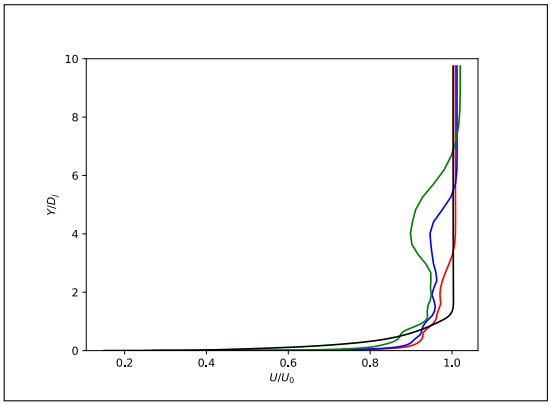

(c) $X/D = 20$

Figure G.4: Axial Velocity plots for the Velocity Ratio Study. : $r = 0.5$, : $r = 1.0$, : $r = 2.0$, : No-jet calculation.

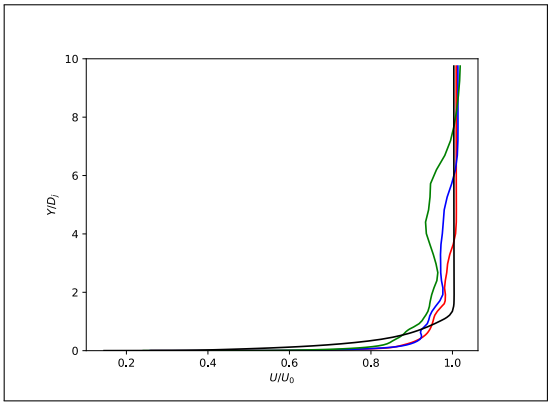

(d) $X/D = 50$

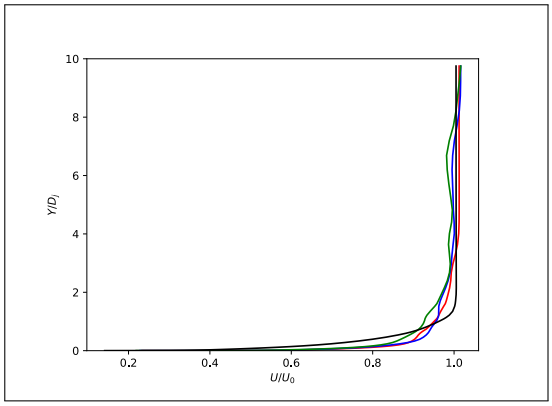

(e) $X/D = 100$

Figure G.4: Axial Velocity plots for the Velocity Ratio Study. : $r = 0.5$, : $r = 1.0$, : $r = 2.0$, : No-jet calculation. (cont.)

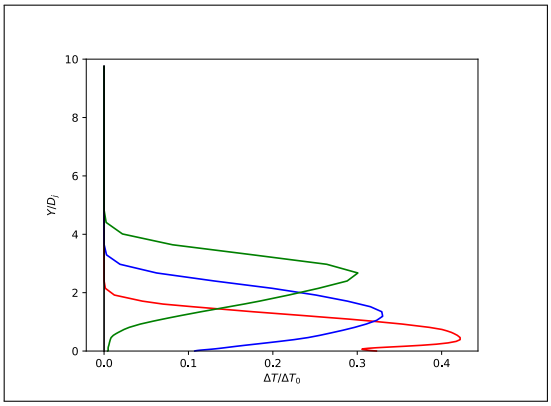

(a) $X/D = 5$

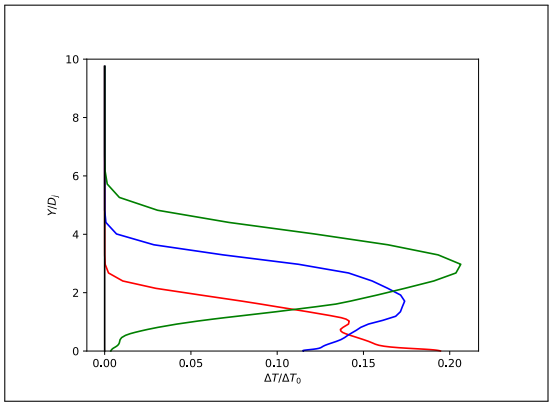

(b) $X/D = 10$

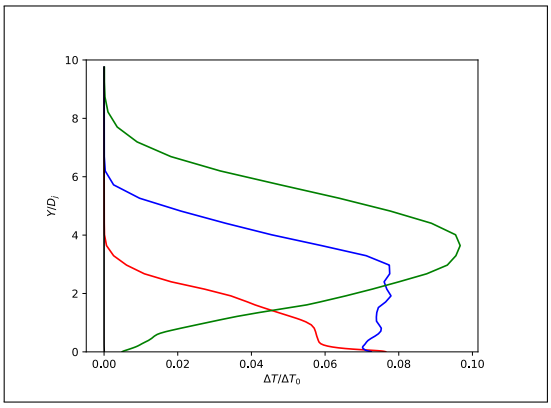

(c) $X/D = 20$

Figure G.5: Temperature Delta plots for the Velocity Ratio Study. : $r = 0.5$, : $r = 1.0$, : $r = 2.0$, : No-jet calculation.

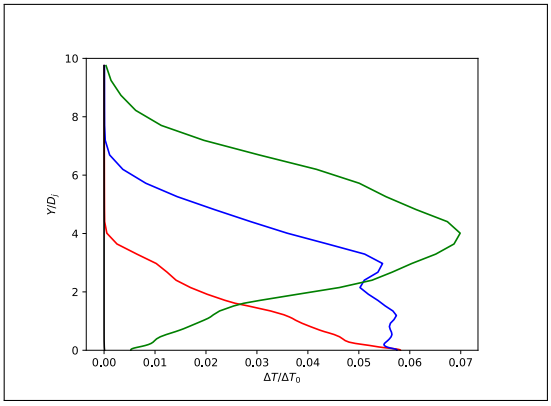

(d) $X/D = 50$

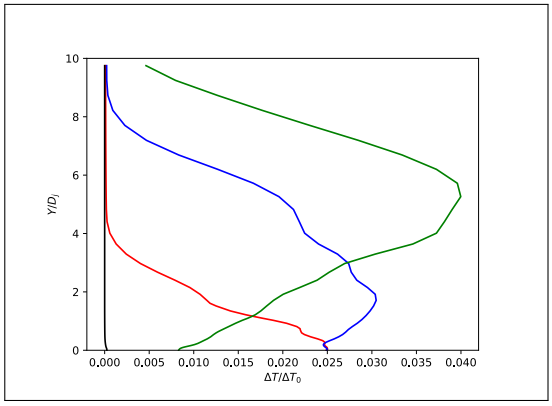

(e) $X/D = 100$

Figure G.5: Temperature Delta plots for the Velocity Ratio Study. : $r = 0.5$, : $r = 1.0$, : $r = 2.0$, : No-jet calculation.(cont.)

G.3.2 Wake Plots

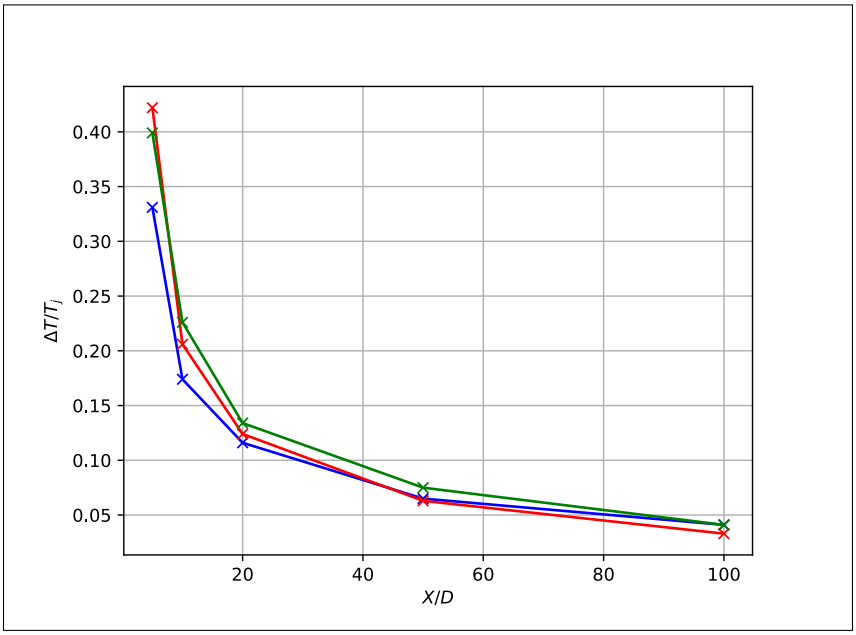

Figure G.6: Centerline Temperature Delta for the Velocity Ratio Study. : $r = 0.5$, : $r = 1.0$, : $r = 2.0$.

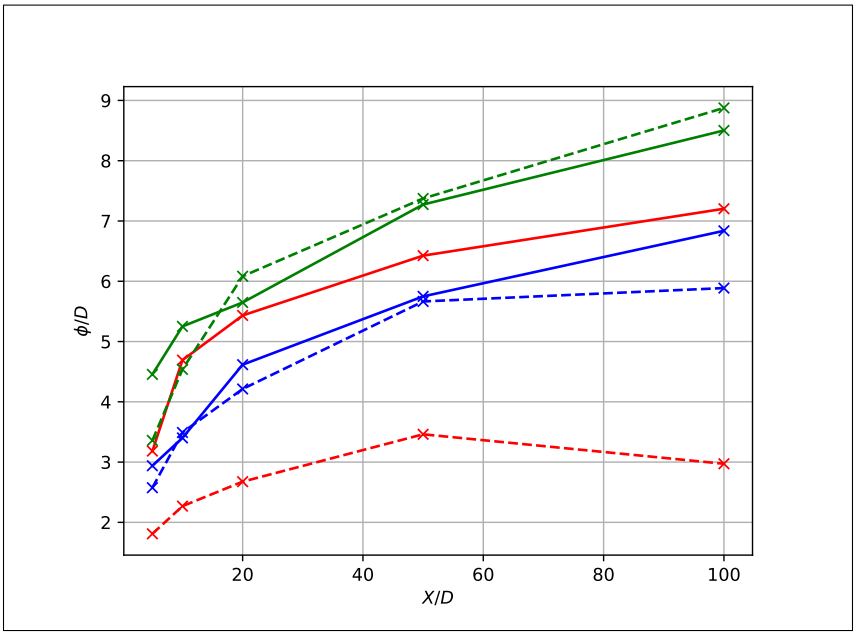

Figure G.7: Wake Height (Dashed) and Width (Solid) for the Velocity Ratio Study. : $r = 0.5$, : $r = 1.0$, : $r = 2.0$.

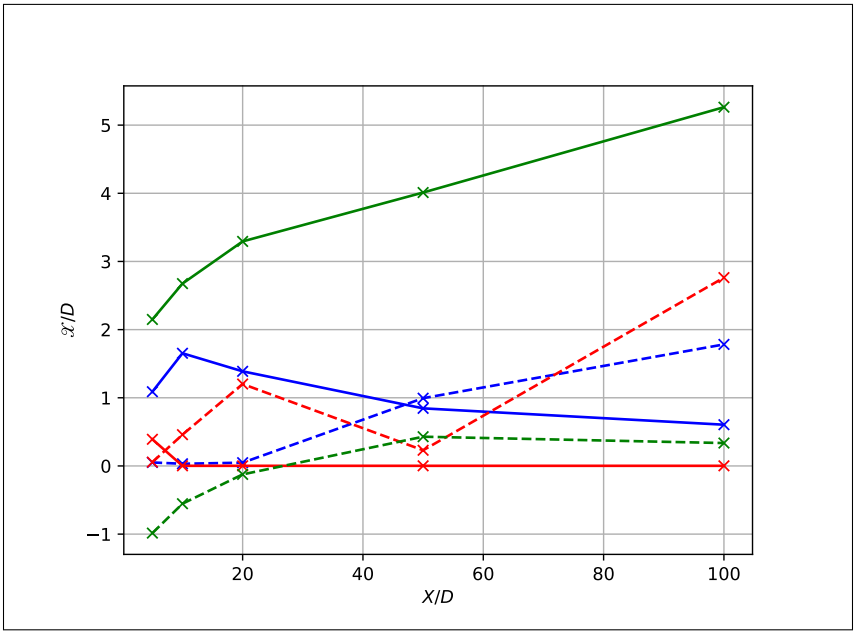

Figure G.8: Centerline Wake Vertical (Dashed) and Horizontal (Solid) position for the Velocity Ratio Study. : $r = 0.5$, : $r = 1.0$, : $r = 2.0$.

G.4 Cross Plane Contours

G.4.1 Axial Velocity

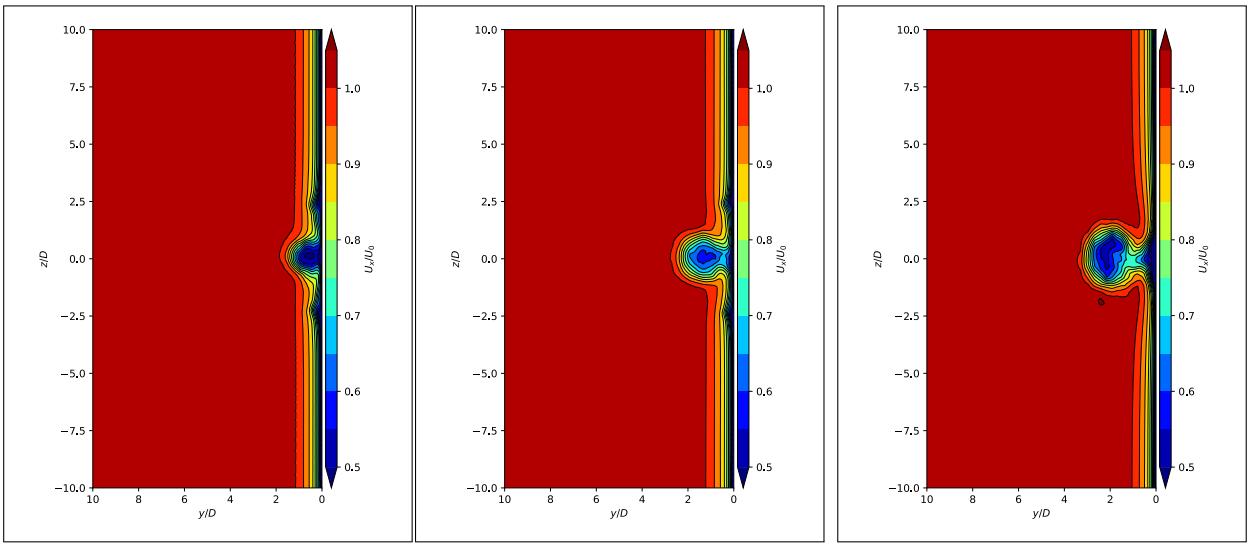

(a) $r = 0.5$ (b) $r = 1.0$ (c) $r = 2.0$

Figure G.9: Axial Velocity cross plane controus at $X/D = 5$.

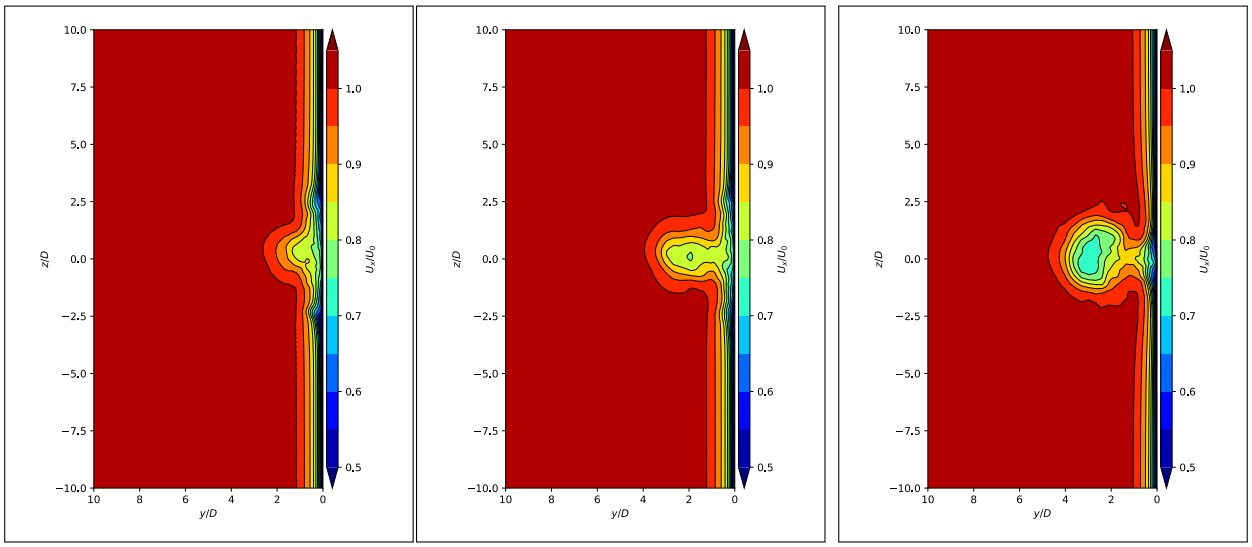

(a) $r = 0.5$ (b) $r = 1.0$ (c) $r = 2.0$

Figure G.10: Axial Velocity cross plane controus at $X/D = 10$.

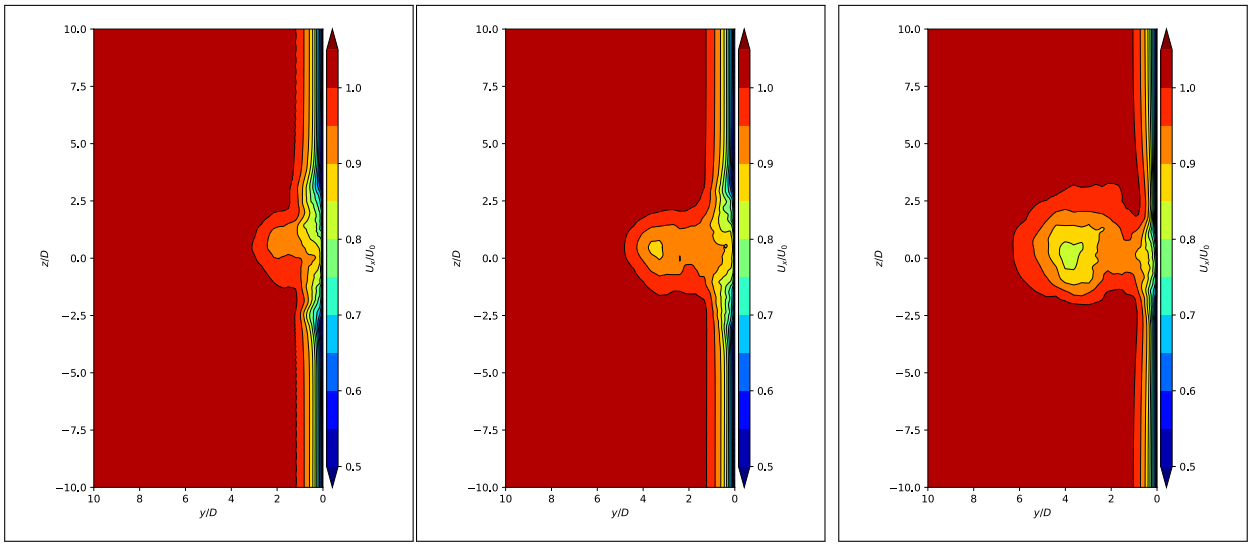

(a) $r = 0.5$ (b) $r = 1.0$ (c) $r = 2.0$

Figure G.11: Axial Velocity cross plane controus at $X/D = 20$.

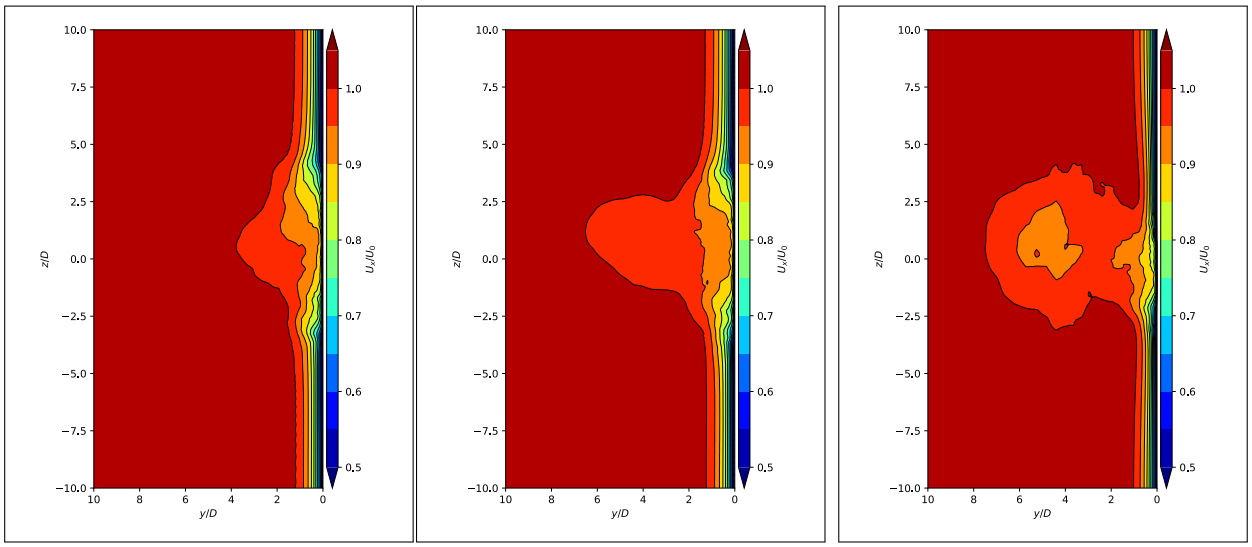

(a) $r = 0.5$ (b) $r = 1.0$ (c) $r = 2.0$

Figure G.12: Axial Velocity cross plane controus at $X/D = 50$.

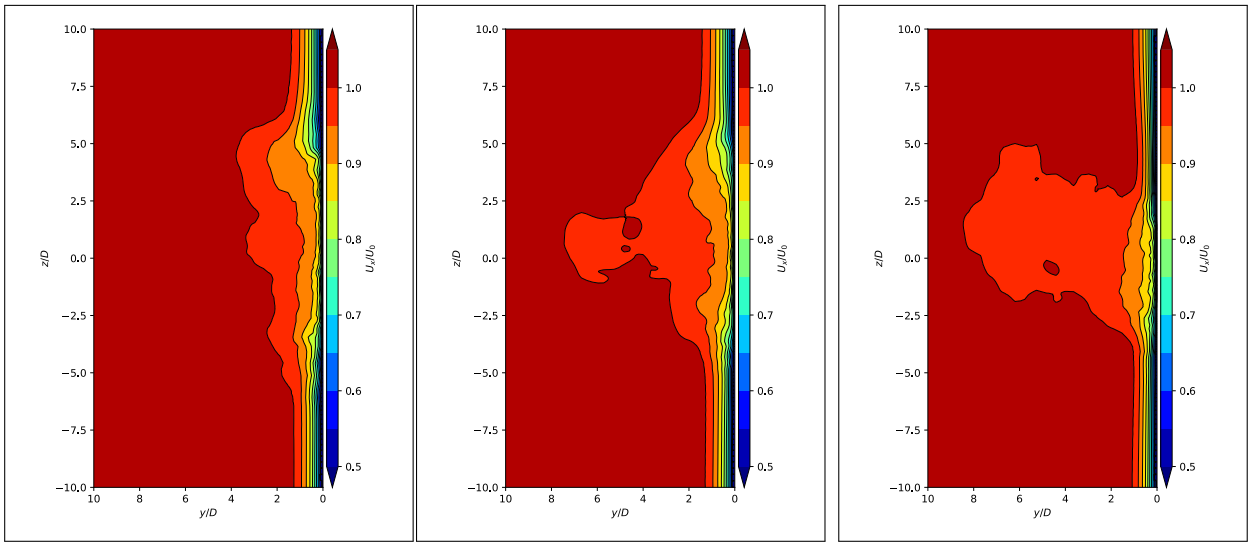

(a) $r = 0.5$ (b) $r = 1.0$ (c) $r = 2.0$

Figure G.13: Axial Velocity cross plane controus at $X/D = 100$.

G.4.2 Temperature Delta

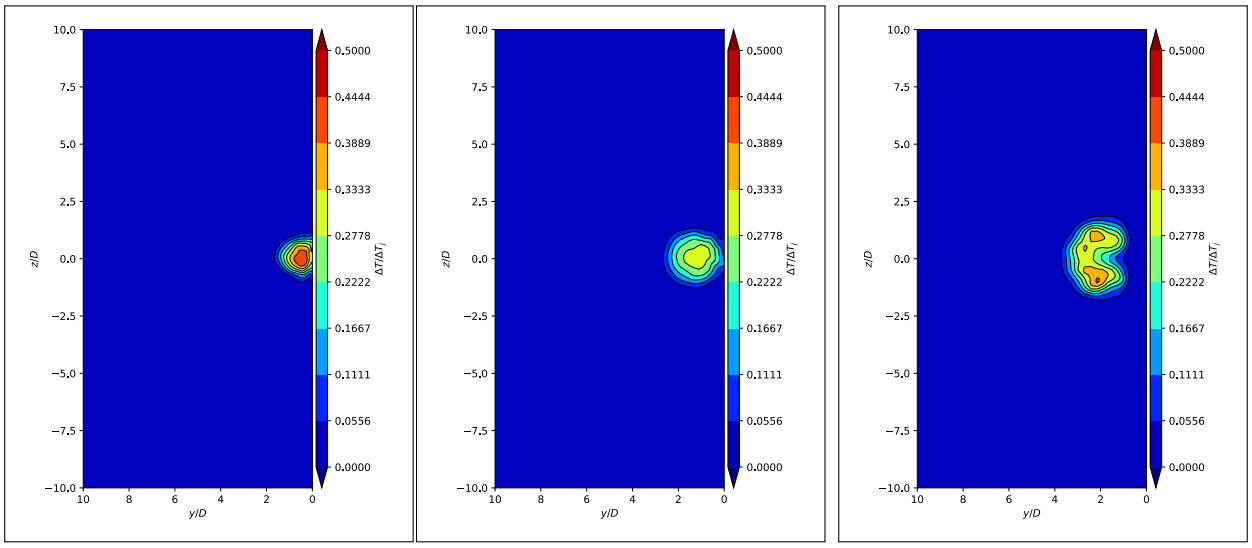

(a) $r = 0.5$ (b) $r = 1.0$ (c) $r = 2.0$

Figure G.14: Temperature Delta cross plane controus at $X/D = 5$.

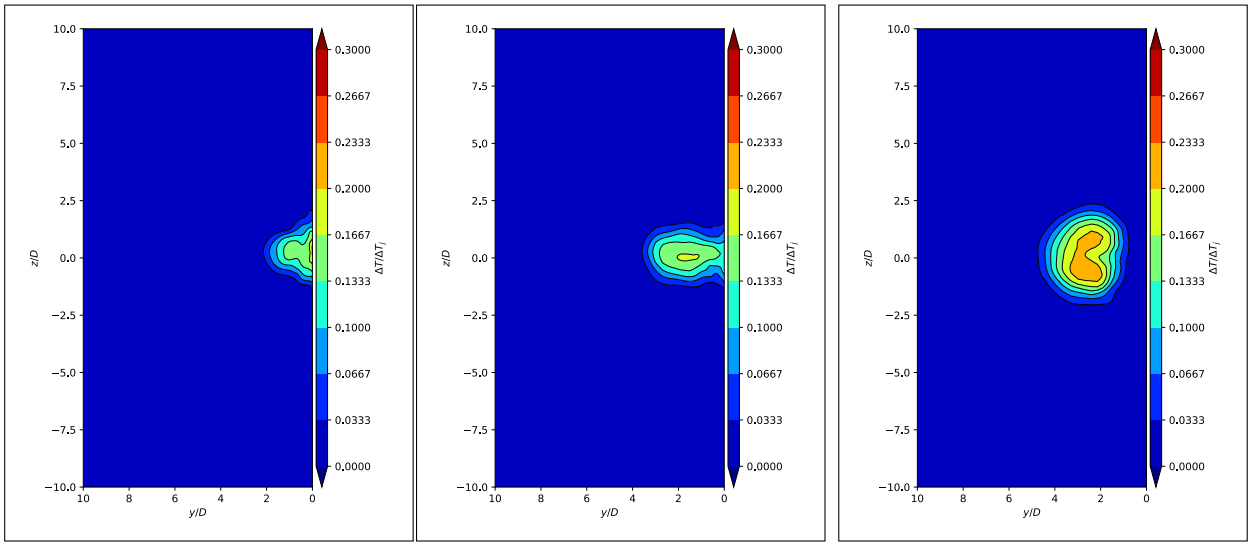

(a) $r = 0.5$ (b) $r = 1.0$ (c) $r = 2.0$

Figure G.15: Temperature Delta cross plane controus at $X/D = 10$.

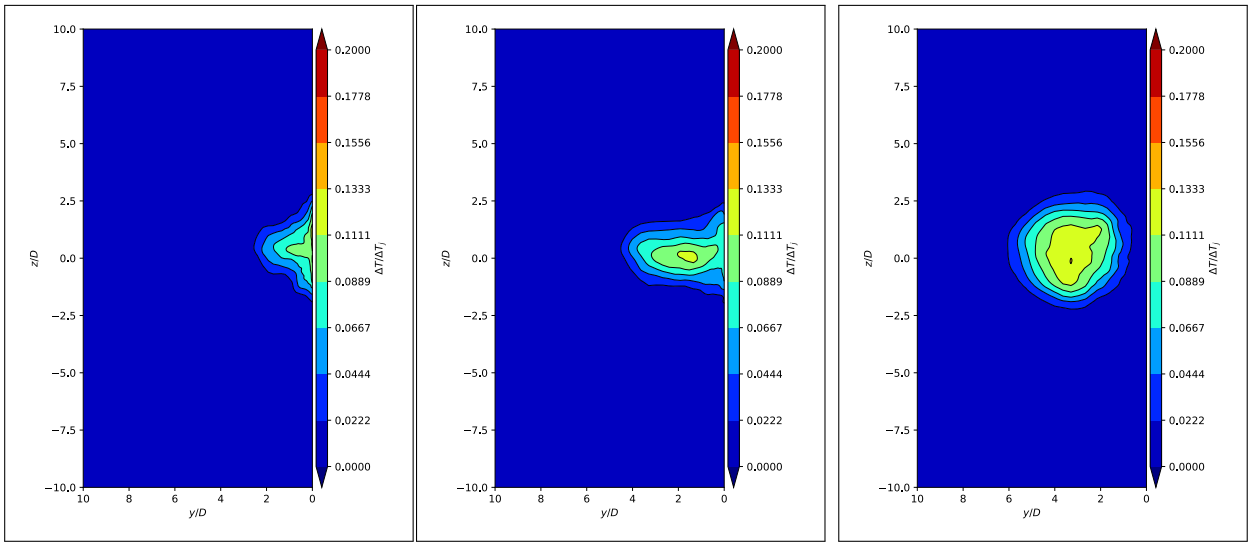

(a) $r = 0.5$ (b) $r = 1.0$ (c) $r = 2.0$

Figure G.16: Temperature Delta cross plane controus at $X/D = 20$.

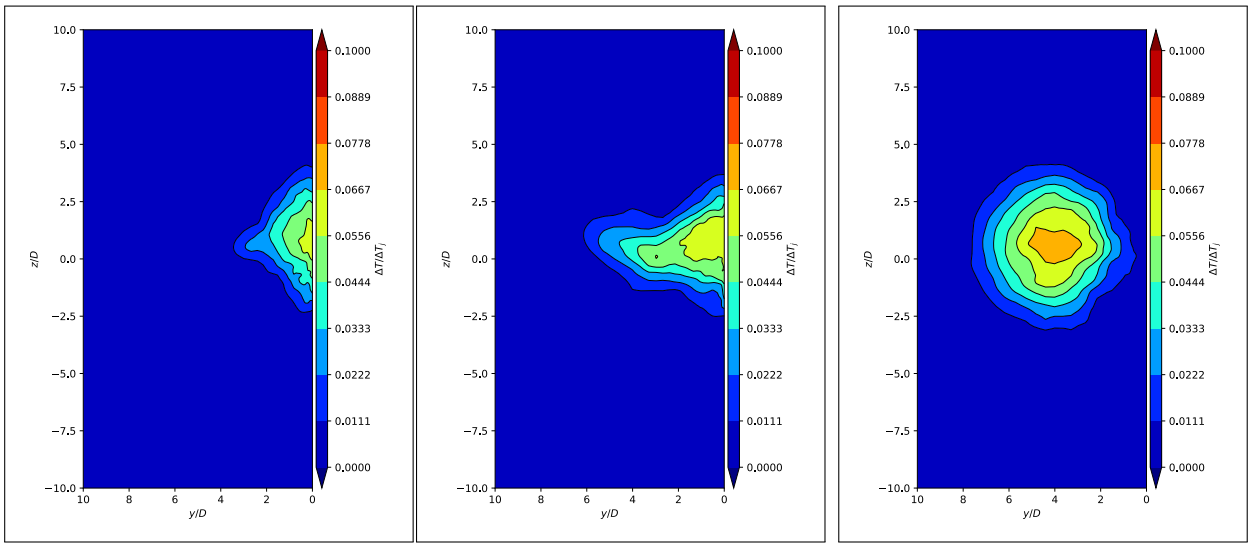

(a) $r = 0.5$ (b) $r = 1.0$ (c) $r = 2.0$

Figure G.17: Temperature Delta cross plane controus at $X/D = 50$.

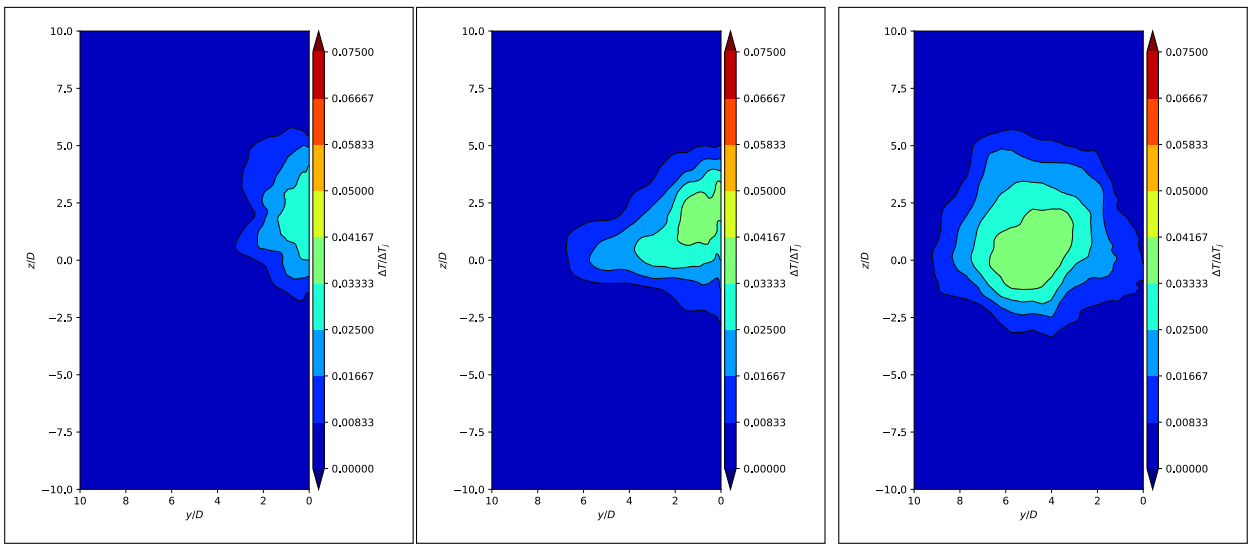

(a) $r = 0.5$ (b) $r = 1.0$ (c) $r = 2.0$

Figure G.18: Temperature Delta cross plane controus at $X/D = 100$.